

**DEVELOPMENT OF POROUS TITANOSILICATE-BASED  
HYBRID NANOCOMPOSITES FOR PHOTOCATALYTIC  
APPLICATIONS UNDER UV AND SOLAR LIGHT IRRADIATION**

**THESIS**

SUBMITTED IN PARTIAL FULFILMENT OF THE REQUIREMENTS  
FOR THE AWARD OF THE DEGREE OF

***Doctor of Philosophy***

IN  
**CHEMISTRY**

BY  
**A. AJAY KUMAR**  
**(Roll No. 701265)**

RESEARCH SUPERVISOR  
**Dr. N. VENKATATHRI**



**DEPARTMENT OF CHEMISTRY**  
**NATIONAL INSTITUTE OF TECHNOLOGY WARANGAL**  
**WARANGAL – 506 004, TELANGANA, INDIA**

**DECEMBER – 2017**

---

## DECLARATION

This is to declare that the work presented in the thesis entitled "***Development of Porous Titanosilicate-based Hybrid Nanocomposites for Photocatalytic Applications under UV and Solar Light Irradiation***" is a bonafide work done by me under the supervision of **Dr. N. Venkatathri**, Assistant Professor in the Department of Chemistry, and was not submitted elsewhere for the award of any degree.

I declare that this written submission represents my ideas in my own words and where others' ideas or words have been included, I have adequately cited and referenced the original sources. I also declare that I have adhered to all principles of academic honesty and integrity and have not misrepresented or fabricated or falsified any idea/data/fact/source in my submission. I understand that any violation of the above will be a cause for disciplinary action by the Institute and can also evoke penal action from the sources which have thus not been properly cited or from whom proper permission has not been taken when needed.

Date:

**(A. AJAY KUMAR)**

Place: **NIT Warangal**

Roll Number: **701265**

---

---

## **CERTIFICATE**

This is to certify that the work presented in the thesis entitled "***Development of Porous Titanosilicate-based Hybrid Nanocomposites for Photocatalytic Applications under UV and Solar Light Irradiation***" is a bonafide work carried out by **Mr. A. Ajay Kumar** under our supervision and was not submitted elsewhere for the award of any degree.

**Dr. N. Venkatathri**  
**(Research Supervisor)**  
Assistant Professor  
Department of Chemistry  
NIT Warangal



## ACKNOWLEDGEMENTS



---

---

## ACKNOWLEDGEMENTS

During the course of my Doctoral Research work, I have received the assistance and support from the following people:

First and foremost, I am truly indebted and I express my earnest gratitude for my Research Supervisor ***Dr. N. Venkatathri***, Assistant Professor, Department of Chemistry, National Institute of Technology Warangal for his inestimable expertise and astute guidance. His unabated enthusiasm, which stems from his absolute command over the subject, has been a constant source of inspiration for me to work hard and the outcome is expressed in the form of this thesis.

I am grateful to ***The Director***, National Institute of Technology Warangal for giving me the opportunity to carry out the work and allowing me to submit in the form of a thesis. I greatly acknowledge ***Ministry of Human Resource Development (MHRD)*** for the financial support in the form of fellowship.

I express my gratitude to the Doctoral Scrutiny Committee members: ***Dr. K. V. Gobi***, Chairman and Head, Department of Chemistry, ***Prof. I. Ajit Kumar Reddy***, Department of Chemistry and ***Prof. M. K. Mohan***, Department of Metallurgical and Materials Engineering, NIT Warangal for their detailed review, constructive suggestions and excellent advice during the progress of this research work.

My sincere thanks to the ***former Heads*** of the Department of Chemistry namely ***Prof. K. Laxma Reddy, Prof. B. Rajitha, and prof. V. Rajewara rao*** during the period of my research work.

I would like to thank all the faculty members from Chemistry Department namely ***Prof. B. V. Appa Rao, Prof. P. Nageswara Rao, Prof. A. Ramachandraiah, Prof. G.V.P. Chandramouli, Dr. P. V. Srilakshmi, Dr. Vishnu Shanker, Dr. D. Kashinath, Dr. B. Srinivas, Dr. K. Hari Prasad*** and the **other faculty members** for their valuable advice and encouragement throughout the research work.

I convey my special thanks from the bottom of my heart to my seniors, ***Dr. M. Nookaraju, Dr. A. Rajini, my juniors Mr. Ch. Suman, Mr. S. Suresh and Mr. G.***

---

  
*Srinath* for their continuous support and encouragement in each and every step of my research work.

I would like to convey my heartfelt thanks to *Dr. N. Siva Prasad*, Research Scholar, Department of ECE, *Dr. Santosh*, *Dr. T. Surender*, *Dr. K. Koteshwara Reddy*, *Dr. M. Satyanarayana* and *Mr. K. Vimal Kumar*, Research Scholars, Department of Chemistry for their fathomless support in technical discussions.

With all happiness, I acknowledge the cheerful assistance rendered by all my research colleagues, *Dr. K. Chaitanya Kumar*, *Dr. M. Narsimha Reddy*, *Dr. G. Srinivasa Rao*, *Dr. V. Krishnaiah*, *Dr. Srinivas Pavurala*, *Mr. Ashutosh Kumar Yadav*, *Mr. E. Hari Mohan*, *Mr. Phani Kumar*, *Mr. Vikram Sagar*, *Mr. M. Sai*, *Mr. G. Ambedkar*, *Mr. G. Ramesh*, *Mr. S. Nagaraju*, *Mr. Papalal*, *Mr. Ch. Raju*, *Dr. L. Suresh*, *Ms B. Mayuri*, *Ms R. Hithavani*, *Dr. O. Surender Reddy*, *Dr. Venkatrajam Marka*, *Dr. V. Jeevan* and my friends for their munificent support.

I am grateful to the lab assistants *Mr. Praveen*, *Mr. Srinivas* and **other supporting staff** of the Department of Chemistry, NIT Warangal for their cooperation.

I am thankful to my friends Mr. N. Narayana Reddy, Mr. S. Srinivas, Mr. S. Ravi Chandranath, Mr. T. Satish Rao, Mr. V. Sandeep, Dr. K. Yugender, Dr. M. Lasya, Mrs. P. Soumya, Mrs. P. Dhansita, Mr. K. Vamsi, Mr. V. Sunil kumar and Mr. K. Shekher for their help and encouragement.

My heart goes to my beloved **Parents, Wife, Brother, Children and Family Members** who with all their patience, prayers and faith in the Almighty, waited all these long years to see me reaching this stage. Their blessings and care always gave me new fervour and gusto to do something more with perfection.

Date:

**A. AJAY KUMAR**

---

# CONTENTS

---

## Table of Contents

### Contents

1. Introduction .....	1
1.1    Background .....	1
1.1    State of problem .....	1
1.2    Objectives of the present research work .....	2
1.3    Scope of the present research work.....	2
1.4    Semiconductor Photocatalysis .....	3
1.4.1    Photocatalysis .....	3
1.4.2    Mechanism of the photocatalysis.....	4
1.4.3    Photocatalysts and selection .....	7
1.4.4    Applications of photocatalysis.....	8
1.4.5    Why visible light active photocatalysis? .....	8
1.4.6    Development of efficient photocatalyst .....	9
1.4.6.1 Metal ion doping .....	9
1.4.6.2 Non–metal doping .....	9
1.4.6.3 Co-doping.....	9
1.4.6.4 Dye sensitization .....	11
1.4.6.5 Metal/semiconductor heterostructure .....	11
1.4.6.6 Semiconductor/semiconductor heterostructure .....	12
1.5    Nanotechnology and photocatalysis.....	13
1.6    Synthesis of nanomaterials.....	15
1.7    Characterization of materials .....	16
1.7.1    X-Ray diffraction (XRD).....	16
1.7.2    Thermogravimetric analysis (TGA) .....	17
1.7.3    Fourier transform infrared spectroscopy (FT-IR).....	18
1.7.4    UV–Visible diffuse reflectance spectroscopy (UV-Vis DRS) .....	19
1.7.5    Scanning electron microscopy (SEM) .....	20
1.7.5.1 Basic components of SEM .....	20
1.7.5.2 Basic operation principle of SEM .....	20
1.7.6    Transmission electron microscopy (TEM) .....	21
1.7.7    Energy dispersive X-ray spectroscopy (EDS) .....	21

---

---

1.7.8	Surface area analysis.....	22
1.7.9	Fluorescence spectroscopy .....	22
1.8	Photocatalytic properties (photodegradation of dye) .....	24
1.9	References .....	27
2	Development of novel porous Titanosilicate/g-C <sub>3</sub> N <sub>4</sub> nanocomposites for Photocatalytic degradation of Rhodamine-B under direct sunlight irradiation .....	32
2.1	Introduction .....	32
2.2	Experimental .....	33
2.2.1	Preparation of porous Titanosilicate .....	33
2.2.2	Preparation of g-C <sub>3</sub> N <sub>4</sub> .....	34
2.2.3	Preparation of mesoporous titanosilicate/g-C <sub>3</sub> N <sub>4</sub> hybrid nanocomposite ..	34
2.2.4	Photocatalytic activity .....	34
2.2.5	Scavenger Study .....	35
2.3	Results and Discussion.....	35
2.3.1	Photoluminescence analysis .....	42
2.3.2	photocatalytic activity.....	42
2.3.3	Reaction Mechanism .....	43
2.3.3.1	Reactive species .....	43
2.3.3.2	Hydroxyl radical generation.....	44
2.3.4	Proposed photocatalytic mechanism.....	44
2.3.5	Reusability .....	46
2.4	References .....	46
3	Development of magnetically separable and recyclable porous Titanosilicate/Fe <sub>3</sub> O <sub>4</sub> hybrid nanocomposites for photocatalytic degradation of methylene blue under UV light irradiation.....	49
3.1	Introduction .....	49
3.2	Experimental details.....	50
3.3	Results and Discussion.....	52
3.4	Photocatalytic Activity Test.....	58
3.5	References .....	63
4	Synthesis and Characterization of Fe <sub>3</sub> O <sub>4</sub> @Titanosilicate/g-C <sub>3</sub> N <sub>4</sub> nanocomposites and their photocatalytic effect on the degradation of Rhodamine B under Sunlight irradiation.....	66
4.1	Introduction .....	66

---

---

4.2	Experimental details.....	67
4.2.1	Materials .....	67
4.2.2	Method.....	68
4.2.2.1	Preparation of Fe <sub>3</sub> O <sub>4</sub> Magnetic nanoparticles (FO).....	68
4.2.2.2	Preparation of Fe <sub>3</sub> O <sub>4</sub> @Titanosilicate (FTS).....	68
4.2.2.3	Preparation of Fe <sub>3</sub> O <sub>4</sub> @Titanosilicate/g-C <sub>3</sub> N <sub>4</sub> (FTSCN) hybrid nanocomposite .....	68
4.2.3	Photocatalytic activity of FTSCN nanocomposites .....	69
4.3	Results and Discussion.....	69
4.3.1	Powder-XRD Analysis .....	69
4.3.2	Morphology characterization and EDX Analysis .....	70
4.3.3	FTIR Analysis.....	72
4.3.4	UV-Visible DRS Spectra.....	73
4.3.5	Photoluminescence analysis .....	74
4.4	Photocatalytic degradation .....	75
4.4.1	Reactive species.....	76
4.5	References .....	78
5	Synthesis and Characterization of porous Titanosilicate/Vanadium pentoxide nanocomposites and their applications for the degradation of methylene blue under sunlight irradiation.....	81
5.1	Introduction.....	81
5.2	Experimental details.....	82
5.2.1	Materials .....	82
5.2.2	Method.....	82
5.2.2.1	Preparation of highly porous Titanosilicate (TS) .....	82
5.2.2.2	Preparation of pure V <sub>2</sub> O <sub>5</sub> nanoparticles .....	83
5.2.2.3	Preparation of VTS inorganic hybrid nanocomposite .....	83
5.2.3	Photocatalytic activity .....	83
5.3	Results and discussion .....	84
5.3.1	Powder X-ray Diffraction Analysis .....	84
5.3.2	Morphology Characterization.....	85
5.3.3	FTIR Analysis.....	87
5.3.4	UV-Visible DRS Spectra .....	88
5.3.5	Photoluminescence .....	89

---

---

5.4	Photocatalytic activity.....	90
5.5	Photocatalytic mechanism.....	93
5.6	References .....	94
6	Photocatalytic degradation of Rhodamine B under direct sunlight irradiation using porous Titanosilicate/Bismuth Vanadate hybrid nanocomposites.....	96
6.1	Introduction .....	96
6.2	Experimental Section.....	97
6.2.1	Synthesis of photocatalysts.....	97
6.2.2	Dye photodegradation experiment.....	98
6.3	Results and Discussion.....	99
6.3.1	Morphology and composition characterization .....	99
6.3.2	Photoluminescence .....	103
6.3.3	Photocatalytic activity and the mechanism: .....	104
6.4	References:.....	108
7	Summary and Conclusions.....	111
7.1	Present thesis.....	111
7.2	Conclusions.....	111
7.3	Summary .....	113
7.4	Outlook for future work .....	113
8	LIST OF PUBLICATIONS, CONFERENCES .....	115
9	BIO-DATA.....	119

---

---

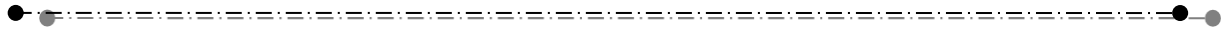
## SYMBOLS AND ABBREVIATIONS

IUPAC	:	International Union for Pure and Applied Chemistry
cm	:	Centimetre
nm	:	Nanometre
Å	:	Angstrom
$\theta$	:	Theta
$\lambda$	:	Lambda
$\beta$	:	Beta
eV	:	Electron volt
$\epsilon$	:	Epsilon
$\nu$	:	Neu
mL	:	milli Litre
$\mu$ L	:	micro Litre
M	:	Molarity
mM	:	milli Molar
h	:	Hour
mins	:	minutes
°C	:	Degree centigrade
K	:	Kelvin
$\mu$ m	:	Micro metre
g	:	Grams
mg	:	milli Grams
mmol	:	milli Mole
RT	:	Room Temperature
SEM	:	Scanning Electron Microscopy
TEM	:	Transmission Electron Microscopy
XRD	:	X-ray Diffraction
FTIR	:	Fourier Transform Infra Red
UV	:	Ultra-violet
PL	:	Photoluminescence



# CHAPTER I

## Introduction



## 1. Introduction

### 1.1 Background

Development of alternative clean energy supplies and pollution-free technologies for green remediation in the sustainable growth of human society is an urgent need. Therefore, search for renewable energy sources and sustainable environmental technologies are primary challenges for enhancing the quality of human life.<sup>[1-4]</sup> Since the first discovery of water splitting for hydrogen production by Fujishima and Honda, the semiconductor-mediated photocatalysis has very much attracted great attention since its potential applications in photocatalytic degradation of pollutants, self-cleaning, and bacterial elimination using non-toxic, low-cost methods.<sup>[5-8]</sup> Photocatalysis, in which sunlight is used as an energy source is one of the most promising technologies to overcome the current day energy and water pollution problems. The advantage of solar energy lies in its ecological purity. It offers the possibility of accomplishing energy cycles without environmental pollution and additional heating of the Earth.<sup>[9,10]</sup> In the previous years, remarkable efforts have been made for improving photocatalysis under visible light irradiation. However, photocatalytic applications under the visible light are still limited due to the low efficiency caused by some exciting issues like slight light-response range, surface structure, high recombination rate, low stability of the material.<sup>[11,12]</sup> Therefore, development of highly efficient visible light active photocatalysts is the current need.

#### 1.1 State of problem

With rapid developments in science and technology, several productions such as textile, petrochemical, food, chemical are being set up universal. These industries release contaminated water leading to pollution of natural water resources. Pollution of consumption water sources with dangerous organic matters has been known as the main problem worldwide. In fact, earth's environment is getting deteriorated due to acid rain, CFC's, global warming, polluted water etc. Nobel prize was awarded to the discoverer of DDT which is an insecticide but it is now banned due to its negative impact on the environment.<sup>[13a]</sup>

Photocatalysis can mimic normal photosynthesis to directly transform solar energy into chemical energy. It is an effective strategy for renewable energy generation and environmental remediation. But, the performance of currently available photocatalysts

doesn't meet the requirements necessary for useful applications. Therefore, studies on the development of highly effective visible light active photocatalysts for environmental remediation is undertaken in this work.

**Nanocomposites:** Nanocomposites are composites in which at least one of the phases shows dimensions in the nanometre range.<sup>[13b]</sup> Nanocomposite materials have emerged as suitable alternatives to overcome limitations of microcomposites and monolithics, while posing preparation challenges related to the control of elemental composition and stoichiometry in the nanocluster phase. They are reported to be the materials of 21<sup>st</sup> century in the view of possessing design uniqueness and property combinations that are not found in conventional composites. The general understanding of these properties is yet to be reached,<sup>[13c]</sup> even though the first inference on them was reported as early as 1992.<sup>[13d]</sup>

## 1.2 Objectives of the present research work

Objectives of the present research work are:

- i. To develop porous titanosilicate-based hybrid nanocomposites
- ii. To characterize the synthesized hybrid nanocomposites and determine their structural, chemical and photophysical properties.
- iii. To Study the photocatalytic activity of the synthesized hybrid nanocomposites for degradation of dyes under UV and direct sunlight irradiation.

## 1.3 Scope of the present research work

The successfully developed novel porous Titanosilicate-based photocatalysts can be potentially applied for the further research and development in clean renewable energy production and also used to treat the contaminants and pollutants in water/air body which are more hazardous to the human life. Furthermore, it would be interesting to work on the formation of porous Titanosilicate-based photocatalysts with unique nanoarchitecture in order to fulfill the needs of practical applications. Cost-effective and magnetically separable  $\text{Fe}_3\text{O}_4$  @ Titanosilicate/g-C<sub>3</sub>N<sub>4</sub> photocatalyst facilitates its reutilization and also opens the possibility of working in a continuous regime.

## 1.4 Semiconductor Photocatalysis

### 1.4.1 Photocatalysis

Photocatalytic technology refers to the rate of chemical reactions (oxidation or reduction) by the initiation of a catalyst, generally a semiconductor material by visible or UV light. Photocatalytic degradation of organic pollutants and photocatalytic water splitting can be simply defined as an artificial photosynthesis. In photosynthesis, (figure 1.1a) plants use chlorophyll and light to generate starch (organic matter) and oxygen from carbon dioxide and water, whereas a photocatalyst can decompose organic matter into carbon dioxide and water using oxygen and water by light irradiation. It can also decompose the water into oxygen and hydrogen gases.<sup>[14–16]</sup> Therefore, photocatalysis is a promising alternative technology for photodegradation of pollutants in water or air and for production of clean renewable energy through the photoinduced electrons and holes in semiconductor particles (figure 1.1b).

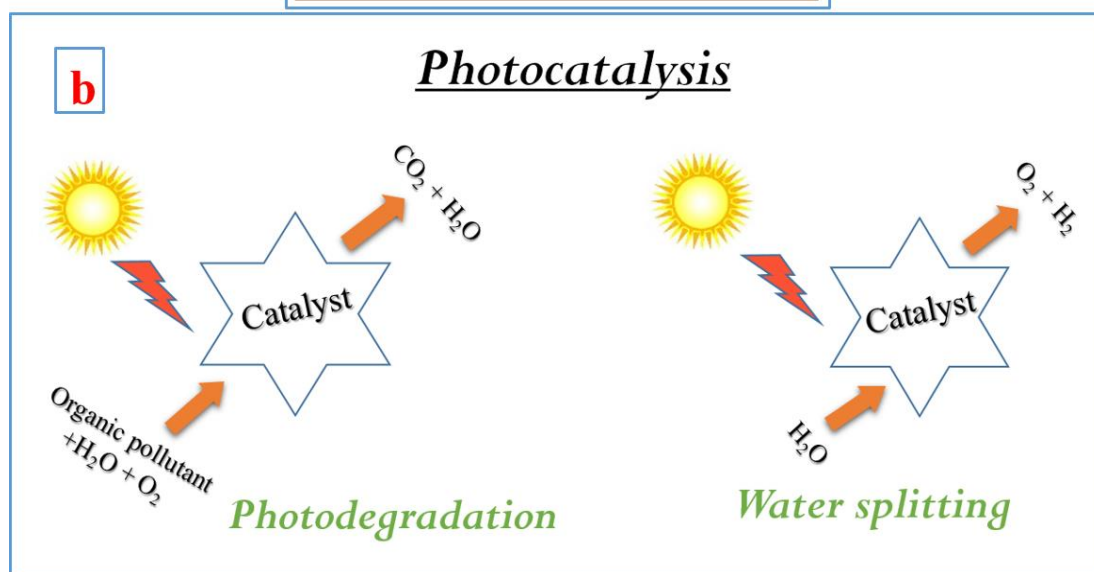
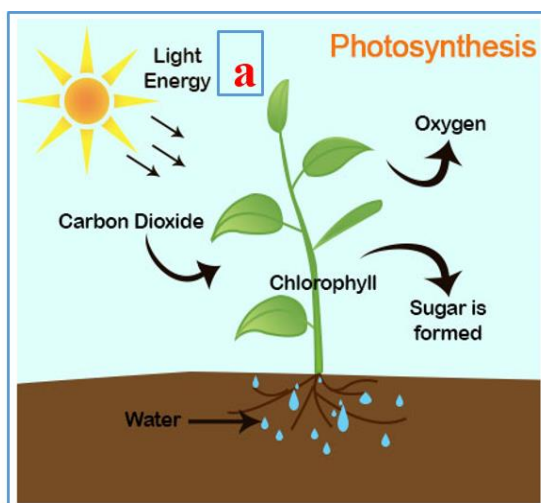


**Figure 1.1:** Schematic illustration of the process of (a) photosynthesis and (b) photocatalysis: photodegradation of organic pollutants and photocatalytic water splitting

#### 1.4.2 Mechanism of the photocatalysis

Photocatalysis is started by charge transfer of electron-hole pairs afterwards band gap excitation (figure 1.2). While a photocatalyst is irradiated by light with energy equal to (or higher than) band gap energy, the valence band electrons ( $e^-$ ) transfer to the conduction band, leaving a hole ( $h^+$ ) in the valence band (step I). The electron-hole pairs can recombine, releasing the input energy as heat, with no chemical effect (step II). However, if the electrons and holes travel to the superficial of the photocatalyst, they can play a part in redox reactions with adsorbed species such as organic or inorganic species, oxygen and water (step III and IV).<sup>[17-24]</sup>

Even though the physics behind the parting of charge carriers varies with various applications and also the surface-electronic structure of photocatalyst, it is definitely known that the major reactions liable for positive photocatalytic effect are interfacial redox reactions of electrons and holes that are produced upon bandgap excitation.<sup>[25,26]</sup>

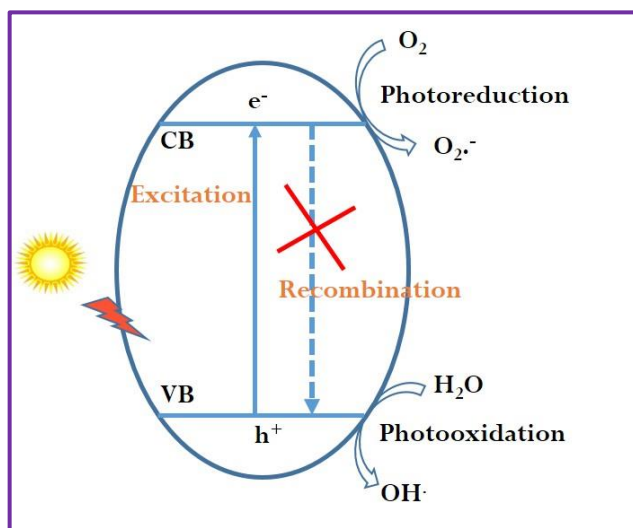


**Figure 1.2:** Schematic illustration of the major processes occurring on a semiconductor photocatalyst under light irradiation

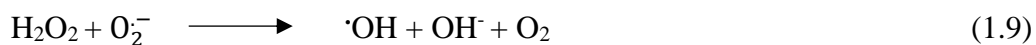
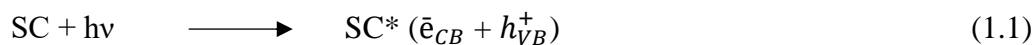
The process described above could be briefly expressed by the steps as follows



Recombination	$e_{CB}^- + h_{VB}^+ \rightarrow \text{heat}$	Step II
Reduction reaction	$A + e_{CB}^- \rightarrow A^-$	Step III
Oxidation reaction	$B + h_{VB}^+ \rightarrow B^+$	Step IV

However, these redox reactions are the basic mechanism of photocatalytic degradation and photocatalytic hydrogen production. For photocatalytic degradation, valence band (VB) holes are the important elements that induce the oxidative decomposition of environmental pollutants. The holes react with water to generates the hydroxyl radical ( $\cdot\text{OH}$ ), this is oxidation reaction occurs at valence band. Which is very powerful oxidant with the oxidation potential of 2.8 eV (NHE).  $\cdot\text{OH}$  quickly attacks pollutants at the surface and can transform them into  $\text{H}_2\text{O}$  and  $\text{CO}_2$ . The photocatalytic mechanism of the organic pollutants degradation in water has been reported broadly in the literature.<sup>[27-34]</sup>

The photocatalytic mechanism of the organic pollutants oxidation under light can be obtained as follows.





From the above reactions, it can be found that various active radicals including  $\text{O}_2^{\cdot-}$ ,  $\cdot\text{OH}$ ,  $\text{HO}_2^{\cdot}$ , and  $\text{H}_2\text{O}_2$  are formed in this process, and among which the  $\cdot\text{OH}$  are theoretical to be the primary oxidizing agent in the photocatalytic oxidation (*eq.* (1.11)). A direct oxidation of carboxylic acids to generate  $\text{CO}_2$  involving the holes (*eq.* (1.12)) was also confirmed, and called as “photo-Kolbe reaction”. The role of the reductive pathways (*eq.* (1.13)) is of a minor significance than oxidation. However, according to thermodynamic requirement, the VB and CB of a semiconductor should be positioned in such way that, the reduction potential of superoxide radicals ( $E_{(\text{H}_2\text{O}_2/\cdot\text{OH})}^0 = -0.3 \text{ eV}$  vs. NHE) and the oxidation potential of the hydroxyl radicals ( $E_{(\text{O}_2/\cdot\text{O}^-)}^0 = +2.8 \text{ eV}$  vs. NHE) within the band gap for actual photodegradation. In other words the redox potential of the hole need to be suitably positive to produce  $\cdot\text{OH}$  and that of the electron need to be suitably negative to produce  $\text{O}_2^{\cdot-}$ .

In the photocatalysis, reducing conduction band (CB) electrons are more significant for generation of hydrogen from water splitting. In order to initiate hydrogen generation, the conduction band level needs to be more negative than the water splitting level:



The total reaction redox potential is  $E_{\text{H}} = -1.23 \text{ V}$  (NHE) at  $\text{pH}=7$ , with the conforming half-reactions of  $-0.41 \text{ V}$  (*eq.* 1.17) and  $0.82 \text{ V}$ , which gives a  $\Delta G^\circ = +237 \text{ kJ/mole}$ .

In this phenomenon, the separation of space charge carriers varies with different applications and also the surface-electric structure of photocatalyst. It is clearly accepted

that the main reactions accountable for positive photocatalytic effect are interfacial redox reactions of electrons and holes that are generated upon bandgap excitation (figure 1.3). Until now, many review articles have published the modern developments reached in the area of  $\text{TiO}_2$ -based photocatalysis.<sup>[35–40]</sup>

#### 1.4.3 Photocatalysts and selection

Since the discovery of photocatalytic water splitting phenomenon on  $\text{TiO}_2$  electrodes by UV light irradiation,<sup>[2]</sup> numerous researchers have been devoted to  $\text{H}_2$  production via this novel and smart process aiming to find an alternative fuel source to solve the energy problem. On the other hand, since the first report of employing photocatalyst for decomposing cyanide,<sup>[41]</sup> the applications in environmental purification have been rapidly developed, and we may find various products and technologies around us to purify the environment by using photocatalysts. A large number of semiconductors, such as  $\text{TiO}_2$ ,  $\text{ZnO}$ ,  $\text{Fe}_2\text{O}_3$ ,  $\text{WO}_3$ ,  $\text{SrTiO}_3$ ,  $\text{NaTaO}_3$ ,  $\text{CdS}$ ,  $\text{Ag}_3\text{PO}_4$ ,  $\text{BiPO}_4$ ,  $\text{MoS}_2$  etc., are known to catalyze the photochemical reaction (figure 1.3). However, the practical utilization of a photocatalyst for water splitting to produce  $\text{H}_2$  fuel and degradation of organic pollutants to protect the environment is still a huge challenge, due to its low efficiency.<sup>[36,38–45]</sup>

The photocatalytic material selection should also be based on the characteristics were shown in figure 1.4.

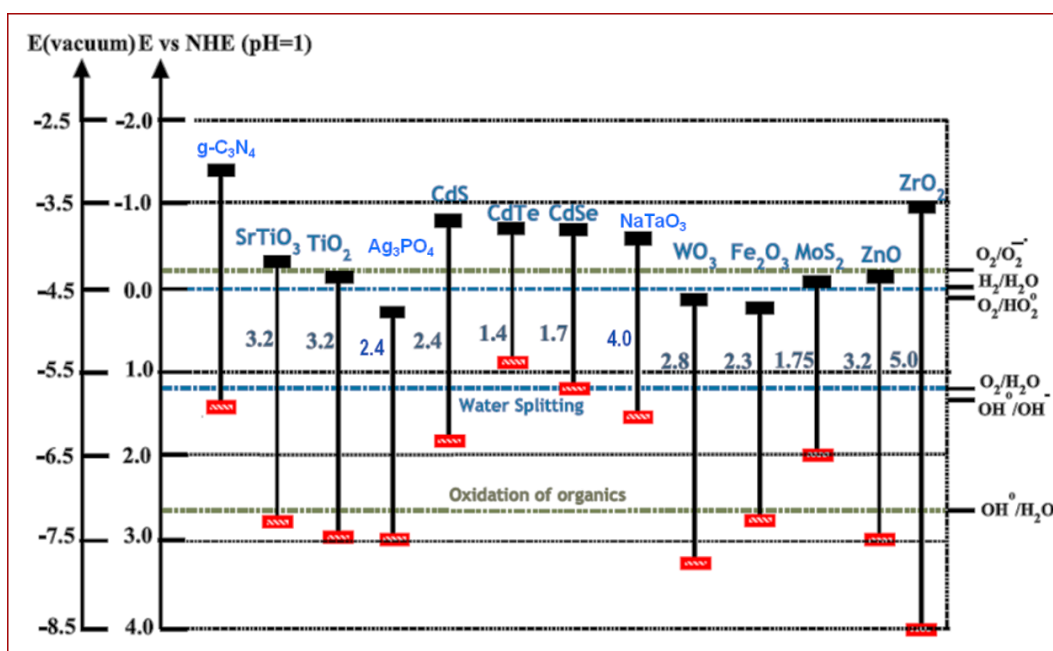


**Figure 1.3:** Band gap energy and band edge positions of different semiconductor materials

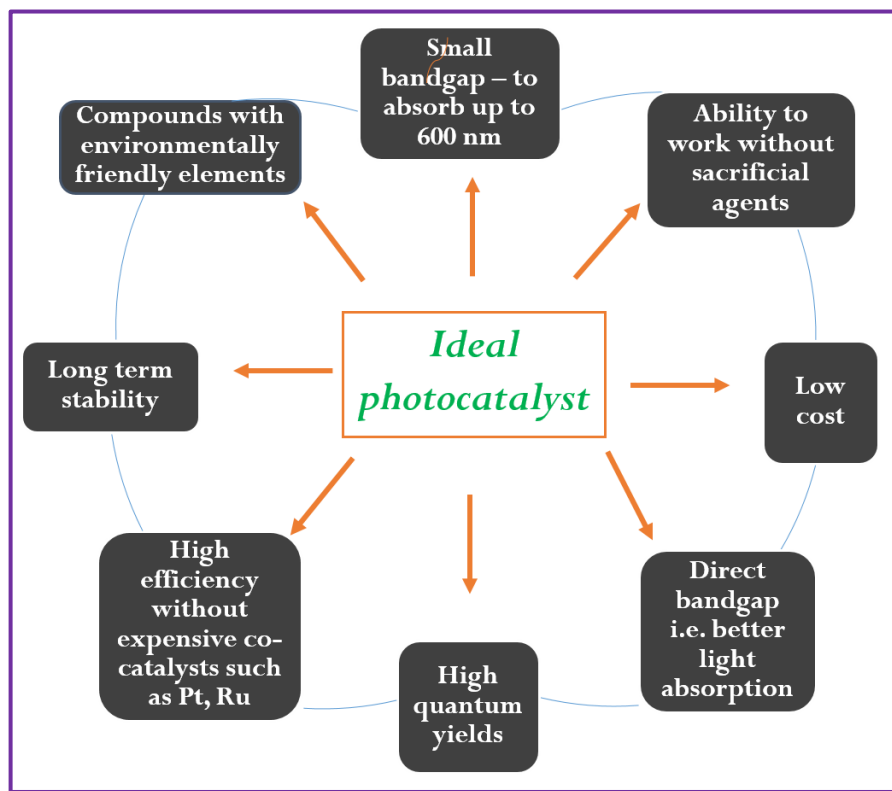


**Figure 1.4:** Characteristics of an ideal photocatalyst

#### 1.4.4 Applications of photocatalysis

The application of photocatalysis has been remarkably developed for a decade. However, there is a great challenge to use sunlight energy as a source of energy in photoreaction to solve the environmental problem and energy crisis in the future. In the recent investigation, photocatalytic processes have been widely used in various applications such as disinfection of drinking water, antibacterial for textile industries, anti-microbe for plastic container, persistent toxic compounds treatment, organic degradation, self-cleaning technology, soil purifications, deodorization, sterilization, air purification, high efficiency/low cost solar cells, and even clean renewable hydrogen energy production from water splitting (figure 1.5).<sup>[46-56]</sup>

#### 1.4.5 Why visible light active photocatalysis?

As shown in figure 1.6, the total solar energy consists of three parts, UV light (~ 5%), visible light (~ 45%), and IR light (~ 50%).<sup>[57]</sup> It means that the visible light active

photocatalysis is great opportunity to utilize maximum compartment in the solar energy spectrum.

To utilize solar energy efficiently, research for developing the high performance visible light photocatalysts have never stopped, which can be clearly reflected from the increasing number of research papers and patents relating to photocatalysis.

#### 1.4.6 Development of efficient photocatalyst

##### 1.4.6.1 Metal ion doping

Metal ion doping has been mainly studied to improve the photocatalytic performance under irradiation of UV light. Nowadays, visible light active photocatalysis using metal ion doped semiconductor has been a topic of prime concern for many researchers. Subsequently, these have revealed the extended absorption spectra into the visible light area. This property has been described by the electrons transfer from dopant ion to the semiconductor conduction band is called as a metal to conduction band charge-migration. Various metal ions, including rare earth metal ions (such as ytterbium, lanthanum and cerium) and transition metal ions (such as V, Cr, Fe, Ni, Co, Pt, Ru) have been explored as possible dopants for visible light photocatalysis.<sup>[9,58,59]</sup>

##### 1.4.6.2 Non-metal doping

The studies of visible light semiconductors, non-metal doping such as C, N and S have been carried out, meanwhile the synthesis of N-TiO<sub>2</sub> in 2001.<sup>[9,60]</sup> It was initially proposed that nitrogen doped titania be able to change its light response into the visible area by collaborating 2p orbitals of lattice O with 2p orbitals of N and growth the photocatalytic performance by reduction band gap of the TiO<sub>2</sub>. Still, current revisions have revealed both practically and theoretically, the localized nitrogen 2p orbitals above the VB and the excitations from N 2p orbital to the CB are made in TiO<sub>2</sub> under visible light irradiation.<sup>[61,62]</sup> Unlike metal and non-metal ion dopants, exchange lattice oxygen and are less likely form recombination centers.

##### 1.4.6.3 Co-doping

In recent times, the result of co-doping has also been widely reported. Few reports have revealed that N and F co-doping is beneficial for low energy cost and a decrease of defect formation for the incorporation of N due to the donor (F) and acceptor (N) charge

compensation effect.<sup>[9,63]</sup> When La-doped TiO<sub>2</sub> co-doped with nitrogen effectively changes the photoabsorption edge.<sup>[64]</sup>

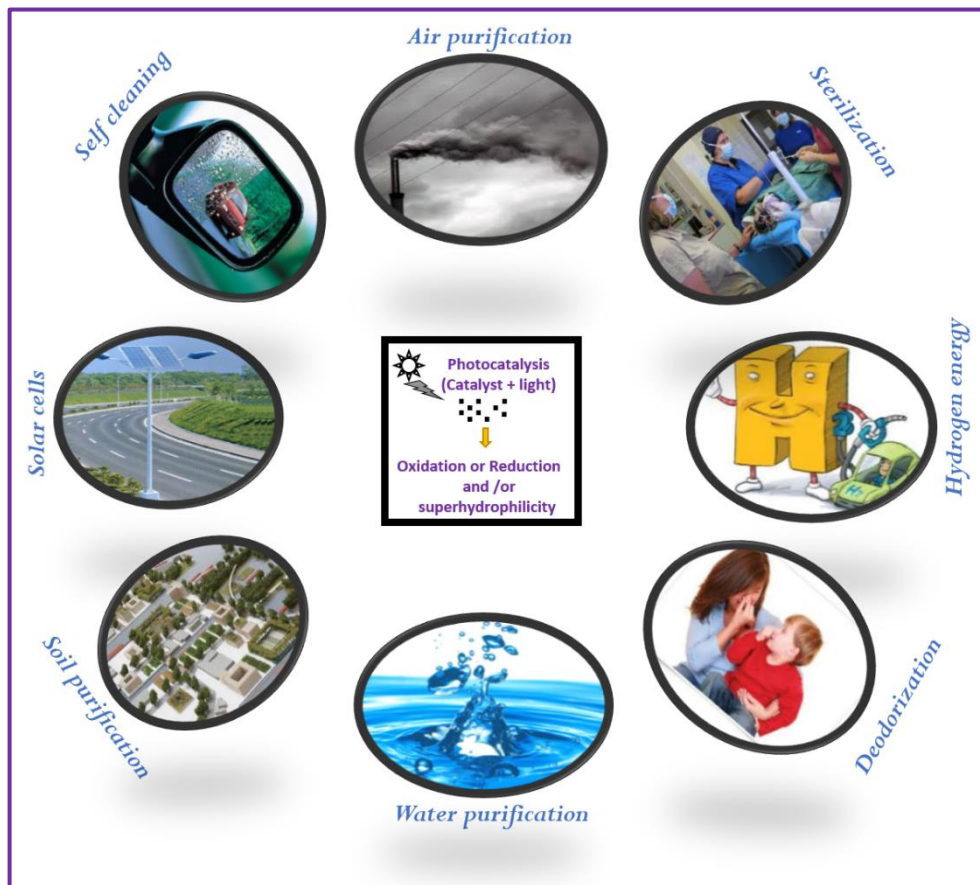


**Figure 1.5:** Potential applications of photocatalysis

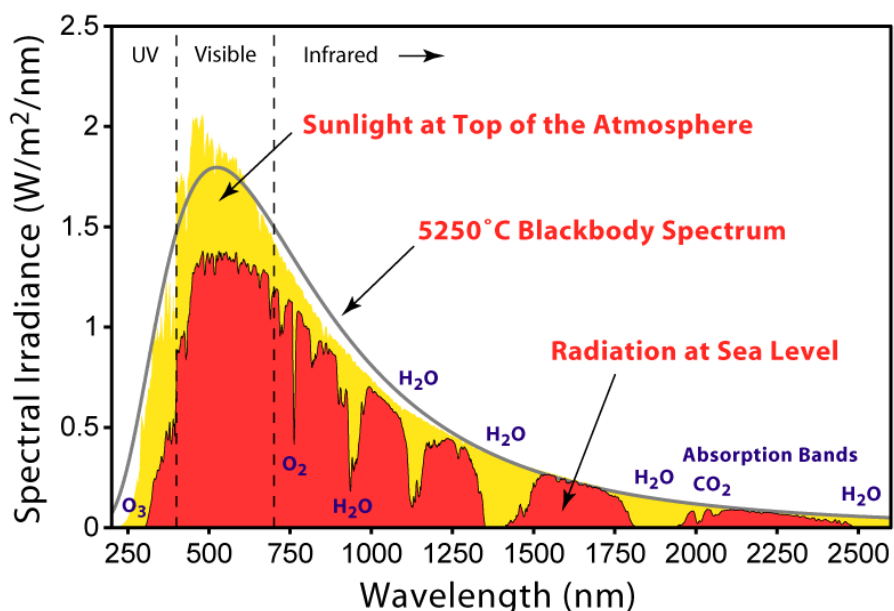


**Figure 1.6:** The wavelength distribution of solar light

#### 1.4.6.4 Dye sensitization

Dye sensitization has been studied by several groups and selected one of the best methods to extend the wide bandgap semiconductors photoresponse into the visible region.<sup>[65][66]</sup> However, these kinds of studies are exploited in the well identified dye sensitized solar cells.<sup>[65]</sup> The dye sensitized photodegradation mechanism is based on the absorption of visible light for moving an electron from the HOMO (Highest Occupied Molecular Orbital) to the LUMO (Lowest Unoccupied Molecular Orbital) of a dye.<sup>[67]</sup> The excited dye molecule then electrons migrate into the CB of semiconductor and these inserted electrons reach to the surface where  $O_2$  to form  $O_2^-$  and  $\cdot OOH$ . These reactive species can also disproportionate to give  $\cdot OH$ . The subsequent radicals chain reactions can lead to the dye degradation.

#### 1.4.6.5 Metal/semiconductor heterostructure

Noble metals (silver, gold, platinum) deposition on the superficial of semiconductor photocatalysts improves the photocatalytic performance under visible light irradiation (figure 1.7). The advantages of metal in metal/semiconductor, promote the charge migration, act as an electron trapping agent and then reducing electron–hole pair recombination effect.<sup>[68–70]</sup> The metallic elements in the metal/semiconductor photocatalyst could also improve the light absorption capacity of semiconductors through a plasmonic enhancement effect.

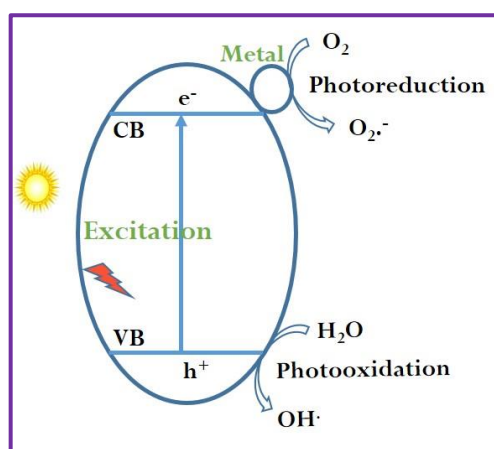


**Figure 1.7:** Schematic illustration for charge separation in metal/semiconductor heterostructure

#### 1.4.6.6 Semiconductor/semiconductor heterostructure

In related to single-segment photocatalysts, which generally have less flexibility in altering their electronic property by doping and low parting efficiency of photoinduced charge transporters. In heterostructure photocatalysts have major benefits in promoting the parting of electron-hole pairs and possession reduction and oxidation reactions at two different reaction sites.<sup>[71–74]</sup> The objective of making heterostructured photocatalysts is to help the parting of photoinduced electron–hole pairs over many carrier transfer paths, and to extend the light-response range by coupling proper electronic properties in materials (figure 1.8). The best characteristic heterostructured photocatalyst constructed on the traditional transfer method is the  $\text{TiO}_2/\text{CdS}$  structure.<sup>[73]</sup> In  $\text{TiO}_2/\text{CdS}$  heterostructure, the highly capable charge migration process is reported by Spanhel *et al.* The CdS electrons are shifted into the titania while the holes generates in the cadmium sulphide. This also aids for isolation of electrons and holes in semiconductors but at the same period, permits the extension of the photoresponse of the photocatalyst in the visible region. Recently, the first novel metal-free polymeric graphitic carbon nitride ( $\text{g-C}_3\text{N}_4$ ), as well as non-oxide  $\text{Ag}_3\text{PO}_4$ , emerged as visible light active photocatalysts which exhibit good photocatalytic activity for water splitting and environmental remediation.<sup>[75,76]</sup> However, the photocatalytic efficiency of this pure  $\text{g-C}_3\text{N}_4$  and  $\text{Ag}_3\text{PO}_4$  is still limited due to the high recombination rate of photoinduced electron-hole pairs and low surface area.  $\text{Ag}_3\text{PO}_4$  is also suffering from serious photocorrosion. The development of photocatalysts by direct combination of two semiconductors is a good method to help the isolation of charge carriers for enhanced photocatalytic performance.<sup>[72]</sup> The heterostructure has excellence of developing a positive interface combination, offers a highly capable charge separation, the charge carriers lifetime also increases and an improved charge migration. In particular, the type-II (staggered band gap) heterostructure (figure 1.9) has excellence of developing a constructive interface combination and the spatially isolated charge carrier on other sides of the hetero/nanojunction in which holes can be regulated to one side and electrons to other side.<sup>[77]</sup> The electrons and holes in the type-II hetero/nanostructures could make them a proper candidate for enhanced photocatalysis. In this search, the present thesis has been focused on improving the photocatalytic performance of porous titanosilicate,  $\text{g-C}_3\text{N}_4$ ,  $\text{V}_2\text{O}_5$ , and  $\text{BiVO}_4$ , under visible light by forming the two phase nano/heterojunction of these semiconductor materials for photocatalytic applications.

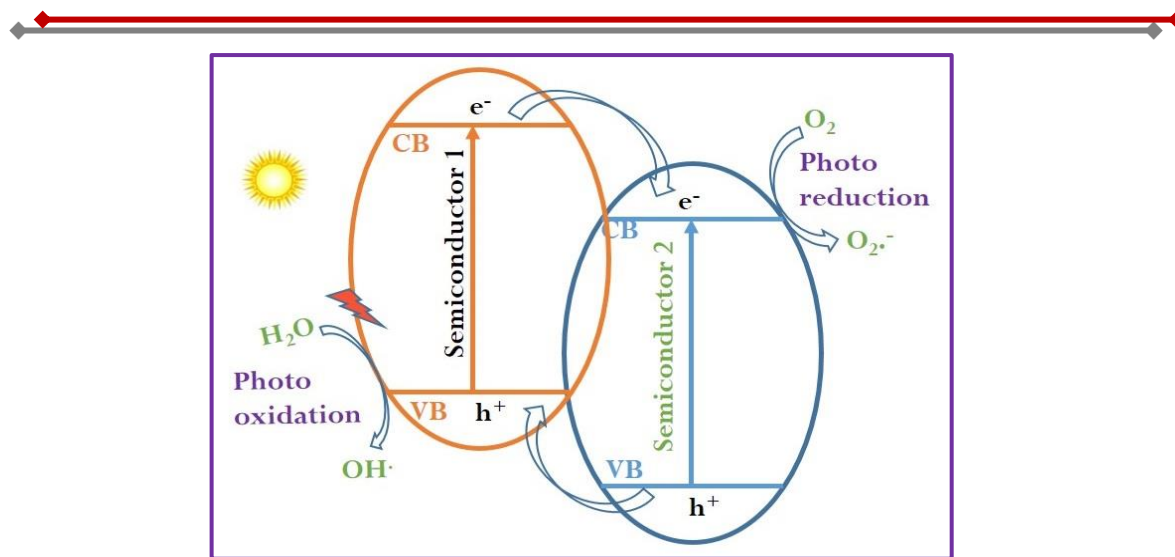


**Figure 1.8:** Schematic illustration for charge separation in semiconductor/semiconductor heterostructure

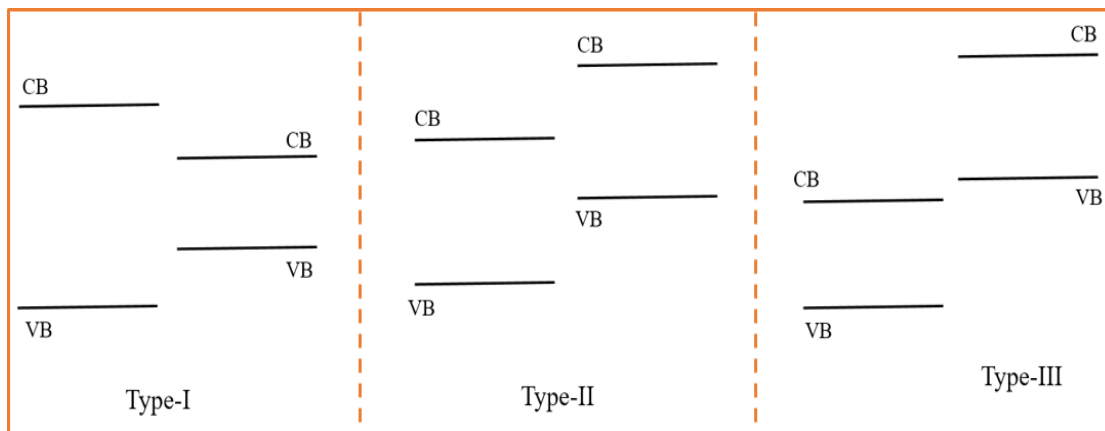


**Figure 1.9:** Different types of semiconductor heterojunction

## 1.5 Nanotechnology and photocatalysis

The term Nano is small. However, we know that “Small is beautiful”, but today the emerging nanotechnology has shown that small is not only beautiful but also powerful. Engineering materials at the nanoscale is of prime concern in the futuristic design of devices in electronics, catalysis, biomedical, sensors, medical diagnostics, and smart building materials, within the range of applications that nanoparticles find in varied fields of engineering and science.<sup>[78]</sup> Nanoparticles are particles that have at least one dimension in less than 100 nm range. Therefore, nanoparticles seem a promising option when compared to the conventional materials.

The following effects account for most of the special properties of nanomaterials in contrast to bulk materials:

- i. A number of surface atoms, which is a large fraction of the total atoms, makes a distinct contribution to the free energy and results in large changes in the thermodynamic properties (melting temperature depression, solid-solid phase transition elevation) of nanocrystals.<sup>[79–81]</sup>
- ii. The intrinsic properties of the nanocrystals are transformed by quantum size effect *i.e.* changes in the optical and electrical properties with a size which arise because of the variation in the density of electronic energy levels.<sup>[82]</sup>

In general, a real photocatalyst needs the close addition of three important components, including a light antenna, an oxidation catalyst and a reduction catalyst. In this favour, heterostructured materials have developed as the novel photocatalysts to produce solar energy because of their unique optical, chemical, and structural assets related to their bulk counterparts.<sup>[83–89]</sup> These diverse nanostructures (figure 1.10) such as nanotubes, nanosheets, porous nanospheres, nanoflowers, nanoplates, nanorods, nanoparticles, nanowires and other extra complex structures have been confirmed to show peculiar alternative properties, which can importantly develop the material selection and exposed a new degree of choice for the proposal of active photocatalytic systems.<sup>[90–94]</sup> For instance, nanostructured photocatalysts having a high surface area can contribute a large number of active sites for favorite electrochemical reactions. Morphology and size dependent assets, such as major confinement effects in nanostructured semiconductor and plasmonic absorption features in metallic nanostructures, can afford a new pathway to engineer the solar energy harvesting processes. Finally, the availability of a wide range of nanostructures can allow for incorporation of various efficient components to produce heterogeneous structures with unique characteristics or unprecedented performance. Therefore, development of semiconductor nanoarchitectures for the next generation highly efficient and stable visible light responsive photocatalyst is still being sought for the production of clean energy and green remediation.

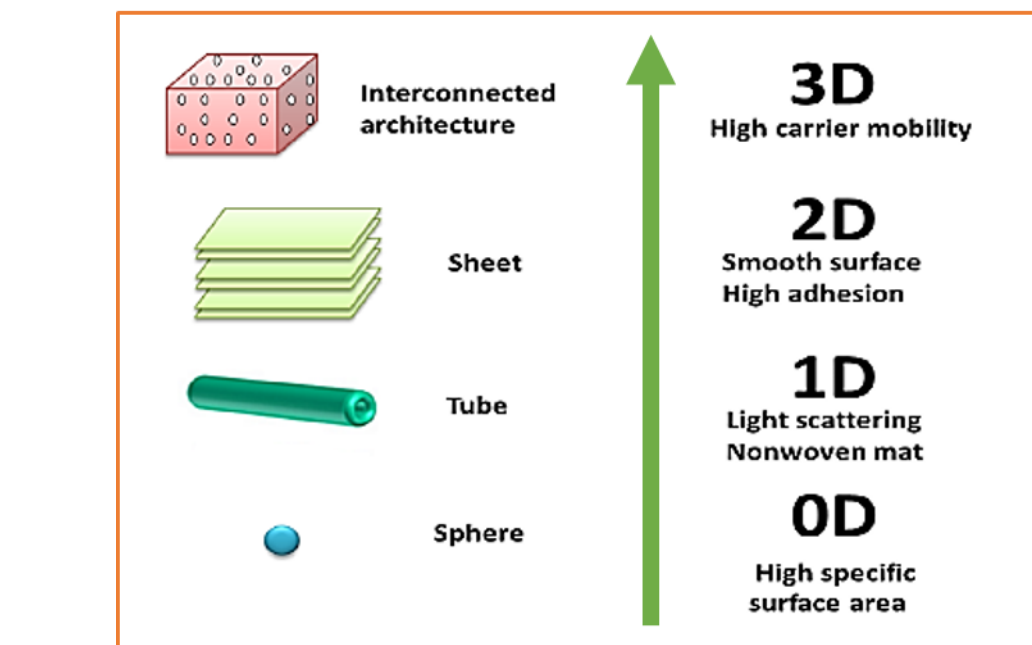


**Figure 1.10:** Different type of nanostructured materials

## 1.6 Synthesis of nanomaterials

There are two synthetic methods normally followed for the synthesis of nanomaterials: “top down” and “bottom up”. Both the approaches have been developed with a focus towards gaining a control over the particle size, size distribution, morphology and homogeneity. As the name suggests “top down” is essentially the breaking of the system till the nanosize is reached (e.g. ball milling and liquid exfoliation). While by “bottom up” we understand building up from the atomic or molecular precursor to form clusters and subsequently nanoparticles. However, synthesis of nanomaterials has been a challenging job for material scientists who have developed several new methods for obtaining monodispersed nanoparticles. The technique used for the preparation of nanomaterials depends on the interested material and size of the material. The great demand for fine particles of semiconductor materials has stimulated a lot of activity towards their synthesis by soft chemical techniques. There are some well known soft chemical techniques which are used for the synthesis of semiconductor nanomaterials. Among them, sol-gel, solvothermal, polymeric-precursor, hydrothermal technique and sonochemical approach are some of the commonly used methods.<sup>[95–100]</sup> Several points have to be considered for the utility of a particular synthetic methodology: (a) the range of applicability for different class of materials, (b) the reproducibility of average size and

shape of particles, (c) the control over the average particle size and range of sizes obtainable, and (d) the homogeneity of product phase. The basic principle for the synthesis of nanoparticles is to produce a large number of nuclei and to inhibit the growth and aggregation of grains. For a facile and effective control of particle size and crystalline phases, *in situ* precipitation strategy, which favours the formation of nanoparticles, was used in this research. Comparing with sol-gel or solid state reactions, the elimination of subsequent calculations greatly simplified the synthesis method. Furthermore, instead of conventional methods, a facile and environmental friendly self-assembly process was also employed to prepare the  $\text{Fe}_3\text{O}_4$ @titanosilicate/g-C<sub>3</sub>N<sub>4</sub> core-shell nanostructures. The Titanosilicate/BiVO<sub>4</sub> and Titanosilicate/Fe<sub>3</sub>O<sub>4</sub> hybrid nanocomposites synthesized via facile in-situ method. In addition, a facile ultrasonic dispersion method was used to synthesize composite samples. The detailed synthesis systems were discussed in the following chapters.

## 1.7 Characterization of materials

### 1.7.1 X-Ray diffraction (XRD)

XRD is one of the best methods for the quantitative and qualitative study of the solid phases and gives material information on the particle size of specific components. It is also employed to identify the material structure, different phases of transition, framework constants and external atoms occupied in the crystal framework of an active component of the catalyst. When combined with framework refinement methods, such as Rietveld refinement, it provides materials crystal structure. Powder XRD is a commonly used to finding the lattice strain in crystalline materials. XRD is based on the principle of Bragg's law (figure 1.11):<sup>[101]</sup>

$$n\lambda = 2d \sin\Theta \quad (1.18)$$

Where  $\lambda$  is the X-rays wavelength (1.5418 Å for Cu K $\alpha$ ) and  $d$  is the interplanar distance.

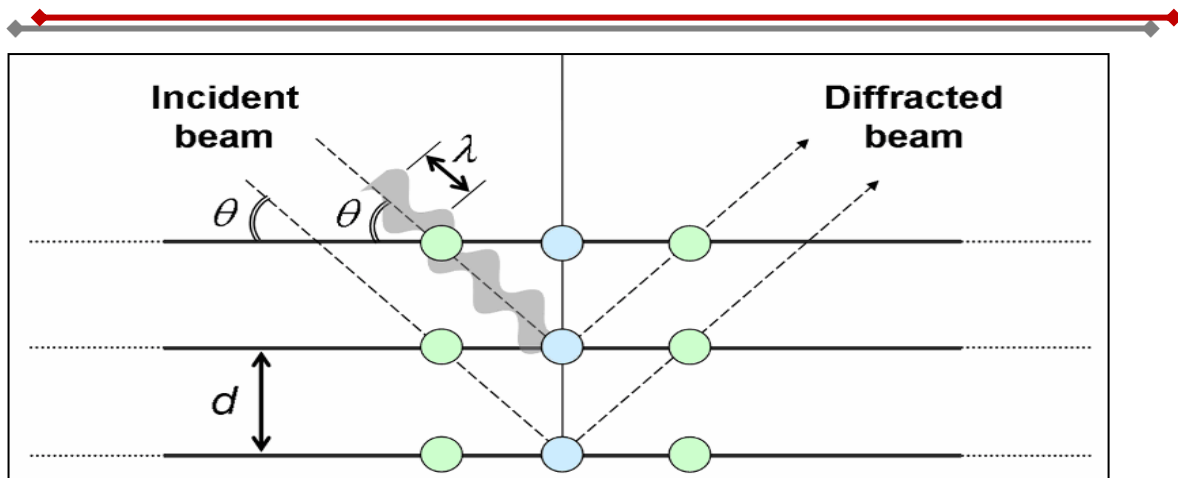


**Figure 1.11: Bragg's Law for X-ray diffraction**

The grain size can be determined from the broadening of the diffracted beam using the Scherrer's formula:

$$t = \frac{0.9\lambda}{B\cos\theta}$$

where,  $t$  = diameter of the grain,

$\lambda$  = wavelength of the X-ray (for Cu-K $\alpha$ ,  $\lambda = 1.5418 \text{ \AA}$ ),

$\Theta$  = Bragg angle or diffraction angle,

$B$  = Full width at half maximum (FWHM) of the diffraction peak,

The line broadening  $B$  is measured from the broaden peak at FWHM and obtained from Warren's formula:

$$B^2 = B_M^2 - B_S^2 \quad (1.20)$$

where  $B_M$  = FWHM of the sample

$B_S$  = FWHM of a standard sample of grain size of around  $2 \mu\text{m}$ .

### 1.7.2 Thermogravimetric analysis (TGA)

TGA is to define the changes in the weight of samples in relative to the variation in the temperature. The instrument generally contains a high-precision stability with a reference and a sample pan. The sample is placed in a small oven with a thermocouple to precisely analyze the temperature and purged with a N<sub>2</sub> or Ar gas to avoid oxidation reactions. The analysis is passed out by raising the temperature regularly and plotting weight vs temperature. As various weight loss curves look parallel, the weight loss curve may need conversion before results may be taken. TGA is usually working in scientific area and testing to define polymeric materials features, to describe degradation

temperatures, materials moisture content, the level of organic and inorganic constituents in materials, decomposition points of explosives, and residues of the solvent. It is also often used to estimate the corrosion kinetics at high temperature oxidation.<sup>[101]</sup>

### 1.7.3 Fourier transform infrared spectroscopy (FT-IR)

The infrared area of the electromagnetic spectrum includes radiation with wavelengths ranging from 1-1000 microns. This range is allocated to 3 regions; Far IR ( $200 - 10\text{ cm}^{-1}$ ), Mid IR ( $4000 - 200\text{ cm}^{-1}$ ) and Near IR ( $12500 - 4000\text{ cm}^{-1}$ ). The common analytical applications are limited to a portion of the middle region extending from 4000 to  $400\text{ cm}^{-1}$ . The absorption spectra in the infrared region originate from the transitions between vibrational (along with rotational) levels of a molecule present in its ground electronic state upon irradiation with infrared radiation.

The atoms in a molecule are never stationary and a good approximation is to treat them as a combination of point masses held together by Hooke's law of forces. By classical mechanics, it can be shown that the displacements of the masses from their mean positions are always the sum of the displacements due to a particular set of vibrations. If in these set of vibrations the masses are in phase and the motion of all the nuclei involved are such that the centre of gravity of the molecule remains unaltered, then such vibrations are known as the fundamental modes of vibration of the molecule. Mostly, a normal mode is localized largely to a group within the molecule and hence corresponds to stretching or bending of one or few bonds only and hence associated with that particular functional group. Whether for the functional group or the entire molecule, the vibrations are universally classified either as stretching or as bending types. Stretching vibrations, which correspond to the oscillations leading to a change in the bond lengths, can be further sub-divided into symmetric or asymmetric stretching vibrations. Bending vibrations are characterized by continuously changing the angle between the bonds and is further sub classified as wagging, rocking, twisting, or scissoring.

One of the primary requirements for vibrating molecules to interact with the oscillating electric field of the incident radiation and to undergo a transition between two vibrational energy levels is that the molecular dipole moment must change during the vibration. The intensity of the absorption is determined by the magnitude of this dipole

moment change. Owing to symmetry, some of the vibrations in a molecule may not induce a change in dipole moment and hence are transparent to infrared radiations *i.e.* IR inactive.

#### 1.7.4 UV–Visible diffuse reflectance spectroscopy (UV-Vis DRS)

UV–Vis DRS technique is, when a powdered sample irradiates with UV or visible light, the light can be reflected in all directions. Only the portion of light which is scattered within a solid sample and reverted to the surface is considered to be a diffuse reflection. The reflectance spectrum of a reference standard is barium sulphate ( $\text{BaSO}_4$ ), it must be recorded prior to that of any other powder sample.

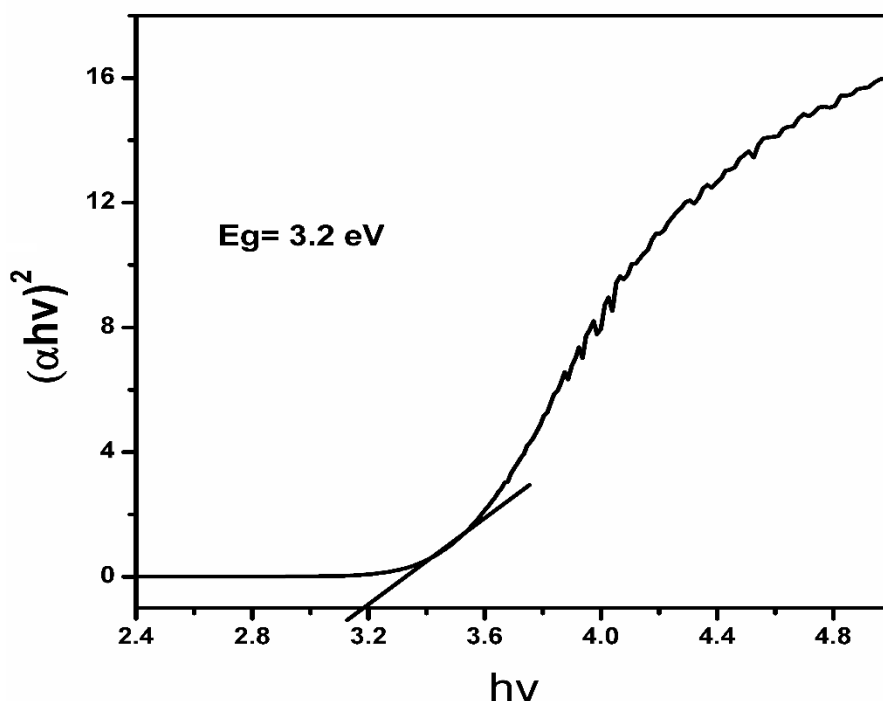


**Figure 1.12:** Determination of band gap energy using Kubelka–Munk function

An absorbance is usually definite as  $\log (I_o/I)$ , where  $I$  is transmitted light intensity and  $I_o$  is incident light intensity. The photoabsorption is measured in a reflection mode, such as  $\text{BaSO}_4$ , which can reflect the total incident light ( $I_o$ ), *i.e.* 100% reflection. The semiconductor band gap energy can be determined by the following formula:

$$\alpha h\nu = A(h\nu - E_g)^\eta \quad (1.21)$$

Where,  $A$  is constant,  $h$  is Planck's constant,  $E_g$  is band gap energy,  $\alpha$  is absorption coefficient, and  $\nu$  is light frequency. The variable  $\eta$  depends on the type of the optical

transition caused by photon absorption.  $E_g$  (band gap) can be expected according to a plot of  $(ahv)^2$  Vs energy ( $h\nu$ ). The  $\alpha$  was determined from the Kubelka–Munk function: [102]

$$\alpha = \frac{(1 - R)^2}{2R}$$

where,  $\alpha$  is the reflection coefficient of the sample and  $R$  is the reflectance

### 1.7.5 Scanning electron microscopy (SEM)

SEM is the powerful technique that is classified under scanning probe microscopy (SPM); it uses a focused beam of high energy electrons to give the morphological structure of the compound by scanning. The electrons collision with atoms in the compound surface gives several signals that can be observed. It gives information about the sample including external morphological structure, elemental composition and orientation of materials making up the sample. Finally, data is collected over a particular area of the compound, 2D image is generated.

#### 1.7.5.1 Basic components of SEM

SEM is an instrument with an electron producing factor called the electron gun, the electron beam travels through a column, the shape of the electron beam is set by a series of lenses, the sample compartment at the base and a series of pumps create a vacuum in the system.

#### 1.7.5.2 Basic operation principle of SEM

SEM facilitates the analysis of samples with a resolution down to the nanometre scale. Accelerated electrons from the gun and it is focused on the surface of the solid compound through the column and lenses. The electron-sample interaction produces a variety of signal when the incident electrons are decelerated. These signals include: secondary electrons (that produce SEM images) –

- ❖ Secondary electrons are normally used for imaging samples: They are more valuable for showing topography and morphology on samples.
- ❖ Backscattered electrons (BSE) – are also used for imaging samples. They are more valuable for showing differences in composition in multiphase samples

- ❖ Diffracted backscattered electrons – are used to define crystal structures and orientations of minerals
- ❖ Photons – these are characteristic X-ray that is used for elemental analysis
- ❖ Visible light – Cathode luminescence (CL) and heat

#### 1.7.6 Transmission electron microscopy (TEM)

Transmission electron microscopy (TEM) is a scanning probe microscopy (SPM) technique in which electrons beam having the energy of the order of hundreds of KeV is transmitted over an ultra-thin sample, interacting with the sample as it passes through to provide morphological, topographical, compositional and crystallographic information of the sample. An image is obtained from the interaction between electrons and sample; the image has magnified an image is captured by a sensor.

High-resolution TEM allows the researchers to outlook samples on a molecular level in the order of a few angstroms ( $10^{-10}$  m), making it possible to analyze structure and texture at a significantly high resolution. The TEM operates nearly on the equal basic principles as SEM as both use electrons.

#### 1.7.7 Energy dispersive X-ray spectroscopy (EDS)

Energy Dispersive X-ray Spectroscopy (EDS) is a quantitative and qualitative X-ray micro analytical technique that can provide information about the chemical composition of a sample. A beam of electron is directed on the compound in either SEM or a TEM. The primary beam of electrons penetrate the compound and interrelate with the compositional atoms. From these interactions X-rays divided into two types: Bremsstrahlung X-rays, which means “braking radiation” also denoted as background X-rays and characteristic X-rays. The X-rays are recorded by an Energy Dispersive detector which shows the signal as a spectrum.

Energy dispersive X-ray spectroscopy (EDS) coupled with a transmission electron microscope with high resolution is one of the most revealing analytical methods for analyzing the composition of nanomaterials. It uses the X-ray spectrum emitted by a solid compound collision with a focused electron beam, to obtain an elemental composition of the compound.

- ❖ The qualitative analysis contains the identification of the outlines in the spectrum and is properly straight forward being to the simplicity of X-ray spectra.
- ❖ Quantitative analysis involves evaluating each element line intensities in the compound and for the same elements in calibration standards of known composition.

### 1.7.8 Surface area analysis

BET (Brunauer–Emmett–Teller) is one of the best technique for the determination of the compound surface area by physical adsorption of gas molecules on the surface. The BET theory was proposed by Stephen Brunauer, Paul Hugh Emmett and Edward Teller in 1938. The Langmuir theory was extended from this BET theory, which is a theory for monolayer molecular adsorption, to multilayer adsorption with the resulting theories: (a) gas molecules physically adsorb on a solid in layers considerably; (b) there is no contact between each adsorption layer; and (c) the Langmuir theory can be functional to each layer. The resulting BET equation is expressed by:

$$\frac{1}{v(\frac{P_0}{P}-1)} = \frac{1}{v_m} \left( \frac{P}{P_0} \right) + \frac{1}{v_m} \quad (1.27)$$

$P_0$  is the saturation pressure and  $P$  is the equilibrium pressure of adsorbates,  $v$  is the adsorbed gas quantity (for ex. in volume units),  $v_m$  is the adsorbed gas quantity of the monolayer.

### 1.7.9 Fluorescence spectroscopy

Fluorescence is the best technique of study where the molecules of the analyte are migrated by a certain wavelength of the light irradiation and emits a different wavelength radiation. The emission spectrum thus gives evidence for both quantitative and qualitative analysis. Fluorescence spectroscopy is mainly concerned with the electronic and vibrational states. The procedures which happen among the emission and absorption of light are regularly verified by a Jablonski diagram named after Prof Alexander Jablonski, regarded as the father of fluorescence.

At each of these electronic energy levels, the fluorophores can occur in a number of vibrational energy levels, depicted by 0, 1, 2, etc. The excited electronic state is

generally the first excited singlet state,  $S_1$  (figure 1.13). Once, the molecule reaches this excited state, relaxation can occur via several pathways. Fluorescence is one of these methods which results in the emission of light. An essential pathways are:

1. Collisional deactivation leading to non-radiative relaxation.
2. Intersystem crossing ( $10^{-9}$ s): Molecules in the  $S_1$  state can also undergo a spin conversion to the first triplet state  $T_1$ . This conversion of  $S_1$  to  $T_1$  is called intersystem crossing.
3. Phosphorescence: The relaxation of the molecule from the  $T_1$  state to the  $S_0$  state with emission of light is called as phosphorescence. This is an obviously forbidden transition and thus the  $T_1$  state has a more lifetime and the phosphorescence rate is low (10 to 100 sec).
4. Fluorescence: This resembles to the relaxation of the molecule from the  $S_1$  state to the  $S_0$  state with emission of light is called as fluorescence and it has a short lifetime ( $\sim 10$  sec). The wavelength of the light emitted is dependent on the energy gap between the ground state and the  $S_1$  state. An overall energy balance for the fluorescence process could be written as:

$$E_{\text{fluor}} = E_{\text{abs}} - E_{\text{vib}} - E_{\text{solv. relax}} \quad (1.31)$$

Where,  $E_{\text{fluor}}$  is the emitted light energy,  $E_{\text{abs}}$  is the absorbed light energy by the molecule during excitation, and  $E_{\text{vib}}$  is the molecule energy is lost from vibrational relaxation. The  $E_{\text{solv. relax}}$  is the solvent cage of the molecule in the excited state and then again molecule relaxes to the ground state. For a given molecule, absorption energy is always greater than the fluorescence energy. Thus the emitted light is observed at longer wavelengths than the excitation. This is known as Stokes' shift.

5. Internal Conversion: Molecules in reduced phases quickly relax to the bottom vibrational level of  $S_1$ . This phenomenon is called internal conversion and normally happens within  $10^{-12}$  s or less. Since fluorescence lifetimes are naturally near  $10^{-8}$  s, internal conversion is usually finished prior to emission are internal conversion processes.

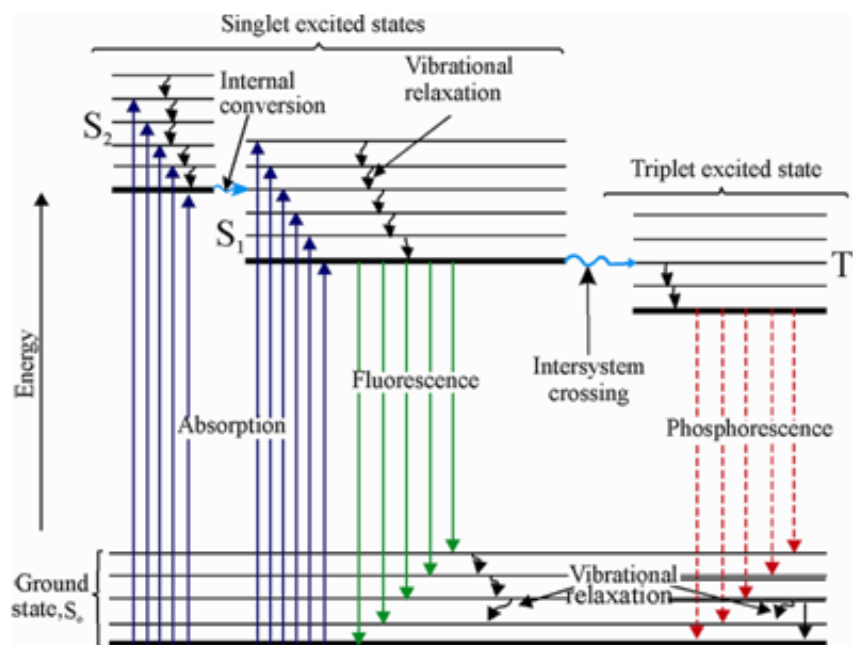


**Figure 1.13:** Electronic transition energy level diagram: Jablonski diagram

### 1.8 Photocatalytic properties (photodegradation of dye)

For the last several decades, environmental pollution has become an increasing concern on a global scale. Therefore the development of environmental pollutant remediation and clean technologies is vital. One class of pollutant is organic contaminants in aqueous systems, which includes wastewater from pharmaceuticals, pesticides, packaging, and textile dyeing. Dyes alone account for approximately 700,000 tons per year of waste. This waste contains over 100,000 different organic compounds, of which, more than half are highly toxic azo dyes.<sup>[103]</sup> These widespread pollution warrants search for an environmentally friendly, large scale, commercially applicable process. Photocatalytic application on entire degradation of organic pollutants from polluted water and effluents. Unlike the conservative biodegradable and activated carbon adsorption method, photocatalysis proposes a great oxidation in the treatment of bioresistant organic contaminants such as dye solution by converting them into water and Carbon dioxide.

To expand the application of photocatalysts, Rhodamine B (RhB), methylene blue (MB) were selected as an organic pollutant for the study of photocatalytic activity. The photocatalytic performance of the synthesized photocatalysts was examined for degradation of RhB solution under light irradiation. Photocatalytic experiments of all the samples were conducted under similar conditions at NIT Warangal, during 11.00 am to

4.00 pm. The UV light source is Hg lamp (400 W). In each experiment, 0.1 g of photocatalyst was added to 250 mL RhB/MB solution with a concentration of 5 or 10 mg L<sup>-1</sup>. Prior to irradiation, the solution was allowed to stir for 30 min in the dark to create an adsorption-desorption equilibrium. During photocatalytic processes, the sample was from time to time withdrawn, centrifuged to discrete the catalyst from the dye solution. The RhB or MB concentration was observed by UV–Vis spectrophotometer.

**Table 1.1:** literature of the photocatalytic dye degradation on porous materials

S. No.	Porous nanocomposite	Synthesis Method	Dye	Light source	Degradation /min
1.	Mesoporous titanosilicate/reduced graphene oxide	Hydrothermal	Methylene blue	UV (20 W black light, 365)	98%, 60 min <sup>104</sup>
2	Controllable Pt/ZnO Porous Nanocages	ultrasonic irradiation	Methyl orange	UV (125 W 365 nm)	97%, 90 min <sup>86</sup>
3	Mesoporous Ce <sub>0.49</sub> Zr <sub>0.37</sub> Bi <sub>0.14</sub> O <sub>1.93</sub>	general polymerization–carbonization–oxidation	Methyl orange	300 W Xe lamp	98%, 60 min <sup>92</sup>
4	macro/mesoporous g-C <sub>3</sub> N <sub>4</sub> /TiO <sub>2</sub>	Calcining of the mixtures	Rhodamine B	350 W Xe lamp	98%, 80 min <sup>105</sup>
5	titania supported nanoporous MCM-41	Hydrothermal	Methyl orange	150 W Xe lamp, 466 nm	80%, 60 min <sup>106</sup>
6	Highly ordered Ti-SBA-15:	Hydrothermal	Methylene blue	A 450W mercury-lamp	87.1%, 120 min <sup>107</sup>
7	porous Fe <sub>3</sub> O <sub>4</sub> /g-C <sub>3</sub> N <sub>4</sub>	Hydrothermal	Methyl orange	150W Xe lamp	98%, 150 min <sup>108</sup>
8	graphene oxide/TiO <sub>2</sub>	In-situ	Methyl orange	20W UV lamp	98%, 9 min <sup>109</sup>
9	Ag <sub>3</sub> PO <sub>4</sub> /TiO <sub>2</sub> mesoporous spheres	sol–gel and solvothermal	Methylene blue	150W Xe lamp	99%, 28 min <sup>110</sup>
10	Graphene-modified nanosized Ag <sub>3</sub> PO <sub>4</sub>	In-situ	Methylene blue	350W Xe arc lamp	97%, 20 min <sup>111</sup>

**Literature review:**

Mesoporous titanosilicate/reduced graphene oxide synthesized via Hydrothermal method with different molar ratios and methylene blue degradation under UV light within 60 min reported by T.D. Nguyen-Phan et al.<sup>104</sup> H. Tong et al. reported controllable Pt/ZnO porous nanocages via ultrasonication method and degradation of methyl orange within 90 min under UV light irradiation.<sup>86</sup> Z. Liu et. al. has been reported mesoporous Ce<sub>0.49</sub>Zr<sub>0.37</sub>Bi<sub>0.14</sub>O<sub>1.93</sub> prepared through general polymerization-carbonization-oxidation route and photocatalytic activity with methyl orange under Xe lamp within 60 min.<sup>92</sup> Macro/mesoporous g-C<sub>3</sub>N<sub>4</sub>/TiO<sub>2</sub> synthesized via calcination of the mixture and degradation of rhodamine B under 350W Xe lamp within 80 min was reported by R. Hao et al.<sup>105</sup> Ti-MCM-41 synthesized via hydrothermal method and methylene blue degradation under 150W Xe lamp within 60 min reported by S. anandan et al.<sup>106</sup> S. K. Das et al. reported highly ordered Ti-SBA-15 and degradation of methylene blue under 450W mercury lamp within 120 min.<sup>107</sup> porous Fe<sub>3</sub>O<sub>4</sub>/g-C<sub>3</sub>N<sub>4</sub> photocatalyst synthesized via hydrothermal method and degradation of methyl orange under 150W Xe lamp reported by Xi. Zhou et. al.<sup>108</sup> G. Jiang et. al. reported by graphene oxide/TiO<sub>2</sub> via insitu method and degradation of methyl orange under 20W UV light within 9 min.<sup>109</sup> Ag<sub>3</sub>PO<sub>4</sub>/TiO<sub>2</sub> mesoporous spheres synthesized via sol-gel and solvothermal method and degradation of methylene blue under 150W Xe lamp within 28 min Y. Li et. al. reported.<sup>110</sup> Q. Xiang et. al. reported Graphene-modified nanosized Ag<sub>3</sub>PO<sub>4</sub> and degradation of methylene blue under 350W Xe lamp within 20min.<sup>111</sup>

**Table 1.2:** Information available on characterization by various technics.

S. No.	Characterization	Observed information
1.	Powder X-ray diffraction	Phase purity, symmetry, mesoporosity
2.	Field emission – Scanning electron microscopy/Dispersive X-ray Analysis	Particle size, shape and Surface elemental composition
3.	Transmission electron microscopy	Mesoporosity, Particle size and shape.
4.	Thermogravimetry	Weight loss with respect to temperature
5.	Fourier transform Infrared spectroscopy	Framework structure, and Transition metal incorporation in basic framework.
6.	Ultraviolet – visible Diffuse reflectance spectroscopy.	Band gap, Transition metal ion incorporation, its co-ordination and oxidation state.

7.	Photoluminescence spectroscopy	Emission spectra of the luminescent compound.
8.	Ultraviolet – visible spectrophotometer.	To estimate the concentration of dye in test sample.

## 1.9 References

- [1] A. L. Linsebigler, G. Lu, J. T. Yates, *Chem. Rev.* **1995**, *95*, 735.
- [2] P. V. Kamat, *Chem. Rev.* **1993**, *93*, 267.
- [3] A. Mills, S. Le Hunte, *J. Photochem. Photobiol. A Chem.* **1997**, *108*, 1.
- [4] M. R. Hoffmann, S. T. Martin, W. Choi, D. W. Bahnemann, *Chem. Rev.* **1995**, *95*, 69.
- [5] A. Fujishima, honda kenichi, *Nature* **1972**, *238*, 37.
- [6] A. Fujishima, T. N. Rao, D. A. Tryk, *J. Photochem. Photobiol. C Photochem. Rev.* **2000**, *1*, 1.
- [7] K. Domen, S. Naito, M. Soma, T. Onishi, K. Tamaru, *J. Chem. Soc., Chem. Commun.* **1980**, 543.
- [8] J. Zhao, X. Yang, *Build. Environ.* **2003**, *38*, 645.
- [9] S. Rehman, R. Ullah, A. M. Butt, N. D. Gohar, *J. Hazard. Mater.* **2009**, *170*, 560.
- [10] Z. Yi, J. Ye, N. Kikugawa, T. Kako, S. Ouyang, H. Stuart-Williams, H. Yang, J. Cao, W. Luo, Z. Li, Y. Liu, R. L. Withers, *Nat. Mater.* **2010**, *9*, 559.
- [11] R. M. Mohamed, D. L. McKinney, W. M. Sigmund, *Mater. Sci. Eng. R Reports* **2012**, *73*, 1.
- [12] D. Bahnemann, *Sol. Energy* **2004**, *77*, 445.
- [13] a) P. H. Muller, “The Nobel Prize in Physiology or Medicine 1948,” **1948**. b) Roy R, Roy RA, Roy DM. *Materials Letters*. **1986**, *4*, 323. c) Schmidt D, Shah D, Giannelis EP. *Current Opinion in Solid State & Materials Science* **2002**, *6*, 205. d) Gleiter H. *Nanostructured Materials*. **1992**, *1*, 1
- [14] Qamar, M. Saquib, M. Muneer, *Dye. Pigment.* **2005**, *65*, 1.
- [15] L. B. Reutergådh, M. Iangphasuk, *Chemosphere* **1997**, *35*, 585.
- [16] I. K. Konstantinou, T. A. Albanis, *Appl. Catal. B Environ.* **2004**, *49*, 1.
- [17] T. Van Gerven, G. Mul, J. Moulijn, A. Stankiewicz, *Chem. Eng. Process. Process Intensif.* **2007**, *46*, 781.
- [18] D. Ljubas, *Energy* **2005**, *30*, 1699.

[19] Q. Zhang, J. Wang, S. Yin, T. Sato, F. Saito, *J. Am. Ceram. Soc.* **2004**, 87, 1161.

[20] J. M. Herrmann, *Top. Catal.* **2005**, 34, 49.

[21] K. Pirkanniemi, M. Sillanpää, *Chemosphere* **2002**, 48, 1047.

[22] Y. Liang, H. Wang, H. Sanchez Casalongue, Z. Chen, H. Dai, *Nano Res.* **2010**, 3, 701.

[23] P. R. Gogate, A. B. Pandit, *Adv. Environ. Res.* **2004**, 8, 501.

[24] M. Litter, *Appl. Catal. B Environ.* **1999**, 23, 89.

[25] J. Herrmann, *Catal. Today* **1999**, 53, 115.

[26] S. Anandan, N. Ohashi, M. Miyauchi, *Appl. Catal. B Environ.* **2010**, 100, 502.

[27] Y. Li, J. Wang, H. Yao, L. Dang, Z. Li, *J. Mol. Catal. A Chem.* **2011**, 334, 116.

[28] O. M. Alfano, D. Bahnemann, A. E. Cassano, R. Dillert, R. Goslich, *Catal. Today* **2000**, 58, 199.

[29] D. F. Ollis, E. Pelizzetti, N. Serpone, *Environ. Sci. Technol.* **1991**, 25, 1522.

[30] M. Qamar, S. J. Kim, a K. Ganguli, *Nanotechnology* **2009**, 20, 455703.

[31] U. I. Gaya, A. H. Abdullah, *J. Photochem. Photobiol. C Photochem. Rev.* **2008**, 9, 1.

[32] R. Thiruvenkatachari, S. Vigneswaran, I. S. Moon, *Korean J. Chem. Eng.* **2008**, 25, 64.

[33] K. Kabra, R. Chaudhary, R. L. Sawhney, *Ind. Eng. Chem. Res.* **2004**, 43, 7683.

[34] S. Mozia, *Sep. Purif. Technol.* **2010**, 73, 71.

[35] C. TURCHI, D. F. OLLIS, *J. Catal.* **1990**, 122, 178.

[36] C. a. Linkous, G. J. Carter, D. B. Locuson, A. J. Ouellette, D. K. Slattery, L. a. Smitha, *Environ. Sci. Technol.* **2000**, 34, 4754.

[37] M. D. Hernández-Alonso, F. Fresno, S. Suárez, J. M. Coronado, *Energy Environ. Sci.* **2009**, 2, 1231.

[38] M. Vautier, C. Guillard, J.-M. Herrmann, *J. Catal.* **2001**, 201, 46.

[39] M. Ni, M. K. H. Leung, D. Y. C. Leung, K. Sumathy, *Renew. Sustain. Energy Rev.* **2007**, 11, 401.

[40] G. Liu, L. Wang, H. G. Yang, H.-M. Cheng, G. Q. (Max) Lu, *J. Mater. Chem.* **2010**, 20, 831.

[41] S. N. Frank, A. J. Bard, *J. Am. Chem. Soc.* **1977**, 99, 303.

[42] M. N. Chong, B. Jin, C. W. K. Chow, C. Saint, *Water Res.* **2010**, 44, 2997.

[43] W. Liu, M. Wang, C. Xu, S. Chen, *Chem. Eng. J.* **2012**, 209, 386.

[44] K. Nakata, A. Fujishima, *J. Photochem. Photobiol. C Photochem. Rev.* **2012**, *13*, 169.

[45] R. Vinu, M. Giridhar, *J. Indian Inst. Sci.* **2010**, *90*, 189.

[46] Y. Zhang, Q. Pan, G. Chai, M. Liang, G. Dong, Q. Zhang, J. Qiu, *Sci. Rep.* **2013**, *3*, 1.

[47] N. Xiao, D. Lau, W. Shi, J. Zhu, X. Dong, H. H. Hng, Q. Yan, *Carbon N. Y.* **2013**, *57*, 184.

[48] A. Fujishima, X. Zhang, D. Tryk, *Int. J. Hydrogen Energy* **2007**, *32*, 2664.

[49] F. Méndez-Hermida, E. Ares-Mazás, K. G. McGuigan, M. Boyle, C. Sichel, P. Fernández-Ibáñez, *J. Photochem. Photobiol. B Biol.* **2007**, *88*, 105.

[50] J. Llonen, S. Kilvington, S. C. Kehoe, F. Al-Touati, K. G. McGuigan, *Water Res.* **2005**, *39*, 877.

[51] W. Kangwansupamonkon, V. Lauruengtana, S. Surassmo, U. Ruktanonchai, *Nanomedicine Nanotechnology, Biol. Med.* **2009**, *5*, 240.

[52] Y. Liu, L. Xie, Y. Li, R. Yang, J. Qu, Y. Li, X. Li, *J. Power Sources* **2008**, *183*, 701.

[53] S. Koide, T. Nonami, *Food Control* **2007**, *18*, 1.

[54] S. Malato, P. Fernández-Ibáñez, M. I. Maldonado, J. Blanco, W. Gernjak, *Catal. Today* **2009**, *147*, 1.

[55] T. Puangpetch, T. Sreethawong, S. Yoshikawa, S. Chavadej, *J. Mol. Catal. A Chem.* **2009**, *312*, 97.

[56] C. Ooka, H. Yoshida, K. Suzuki, T. Hattori, *Microporous Mesoporous Mater.* **2004**, *67*, 143.

[57] J.-Y. Lee, J. Park, J.-H. Cho, *Appl. Phys. Lett.* **2005**, *87*, 11904.

[58] K. Yang, Y. Dai, B. Huang, *Phys. Rev. B* **2007**, *76*, 195.

[59] E. Finazzi, C. Di Valentin, G. Pacchioni, *J. Phys. Chem. C* **2009**, *113*, 220.

[60] R. Asahi, T. Morikawa, T. Ohwaki, K. Aoki, Y. Taga, *Science (80-. ).* **2001**, *293*, 269.

[61] M. Batzill, E. H. Morales, U. Diebold, *Phys. Rev. Lett.* **2006**, *96*, 26103.

[62] S. Livraghi, M. C. Paganini, E. Giannello, A. Selloni, C. Di Valentin, G. Pacchioni, *J. Am. Chem. Soc.* **2006**, *128*, 15666.

[63] X. Zong, Z. Xing, H. Yu, Z. Chen, F. Tang, J. Zou, G. Q. Lu, L. Wang, *Chem. Commun.* **2011**, *47*, 11742.

[64] R. Long, N. J. English, *Chem. Phys. Lett.* **2009**, *478*, 175.

[65] M. Grätzel, *J. Photochem. Photobiol. C Photochem. Rev.* **2003**, *4*, 145.

[66] J. Moon, C. Y. Yun, K.-W. Chung, M.-S. Kang, J. Yi, *Catal. Today* **2003**, *87*, 77.

[67] D. Chatterjee, S. Dasgupta, *J. Photochem. Photobiol. C Photochem. Rev.* **2005**, *6*, 186.

[68] Y. Tian, T. Tatsuma, *J. Am. Chem. Soc.* **2005**, *127*, 7632.

[69] M. D. Driessens, V. H. Grassian, *J. Phys. Chem. B* **1998**, *102*, 1418.

[70] H. Zhang, C. Liang, J. Liu, Z. Tian, G. Wang, W. Cai, *Langmuir* **2012**, *28*, 3938.

[71] J. JANG, H. KIM, U. JOSHI, J. JANG, J. LEE, *Int. J. Hydrogen Energy* **2008**, *33*, 5975.

[72] Y. Wang, R. Shi, J. Lin, Y. Zhu, *Energy Environ. Sci.* **2011**, *4*, 2922.

[73] L. Spanhel, H. Weller, A. Henglein, *J. Am. Chem. Soc.* **1987**, *109*, 6632.

[74] H. Fu, T. Xu, S. Zhu, Y. Zhu, *Environ. Sci. Technol.* **2008**, *42*, 8064.

[75] X. Wang, K. Maeda, A. Thomas, K. Takanabe, G. Xin, J. M. Carlsson, K. Domen, M. Antonietti, *Nat. Mater.* **2009**, *8*, 76.

[76] Z. Yi, J. Ye, N. Kikugawa, T. Kako, S. Ouyang, H. Stuart-Williams, H. Yang, J. Cao, W. Luo, Z. Li, Y. Liu, R. L. Withers, *Nat. Mater.* **2010**, *9*, 559.

[77] Y. Wang, Q. Wang, X. Zhan, F. Wang, M. Safdar, J. He, *Nanoscale* **2013**, *5*, 8326.

[78] M. Anpo, T. Shima, S. Kodama, Y. Kubokawa, *J. Phys. Chem.* **1987**, *91*, 4305.

[79] A. J. Hoffman, H. Yee, G. Mills, M. R. Hoffmann, *J. Phys. Chem.* **1992**, *96*, 5540.

[80] A. Henglein, *Q-Particles: Size Quantization Effects in Colloidal Semiconductors*, Steinkopff, Darmstadt, **1987**.

[81] Q. Li, B. Yue, H. Iwai, T. Kako, J. Ye, *J. Phys. Chem. C* **2010**, *114*, 4100.

[82] P. V. Kamat, *J. Phys. Chem. C* **2007**, *111*, 2834.

[83] X. Chen, S. S. Mao, *Chem. Rev.* **2007**, *107*, 2891.

[84] D. Chen, J. Ye, *Chem. Mater.* **2009**, *21*, 2327.

[85] G. Xi, B. Yue, J. Cao, J. Ye, *Chem. - A Eur. J.* **2011**, *17*, 5145.

[86] H. Tong, J. Ye, *Eur. J. Inorg. Chem.* **2010**, 1473.

[87] D. Chen, J. Ye, *Adv. Funct. Mater.* **2008**, *18*, 1922.

[88] G. Xi, J. Ye, *Chem. - A Eur. J.* **2010**, *16*, 8719.

[89] H. Tong, S. Ouyang, Y. Bi, N. Umezawa, M. Oshikiri, J. Ye, *Adv. Mater.* **2012**, *24*, 229.

[90] S. Wohlrab, M. Weiss, H. Du, S. Kaskel, *Chem. Mater.* **2006**, *18*, 4227.

[91] K. Maeda, T. Takata, M. Hara, N. Saito, Y. Inoue, H. Kobayashi, K. Domen, *J.*

*Am. Chem. Soc.* **2005**, *127*, 8286.

[92] Z. Liu, H. Bai, S. Xu, D. D. Sun, *Int. J. Hydrogen Energy* **2011**, *36*, 13473.

[93] L. Zhang, H. Cheng, R. Zong, Y. Zhu, *J. Phys. Chem. C* **2009**, *113*, 2368.

[94] H. Zeng, W. Cai, P. Liu, X. Xu, H. Zhou, C. Klingshirn, H. Kalt, *ACS Nano* **2008**, *2*, 1661.

[95] H. Zhang, G. Chen, *Environ. Sci. Technol.* **2009**, *43*, 2905.

[96] J. Liao, L. Shi, S. Yuan, Y. Zhao, J. Fang, *J. Phys. Chem. C* **2009**, *113*, 18778.

[97] P. R. Arya, P. Jha, A. K. Ganguli, *J. Mater. Chem.* **2003**, *13*, 415.

[98] M. a Alpuche-Aviles, Y. Wu, *J. Am. Chem. Soc.* **2009**, *131*, 3216.

[99] W. Yin, X. Chen, M. Cao, C. Hu, B. Wei, *J. Phys. Chem. C* **2009**, *113*, 15897.

[100] A. Morel, S. I. Nikitenko, K. Gionnet, A. Wattiaux, J. Lai-Kee-Him, C. Labrugere, B. Chevalier, G. Deleris, C. Petibois, A. Brisson, M. Simonoff, *ACS Nano* **2008**, *2*, 847.

[101] L. S. Birks, H. Friedman, *J. Appl. Phys.* **1946**, *17*, 687.

[102] D. G. Barton, M. Shtein, R. D. Wilson, S. L. Soled, E. Iglesia, *J. Phys. Chem. B* **1999**, *103*, 630.

[103] T. Robinson, G. McMullan, R. Marchant, P. Nigam, *Bioresour. Technol.* **2001**, *77*, 247.

[104] T.-D. Nguyen-Phan, E. W. Shin, V. H. Pham, H. Kweon, S. Kim, E. J. Kim, J. S. Chung, *J. Mater. Chem.* **2012**, *22*, 20504.

[105] R. Hao, G. Wang, H. Tang, L. Sun, C. Xu, D. Han, *Appl. Catal. B Environ.* **2016**, *187*, 47.

[106] S. Anandan, *Dye. Pigment.* **2008**, *76*, 535–541.

[107] S. K. Das, M. K. Bhunia, and A. Bhaumik, *J. solid State chem.*, **2010** *183*, 1326.

[108] Xi. Zhou, B. Jin, R. Chen, F. Peng, and Y. Fang, *Materials Research Bulletin*, **2013**, *48*, 1447.

[109] G. Jiang, Z. Lin, C. Chen, Li. Zhu, Q. Chang, N. Wang, W. Wei, and H. Tang, *Carbon*, **2011**, *49*, 2693.

[110] Y. Li, Li. Yu, N. Li, W. Yan, and X. Li, *J. Coll. Int. Sci.*, **2015**, *450*, 246.

[111] Q. Xiang, D. Lang, T. Shen, and F. Liu, *Appl. Cat. B: Env.*, **2015**, *162*, 196.

## CHAPTER II

Development of novel porous  
Titanosilicate/g- $C_3N_4$  nanocomposites for  
Photocatalytic degradation of Rhodamine-B  
under direct sunlight irradiation



## 2 Development of novel porous Titanosilicate/g-C<sub>3</sub>N<sub>4</sub> nanocomposites for Photocatalytic degradation of Rhodamine-B under direct sunlight irradiation

### 2.1 Introduction

In modern years, the improvement of green, renewable energy sources is of essential importance to address the forthcoming world-wide demand of a carbon-neutral energy cycle.<sup>[1-3]</sup> In this regard, several highly active semiconductor photo-catalysts were employed for renewable clean energy and environmental remediation. Photocatalytic technology is widely employed for hydrogen evolution from water splitting and degradation of organic pollutants in water/air as solar energy is renewable. So far many impressive semiconductor photo-catalysts have been explored and have shown enhanced photoreactivity.<sup>[4-8]</sup> Besides exploring new materials, developing technologies to increase the reactivity and recyclability of known photo-catalysts is also attractive.<sup>[9-13]</sup> Therefore, exploitation of active visible light driven photo-catalysts is of today's demand.

Heterogeneous catalysts based on titanium containing mesoporous materials have excellent catalytic activity due to their unique structural features like exceptionally high surface area, uniform and well defined pore topology since the discovery of titanosilicate 1983.<sup>[14,15]</sup> A variety of Ti incorporated mesoporous silicates such as ETS-10, Ti-SBA-15, Ti-MCM-41 have been synthesized, which shows photocatalytic activity, selectivity in oxidation reactions, adsorptions studies. So many researchers have widely reported titaniumsilicates as an efficient photocatalytic semiconductor materials have been widely reported.<sup>[16-25]</sup>

On the other hand, g-C<sub>3</sub>N<sub>4</sub> (CN) a hetero atom-planar sheet of sp<sup>2</sup> bonded carbon and nitrogen atoms has emerged as one of the most exciting materials since its experimental discovery in 2004.<sup>[26]</sup> The metal free g-C<sub>3</sub>N<sub>4</sub> semiconductor possesses suitable band gap, very high thermal and chemical stability. The g-C<sub>3</sub>N<sub>4</sub> is a good photocatalytic semiconductor for the RhB degradation studies under visible light irradiation. The efficiency of g-C<sub>3</sub>N<sub>4</sub> is still limited due to its low surface area and to absorb adequate visible light and high recombination rate of electron-hole pairs.<sup>[27,28]</sup> Recently, several experiments have been made to develop the photocatalytic activity of g-C<sub>3</sub>N<sub>4</sub> by different modifications, such as loading a co-catalyst onto the surface of g-C<sub>3</sub>N<sub>4</sub>, designing appropriate textural properties, doping and making composites with other semiconductor materials.<sup>[29-31]</sup>

In the present study, we demonstrate a facile hydrothermal method to synthesize porous TSCN with enhanced photocatalytic activity. When the TSCN sample was subjected to sun-light-irradiation, electrons are excited to form the VB to the CB with simultaneous generation of holes in the VB. Due to the variance of band gaps, electrons on  $\text{g-C}_3\text{N}_4$  CB can easily migrate to the CB of TS; on the other hand, holes on TS VB can also be transferred into  $\text{g-C}_3\text{N}_4$  VB, which effectively inhibited recombination and sustained the Lifetime of photogenerated electrons and holes, improved the photocatalysis process. The photocatalysts were characterized by powder X-ray diffraction, field emission scanning electron microscopy, Transmission electron microscopy, Thermogravimetry, nitrogen adsorption-desorption isotherm, Fourier transform infrared spectroscopy, UV-Visible diffused reflectance spectroscopy, photoluminescence spectroscopy. The degradation of RhB was employed to examine the photocatalytic activities of TSCN photo-catalysts under sunlight irradiation.

## 2.2 Experimental

Cetyltrimethyl ammonium bromide (CTAB, 98 %, SD fine), Ammonia solution (25 %, SD fine), Melamine (97.5 %, SD fine), Tetraethyl orthosilicate (TEOS, 98 %, Sigma-Aldrich), Titanium tetraisopropoxide (97 %, Sigma-Aldrich), Methanol (99 %, Merck), Rhodamine B (95 %, Sigma-Aldrich) were used as prepared and double distilled water was used throughout the experiment.

### 2.2.1 Preparation of porous Titanosilicate

In a typical procedure, an aqueous solution of CTAB and  $\text{NH}_3$  was stirred for 1 h at room temperature until the mixture becomes homogeneous. Calculated amount of tetraethyl orthosilicate (TEOS) was added dropwise into this mixture under vigorous stirring, followed by the addition of a predetermined amount of titanium tetraisopropoxide (TTIP) and was stirred for 6 h. The final molar gel composition is CTAB: 3.32TTIP: 6.14TEOS: 28.55 $\text{NH}_3$ : 24.75 $\text{H}_2\text{O}$ . The suspension was transferred into a 100 mL Teflon lined stainless steel autoclave and heated at 100 °C for 12 h. The product was collected by centrifugation, washed several times with deionized water and absolute methanol and dried at 80 °C for overnight. The resulting powder was calcined at 550 °C for 6 h in a programmable tubular furnace in the presence of air.

### 2.2.2 Preparation of g-C<sub>3</sub>N<sub>4</sub>

Bulk g-C<sub>3</sub>N<sub>4</sub> was synthesized according to the reported procedure.<sup>[32]</sup> In brief, melamine powder was directly heated in an alumina crucible, at a heating rate of 4.5 °C min<sup>-1</sup> to reach a temperature of 550 °C for 2 h under an N<sub>2</sub> atmosphere. The obtained pale yellow colored g-C<sub>3</sub>N<sub>4</sub> nanosheets are denoted as CN.

### 2.2.3 Preparation of mesoporous titanosilicate/g-C<sub>3</sub>N<sub>4</sub> hybrid nanocomposite

The TSCN composite was prepared by solution mixing followed by sonication. This method is simple and costs effective with rapid synthesis related to the in-situ method. In this method, an appropriate amount of g-C<sub>3</sub>N<sub>4</sub> was suspended in 100 mL of methanol and ultrasonicated for 1h, followed by constant stirring. 100 mg of Titanosilicate rods was suspended in 100 ml of methanol and then the solution was ultrasonicated for 30 min. The prepared TS solution was mixed with the g-C<sub>3</sub>N<sub>4</sub> solution and stirred for 2h. After stirring, the solution was filtered and washed several times with water and ethanol. The solid product was dried overnight in a vacuum oven at 80 °C to obtain the TSCN nanocomposite. The TSCN with 5wt % loaded g-C<sub>3</sub>N<sub>4</sub>, 10wt % loaded g-C<sub>3</sub>N<sub>4</sub> and 20wt % loaded g-C<sub>3</sub>N<sub>4</sub> are denoted as TSCN5, TSCN10 and TSCN20 respectively. The synthesized samples were subjected to various physicochemical characterizations.

### 2.2.4 Photocatalytic activity

Photocatalytic activity of the synthesized compounds were tested for RhB degradation under sunlight. The RhB solution was prepared in aqueous medium and the degradation experiments were carried out at NIT Warangal (18° 00' N, 79° 35' E) under similar conditions in the month of February, 2015 (having solar Direct Normal Irradiance ~243W/m<sup>2</sup> during the month). In a typical degradation study, 0.1 g of powder catalyst was added to RhB solution (5ppm, 100 mL) of appropriate pH-7 taken in a 250 mL beaker. Then, the RhB-catalyst suspensions were magnetically stirred at 250 rpm for 30 min in the dark to confirm adsorption-desorption equilibrium between the catalyst and RhB. After this, the beaker containing RhB-catalyst suspension was exposed to the direct sun light irradiation. To measure the RhB concentration during the degradation experiments, 4mL of suspension were sampled at regular time intervals, centrifuged at 6000 rpm to remove the catalyst and absorption measurements were carried out with the filtrates using a Shimadzu 2450 UV-visible spectrophotometer. The error due to loss of RhB and catalysts are minimized through maintaining the constant volume of RhB solution by keeping the

RhB solution back to the beaker after recording the absorbance at each time interval. A blank test was also performed with the RhB solution of same concentration without the catalyst under sunlight irradiation for self-degradation correction and to calculate RhB degradation efficiency. The photocatalytic RhB degradation efficiency of the catalysts was calculated using the following expression.

$$\text{RhB degradation efficiency (\%)} = (1 - C/C_0) \times 100$$

where  $C_0$  is the initial RhB concentration and  $C$  is the concentration of the RhB at different time intervals.

### 2.2.5 Scavenger Study

To recognize the role of various reactive species ( $\text{h}^+$ ,  $\cdot\text{OH}$  and  $\text{O}_2^{\cdot-}$ ) in photocatalytic RhB degradation, different scavengers were added to the RhB solution prior to the addition of the catalyst.<sup>[33]</sup> In a brief experimental procedure for the active species determination was similar to that described above during photodegradation studies. In detail, Ammonium oxalate (AO),  $\text{N}_2$  purging, and tertiary butyl alcohol (t-BuOH) were used as  $\text{h}^+$ ,  $\text{O}_2^{\cdot-}$ , and  $\cdot\text{OH}$  scavengers, respectively. Furthermore, the formation of hydroxyl radicals ( $\cdot\text{OH}$ ) on the surface of sunlight irradiated photo-catalyst was detected by the photoluminescence (PL) technique using terephthalic acid (TA) as a probe molecule. In a brief procedure, 0.1 g of a TSCN10 sample was dispersed in 100 mL of a mixture of a  $5 \times 10^{-4}$  mol  $\text{L}^{-1}$  aqueous TA solution and a  $2 \times 10^{-3}$  mol  $\text{L}^{-1}$  NaOH solution at room temperature. The above suspension was subjected to the photocatalytic activity evaluation of the catalyst under visible light irradiation and the PL intensity was measured using a fluorescence spectrophotometer with an excitation wavelength of 365nm.

## 2.3 Results and Discussion

The wide angle powder X-ray diffraction patterns of the pure mesoporous titanosilicate, pure  $\text{g-C}_3\text{N}_4$  and TSCN composites are shown in figure 2.1. The result shows that a broad peak centred at  $23^\circ$  was ascribed to the amorphous titaniumsilica matrix of pure mesoporosity are retained for the TSCN nanocomposites. The low angle PXRD of the pure mesoporous titanosilicate in the inset of figure 2.1 shows a strong feature at a low angle ((1 0 0) reflection line) and two other weaker peaks at higher angles ((1 1 0) and (2 0 0) reflections). This confirms that all samples were hexagonal mesoporous materials.<sup>[34,35]</sup> The crystalline  $\text{g-C}_3\text{N}_4$  shows a peak at  $2\theta=27.7^\circ$  corresponding to the

characteristic inter planar stacking reflection (002) of conjugated aromatic systems.<sup>[36]</sup> There are crystalline g-C<sub>3</sub>N<sub>4</sub> peaks in the TSCN hybrid composite materials, the peak intensities are increased with the increase in g-C<sub>3</sub>N<sub>4</sub> loading indicating the crystallinity of the synthesized TSCN composites.

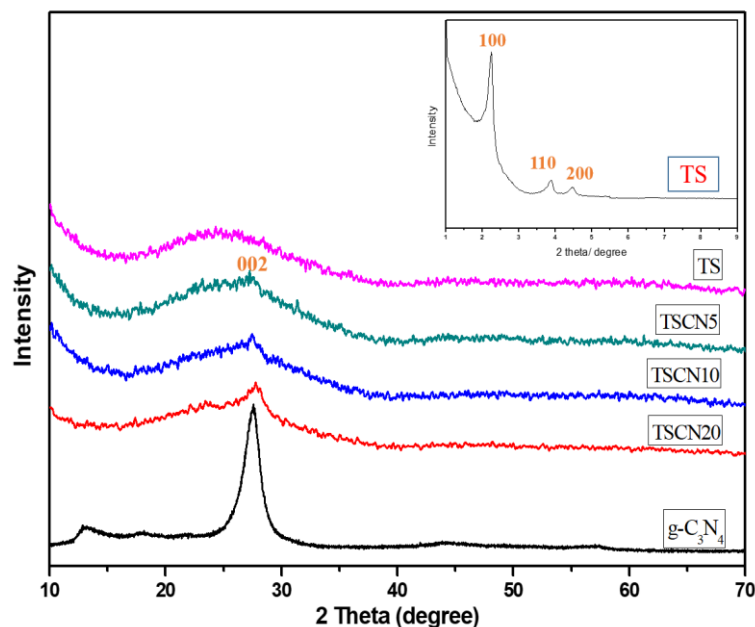


**Figure 2.1:** PXRD Spectra of TS, CN and TSCN composites (Inset: Low angle PXRD of TS)

The morphological growth of various samples was studied by FE-SEM (figure 2.2a-f). From figure 2.2a & 2.2b large numbers of the irregular cylindrical tube-like particles with the size of 200–500 nm are clearly seen in the pure TS samples. As shown in figure 2.2c, the pure g-C<sub>3</sub>N<sub>4</sub> sample consists of submicrometer sheets. Both two types of materials are found in the nanocomposites in figure 2.2d-f, which correspond to TS and CN, respectively. Furthermore, we find that the TS particles deposited on the surface of g-C<sub>3</sub>N<sub>4</sub> and were well dispersed. Table 2.1 shows elemental ratios as obtained from EDS analyses of TSCN10, were in excellent agreement with the input compositions.

The morphological growth of various samples was studied by TEM and HR-TEM (figure 2.3a-f). From figure 2.3a & 2.3b hexagonal mesoporous morphology of the pure titanosilicate and as shown in figure 2.3c g-C<sub>3</sub>N<sub>4</sub> sheet with soft edges after exfoliation. From figure 2.3(d-f) clearly indicates the distribution of porous titanosilicate over g-C<sub>3</sub>N<sub>4</sub> sheets and development of a heterojunction between the inorganic TS and organic g-C<sub>3</sub>N<sub>4</sub>

hybrid composite. This may facilitate the efficient electron transfer for photocatalytic application.

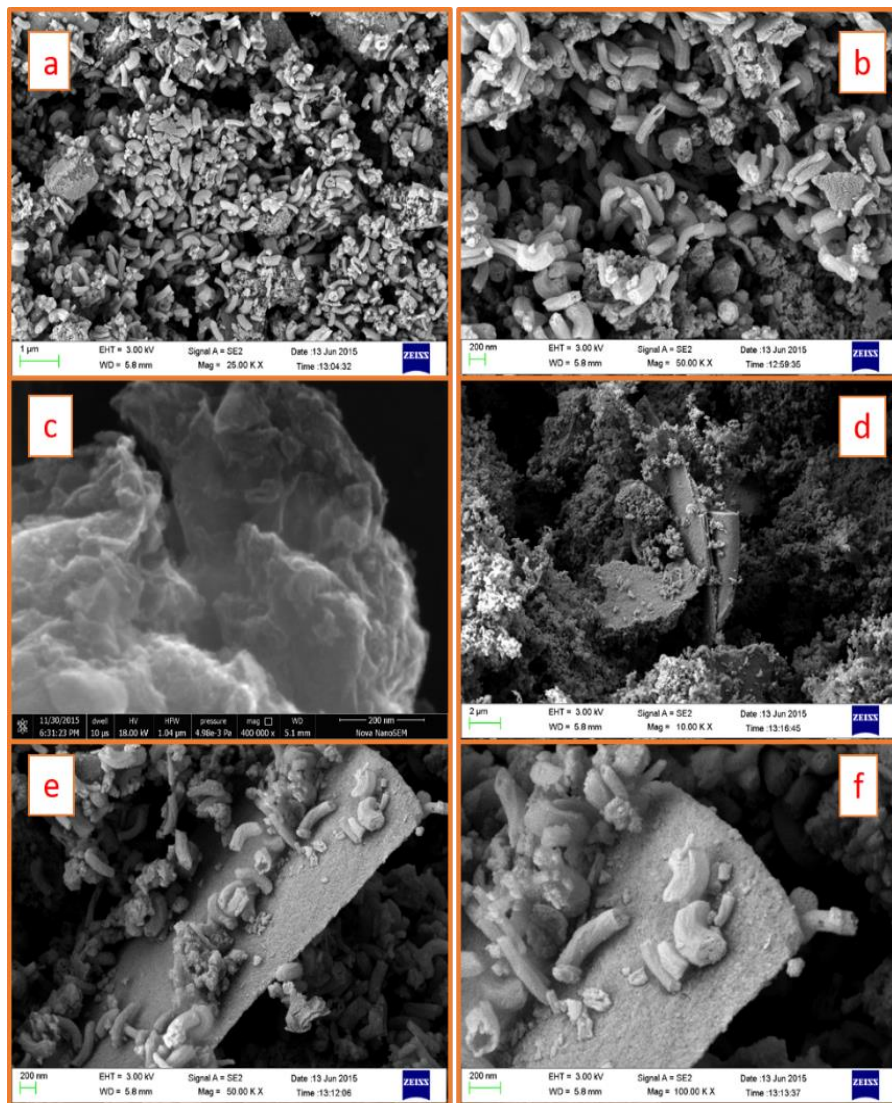


**Figure 2.2:** FE-SEM Images of a&b) TS, c) CN, d) TSCN10 and e&f) TSCN10 (magnified)

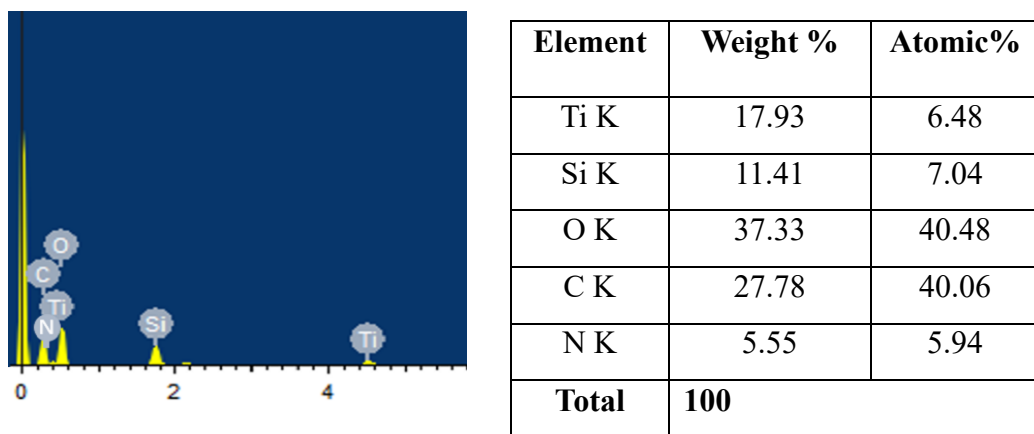


**Table 2.1:** FESEM EDX elemental composition of the TSCN10

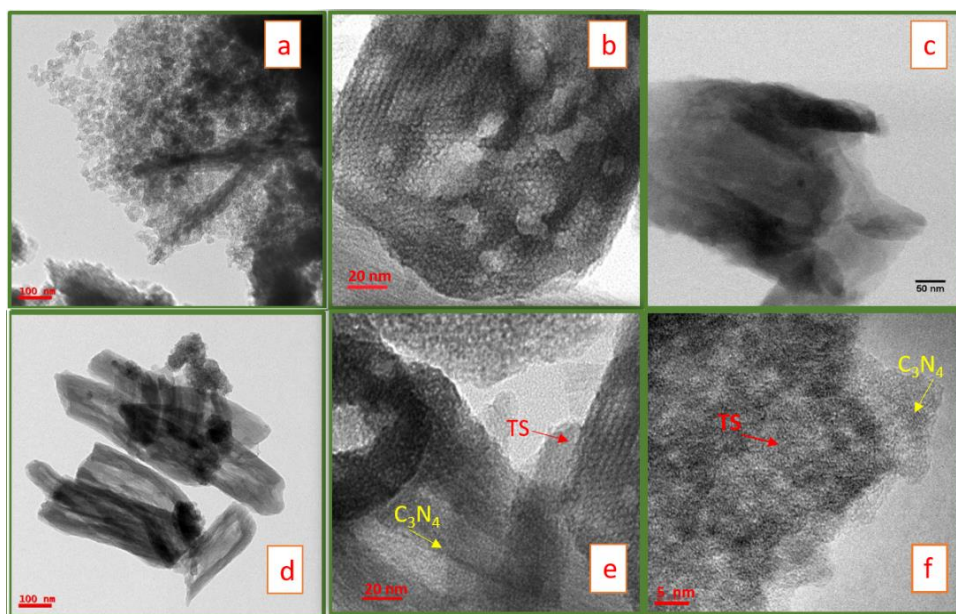


**Figure 2.3:** TEM images of the prepared Titanosilicate/g-C<sub>3</sub>N<sub>4</sub> photo-catalysts: (a) pure TS, (b) magnified pure TS, (c) g- C<sub>3</sub>N<sub>4</sub>, (d) TSCN10, (e) magnified TSCN10 and (d) HR-TEM image of TSCN10

The thermogravimetric analysis was carried out for the g-C<sub>3</sub>N<sub>4</sub> and mesoporous titanosilicate/g-C<sub>3</sub>N<sub>4</sub> nanocomposites. The amount of loaded g-C<sub>3</sub>N<sub>4</sub> was confirmed by TG analysis. For pure g-C<sub>3</sub>N<sub>4</sub>, a weight loss occurring from 550 °C to 700 °C could be attributed to the burning of g-C<sub>3</sub>N<sub>4</sub>. This weight loss region could be seen in all TSCN hybrid composites. The amount of g-C<sub>3</sub>N<sub>4</sub> in the hybrid composite was calculated from the corresponding weight loss and is shown in figure 2.4. The g-C<sub>3</sub>N<sub>4</sub> in the loaded compositions of TSCN nanocomposites was found to be 6wt%, 12wt% and 22wt%

respectively. Therefore, the amount of g-C<sub>3</sub>N<sub>4</sub> was nearly consistent with the dosage of g-C<sub>3</sub>N<sub>4</sub> loaded.

The nitrogen adsorption-desorption isotherm analysis was performed to investigate the Brunauer–Emmett–Teller (BET) specific surface area of the synthesized pure TS, pure g-C<sub>3</sub>N<sub>4</sub> and 10wt% Titanosilicate/g-C<sub>3</sub>N<sub>4</sub> nanocomposite. As shown in figure 2.5, a typical reversible type-IV adsorption isotherm of TS and TSCN composites except for CN.<sup>[37]</sup> The specific surface area of TSCN10 was found to be 481.78 m<sup>2</sup> g<sup>-1</sup>, which is slightly higher than the pure TS (446.36 m<sup>2</sup> g<sup>-1</sup>) but much higher than that of CN (35.75 m<sup>2</sup> g<sup>-1</sup>). The pore-size distribution analysis of the samples was also estimated using the Barrett-Joyner–Halenda (BJH) method, and results are shown in the inset of figure 2.5. The pore distribution curves of both TS and TSCN10 samples show narrow and uniform pores with a pore size of 3.0 and 3.4 nm respectively given in table 2.1, which is well consistent with the TEM observation. The large specific surface area and porous structure of TSCN heterojunctions are useful for the better adsorption of organic compounds and also provide a greater number of reactive sites for the photocatalytic process, thereby enhancing the photocatalytic activity.<sup>[38]</sup> Mesoporous materials are of different type like MCM-41, SBA-15, KIT-6, TUD-1 etc. with variation in surface area and stability. Normally their surface area is considerably reduced by incorporation of hetero transition metal ions due to partial amorphization. The materials we have used are resemble MCM-41. As expected their surface area is considerably reduced was reported by T.-D. Nguyen-Phanet. al.<sup>[24]</sup>

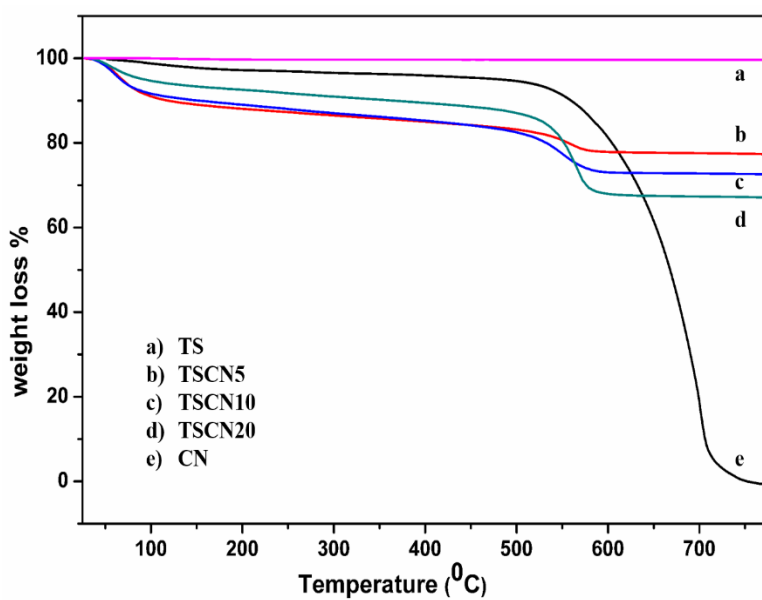


**Figure 2.4:** TGA curves of the synthesized of CN and TSCN photocatalysts

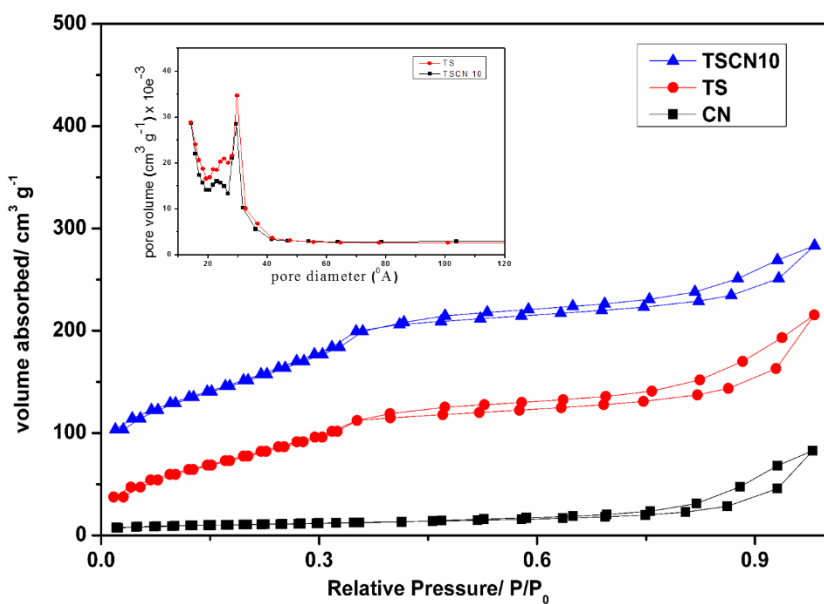


**Figure 2.5:**  $N_2$  adsorption-desorption isotherms of TS, CN and TSCN10 composite and pore size distribution curves (inset)

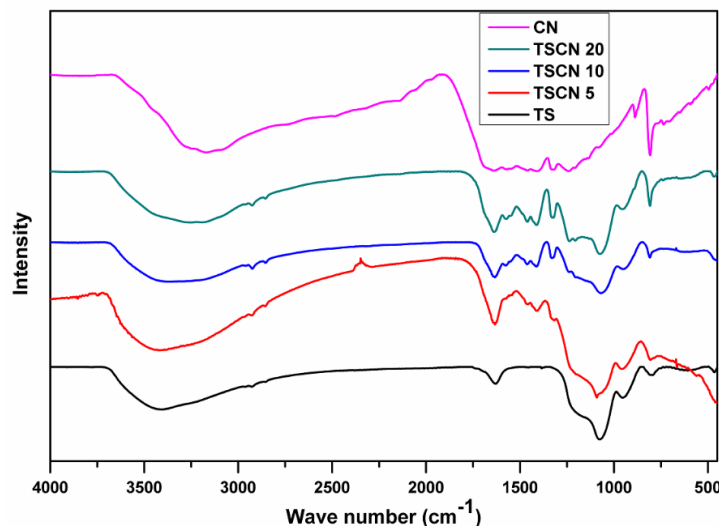


**Figure 2.6:** FTIR Spectra of TS, CN and TSCN nanocomposites

Figure 2.6 shows the FT-IR spectra of the calcined samples of pure titanosilicate, pure g-C<sub>3</sub>N<sub>4</sub>, and TSCN composites. The strong peaks near 1100, 802 and 467 cm<sup>-1</sup> agree to the Si-O-Si bond which implies the condensation of silicon alkoxide. It is observed that the Ti in TS is observed at wavenumber 960 cm<sup>-1</sup>.<sup>[39]</sup> In the FT-IR spectrum of g-C<sub>3</sub>N<sub>4</sub>, the broad bands around 3100 cm<sup>-1</sup> show the presence of N-H stretching vibrations. The peak at 1643 cm<sup>-1</sup> is due to stretching vibrations, while the bands at 1420, 1318 and 1240 cm<sup>-1</sup>

are associated with aromatic C–N stretching vibrations. The sharp characteristic peak at  $808\text{ cm}^{-1}$  corresponds to the s-triazine ring system.<sup>[40–42]</sup> All TSCN samples show the characteristic of pure titanosilicate and  $\text{C}_3\text{N}_4$ .

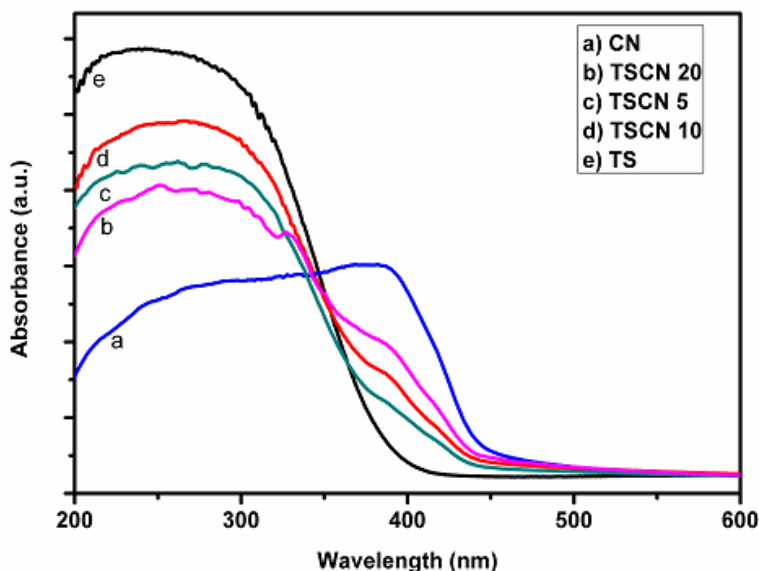


**Figure 2.7:** UV-Vis diffused reflectance Spectra of TS, CN and TSCN composites

The UV-vis DRS was performed to explain the light harvesting ability of the synthesized samples before and after the formation of the heterojunction. UV-Vis diffuse reflectance spectra of the synthesized pure TS, and pure  $\text{g-C}_3\text{N}_4$  and TSCN nanocomposites are shown in figure 2.7. As expected, a fundamental absorption cut off the edge at 390 nm for TS appeared, corresponding to a band gap of 3.1 eV, whereas  $\text{g-C}_3\text{N}_4$  has an absorption cut off the edge at 454 nm, corresponding to a band gap of 2.73 eV. The valence band edge potential and the conduction band edge potential of a semiconductor material can be determined by using the following equation.<sup>[43]</sup>

$$\text{E}_{\text{VB}} = X - E_{\text{e}} + 0.5E_{\text{g}} \quad (1)$$

$$\text{E}_{\text{CB}} = \text{E}_{\text{VB}} - E_{\text{g}} \quad (2)$$

where  $\text{E}_{\text{VB}}$  is the valence band edge potential,  $X$  is the absolute electronegativity of the semiconductor, which is determined as the geometric mean of the electronegativity of the constituent atoms,  $E_{\text{e}}$  is the energy of free electrons on the hydrogen scale (4.5 eV) and  $E_{\text{g}}$  is the band gap energy of the semiconductor. The  $\text{E}_{\text{CB}}$  of TS and  $\text{g-C}_3\text{N}_4$  are calculated

and found to be +0.03 eV and -1.22 eV, respectively. The EVB of TS and g-C<sub>3</sub>N<sub>4</sub> are estimated to be 3.13 and 1.51 eV, respectively.

### 2.3.1 Photoluminescence analysis

Figure 2.8 shows the Photoluminescence spectra of the synthesized pure g-C<sub>3</sub>N<sub>4</sub>, TSCN5, TSCN10 and TSCN20 recorded at room temperature with an excitation wavelength of 365 nm. A lower PL intensity for TSCN10 clearly indicates a larger concentration and lifetime of electron-hole pairs. The PL data support the results of RhB degradation experiment showing enhanced activity over TSCN10. It is broadly established that improvement of the photocatalytic activity of a photo-catalyst is ascribed to efficient photogenerated electron-hole pair separation. The lifetime and recombination rate of photogenerated electron holes in the semiconductor catalysts could be corroborated by PL analysis.

### 2.3.2 photocatalytic activity

The photocatalytic activity of the synthesized titanosilicate, g-C<sub>3</sub>N<sub>4</sub> and TSCN nanocomposites for the degradation of RhB under visible-light irradiation was evaluated (figure 2.9). As seen in figure 2.9a, the decrease in the concentration of RhB is faster with TSCN nanocomposites than with pure CN or TS under the similar experimental conditions. In absence of the catalyst, degradation of RhB was negligible under visible-light irradiation indicating the high stability of RhB under visible-light irradiation. To absorb RhB on the catalyst, the suspension was stirred for 30 min in the dark to achieve equilibrium before photodegradation. TSCN nanocomposites were exhibited a much higher RhB adsorption capacity than pure CN. The results show that the presence of the catalyst and sunlight is essential for RhB degradation. Figure 2.9b shows that the plots of  $-\ln(C/C_0)$  versus irradiation time were linear, which indicates that the kinetics of photodegradation of the RhB was pseudo first-order. The optimum photocatalytic activity of TSCN10 under visible-light irradiation is almost 5 times higher than that of pure g-C<sub>3</sub>N<sub>4</sub>.

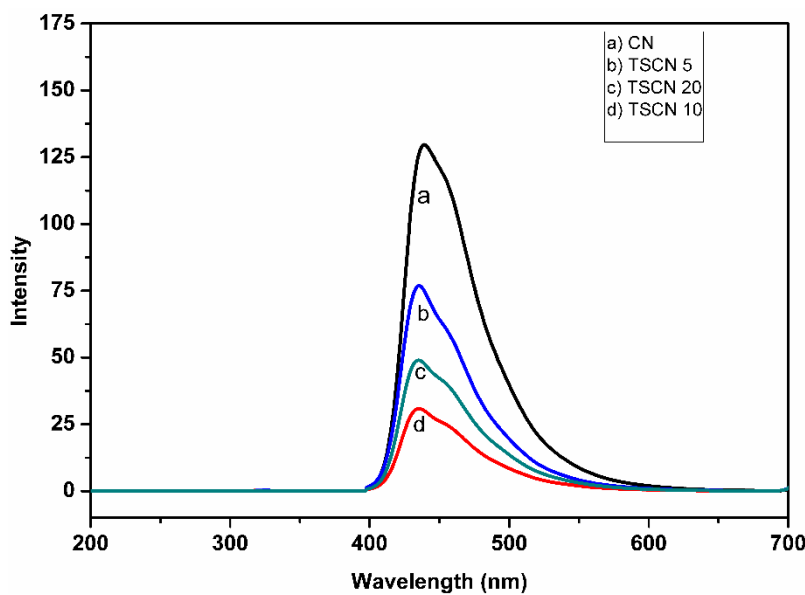


**Figure 2.8:** Photoluminescence Spectra of pure CN and TSCN composites excited at 365nm

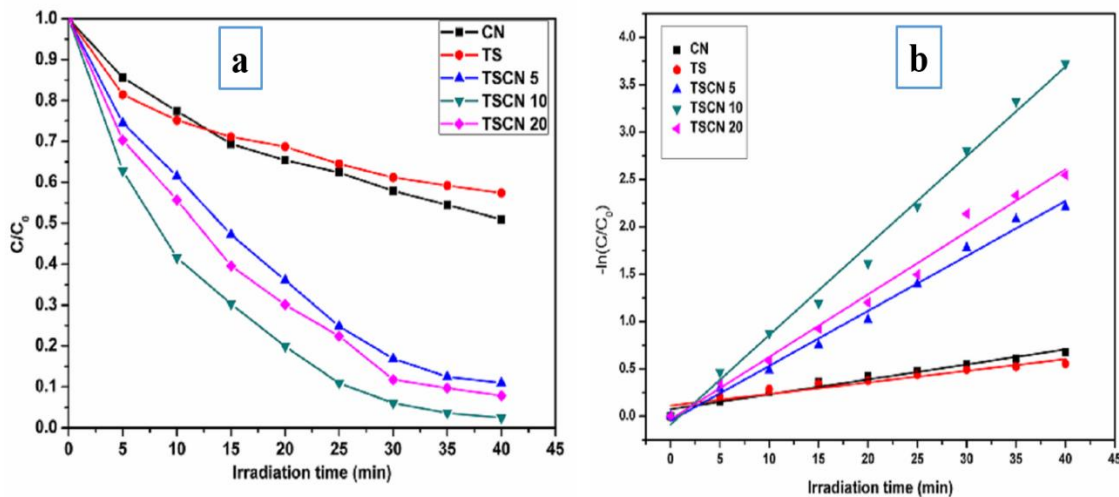


**Figure 2.9:** (a) Comparison of the photocatalytic activities of TS, CN and TSCN nanocomposites for the degradation of RhB in aqueous solution under sunlight irradiation and (b) the corresponding first-order kinetics plots of TS, CN and TSCN composites

### 2.3.3 Reaction Mechanism

#### 2.3.3.1 Reactive species

Generally, photogenerated reactive species, such as,  $\cdot\text{OH}$ ,  $\text{O}_2^{\cdot-}$ , and  $\text{h}^+$  are expected to take part in the photocatalytic RhB degradation process. To understand the mechanism and detect the main reactive species responsible for RhB degradation in the presence of

TSCN10, scavenger tests were carried out employing  $N_2$  purging, ammonium oxalate (AO), and tertbutanol (t-BuOH). Figure 2.10a, shows that after  $N_2$  purging, which acts as an  $O_2^\cdot$  radicals scavenger, This means that dissolved  $O_2$  is a key factor in RhB photodegradation in the case of the TSCN10 photo-catalyst, affecting the formation of  $O_2^\cdot$  through direct reduction of  $O_2$  and the formation of  $\cdot OH$  through multistep reduction of  $O_2$ .<sup>[44]</sup> On addition of AO, the rate of photocatalytic degradation of RhB is extremely reduced compared with no scavenger under the same conditions. In accumulation, an important change in the degradation of RhB is observed after the addition of TBA, which shows that photogenerated  $O_2^\cdot$ ,  $\cdot OH$  and  $h^+$  plays a significant role in the degradation of RhB.

### 2.3.3.2 Hydroxyl radical generation

The  $\cdot OH$  radical generation during the photocatalytic reaction can be easily detected by a photoluminescence (PL) technique using terephthalic acid (TA) a probe molecule, which readily reacts with  $\cdot OH$ . The maximum intensity peaks in the PL spectra were observed at approximately 435 nm as shown in figure 2.10b, with an excitation wavelength of 365 nm. The PL intensity increases gradually with increasing irradiation time, which reveals that  $\cdot OH$  is generated on the sunlight irradiated surface of TSCN. From these results, the  $\cdot OH$  radicals initiate from the reaction of photogenerated electrons during the reduction of dissolved  $O_2$ .

### 2.3.4 Proposed photocatalytic mechanism

In order to understand the photocatalytic mechanism for the synthesized TSCN heterojunctions in detail, the band edge positions of the conduction band (CB) and valence band (VB) of titanosilicate and g-C<sub>3</sub>N<sub>4</sub> should be determined since they are strongly related to the photocatalytic oxidation process of organic compounds. The ECB of TS and g-C<sub>3</sub>N<sub>4</sub> are calculated and found to be +0.03 eV and -1.22 eV, respectively. The EVB of TS and g-C<sub>3</sub>N<sub>4</sub> are estimated to be 3.13 and 1.51 eV, respectively. On the basis of UV DRS, reactive species trapping experiments, and calculated energy bands, a possible photocatalytic mechanism of porous TSCN heterojunction structure is drawn as shown in figure 2.11. Under sunlight irradiation, both titanosilicate and g-C<sub>3</sub>N<sub>4</sub> absorb photons of energy greater than the corresponding band gap energy, which excite the electrons in the valence band (VB) to the conduction band (CB) and leave holes in the VB. The excited electrons in the CB of the g-C<sub>3</sub>N<sub>4</sub> nanosheets can be easily transferred to the CB of the

titanosilicate, resulting in accumulation of negative charges in titanosilicate close to the heterojunction. At the same time, the hole which was present in the VB of titanosilicate would transfer to the VB of  $\text{g-C}_3\text{N}_4$  as the band edges of both titanosilicate and  $\text{g-C}_3\text{N}_4$  lie in the visible region. The migration of photo-induced charge carriers can be promoted by the inner electric field established at the heterojunction interface. Therefore, the photogenerated electron-hole pairs will be efficiently separated with the formation of a heterojunction between the  $\text{g-C}_3\text{N}_4$  and titanosilicate interface, resulting in the enhanced photocatalytic activity of the TSCN photo-catalysts.

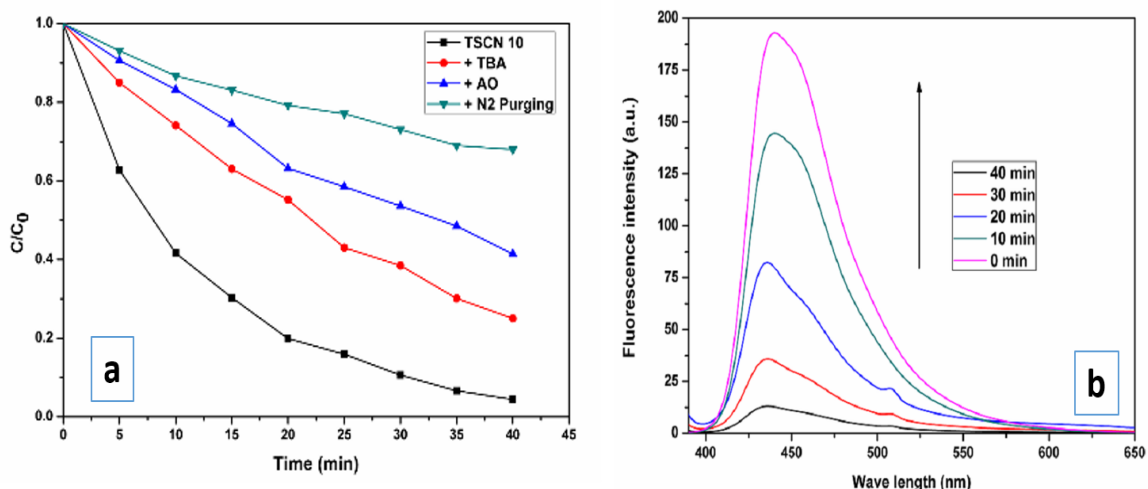


**Figure 2.10:** (a) Effects of different scavengers on the degradation of RhB under sunlight irradiation in the presence of the TSCN 10 photo-catalyst and (b) •OH trapping PL spectra of TSCN10 in TA solution under sunlight irradiation

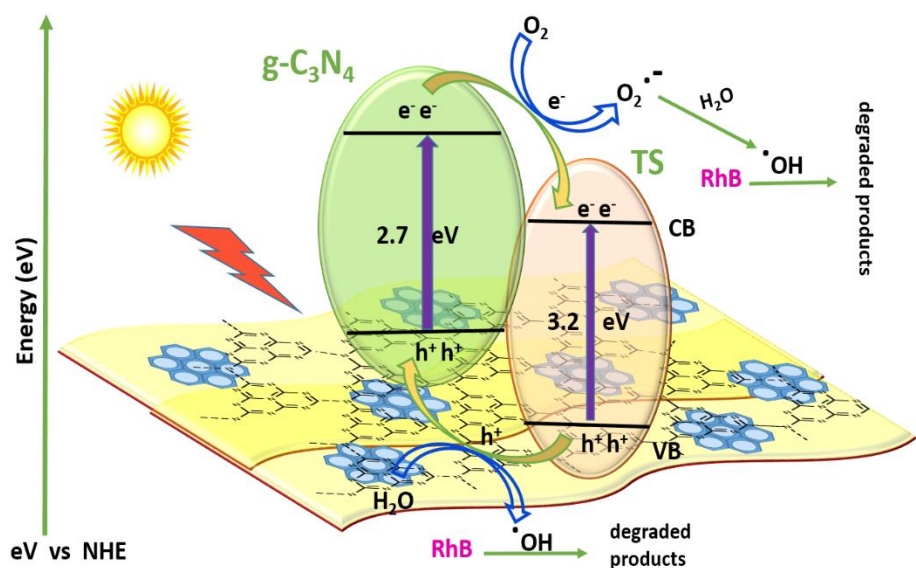


**Figure 2.11:** Schematic diagram showing the process of the photocatalytic RhB degradation over the TSCN composite

### 2.3.5 Reusability

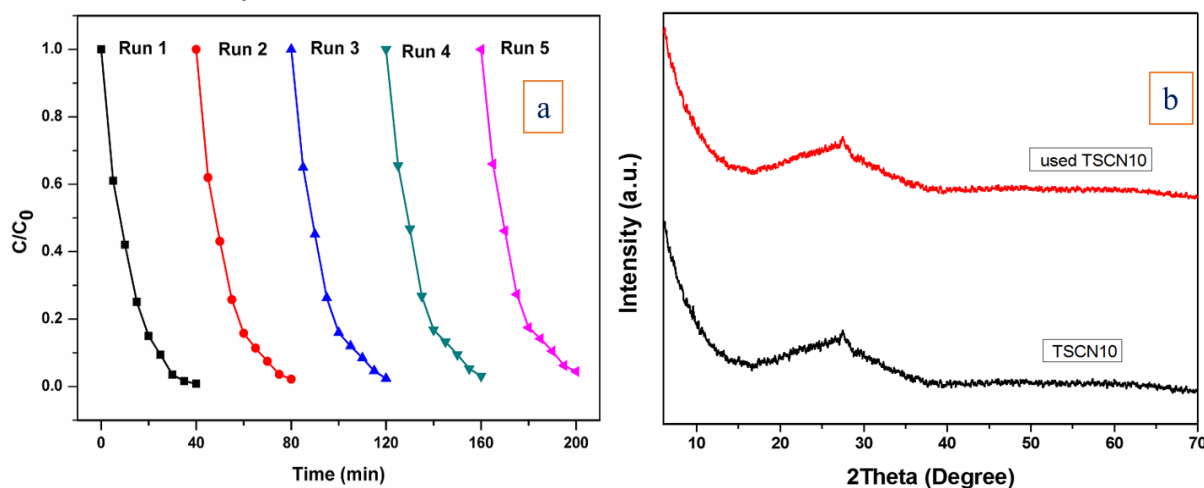


**Figure 2.12:** a) Reusability of the TSCN10 photo-catalyst for the photocatalytic degradation of RhB during five successive experimental runs in aqueous solution under sunlight irradiation. b) PXRD pattern of the pure TSCN10, Used TSCN10

The photo-catalyst reusability is an important issue for their experimental use. For this to resolve, the photocatalytic degradation of RhB over TSCN10 was carried out for five successive cycles (figure 2.12a). It has been observed that 95% degradation efficiency of the catalysts was retained even after five consecutive experimental runs in 40 min of solar irradiation, demonstrating no noticeable loss in the activity of the catalyst. The PXRD studies were performed for TSCN after five successive experimental runs (figure 2.12b). This experiment can run in normal laboratory settings using Xe- lamp (500W or 450W or 300W). The photocatalytic activity of TSCN for RhB degradation under visible light irradiation is very low compared with sunlight irradiation. From the literature, S. Tonda et. al. has been reported Fe doped  $\text{g-C}_3\text{N}_4$  exhibited enhanced photocatalytic activity for the degradation of RhB within 30 min under sun light irradiation.<sup>[45a]</sup> T. S. Natarajan et. al. has been Bi-doped  $\text{TiO}_2$  nanotubes shows improved photodegradation of RhB within 3hrs under sun light.<sup>[45b]</sup> Porous  $\text{Fe}_3\text{O}_4/\text{g-C}_3\text{N}_4$  exhibited enhanced photocatalytic activity for the degradation of methyl orange within 150 min under visible light irradiation was reported by X. Zhou et.al..<sup>[45c]</sup>

## 2.4 References

- [1] P. V. Kamat, *Phys. Chem.* **2007**, 392, 2834–2860.
- [2] M. R. Hoffmann, S. T. Martin, W. Choi, D. W. Bahnemann, *Chem. Rev.* **1995**, 95,

69–96.

- [3] H. Tong, S. Ouyang, Y. Bi, N. Umezawa, M. Oshikiri, J. Ye, *Adv. Mater.* **2012**, *24*, 229–251.
- [4] H. Zhou, Y. Qu, T. Zeid, X. Duan, *Energy Environ. Sci.* **2012**, *5*, 6732.
- [5] F. Fresno, R. Portela, S. Suárez, J. M. Coronado, *J. Mater. Chem. A* **2014**, *2*, 2863–2884.
- [6] J. H. Pan, H. Dou, Z. Xiong, C. Xu, J. Ma, X. S. Zhao, *J. Mater. Chem.* **2010**, *20*, 4512.
- [7] T. Hisatomi, J. Kubota, K. Domen, *Chem. Soc. Rev.* **2014**, *43*, 7520–7535.
- [8] X. Chen, S. Shen, L. Guo, S. S. Mao, *Chem. Rev.* **2010**, *110*, 6503–70.
- [9] M. Yan, Y. Wu, Y. Yan, X. Yan, F. Zhu, Y. Hua, W. Shi, *ACS Sustain. Chem. Eng.* **2016**, *4*, 757–766.
- [10] F. Dong, Z. Wang, Y. Li, W. Ho, S. C. Lee, *Environ. Sci. Technol.* **2014**, *48*, 10345–10353.
- [11] Y. He, L. Zhang, B. Teng, M. Fan, *Environ. Sci. Technol.* **2015**, *49*, 649–656.
- [12] X. Lin, Y. Wang, J. Zheng, C. Liu, Y. Yang, G. Che, *Dalt. Trans.* **2015**, *44*, 19185–19193.
- [13] X. Wang, W. Yang, F. Li, Y. Xue, R. Liu, Y. Hao, *Ind. Eng. Chem. Res.* **2013**, *52*, 17140–17150.
- [14] C. Perego, R. Millini, *Chem. Soc. Rev.* **2013**, *42*, 3956–76.
- [15] G. P. and B. N. M. Taramasso, *United StateS Patent [19]*, **1983**.
- [16] M. Moliner, A. Corma, *Microporous Mesoporous Mater.* **2014**, *189*, 31–40.
- [17] S. Uma, S. Rodrigues, I. N. Martyanov, K. J. Klabunde, *Microporous Mesoporous Mater.* **2004**, *67*, 181–187.
- [18] F. X. Llabrés i Xamena, P. Calza, C. Lamberti, C. Prestipino, A. Damin, S. Bordiga, E. Pelizzetti, A. Zecchina, *J. Am. Chem. Soc.* **2003**, *125*, 2264–2271.
- [19] S. K. Das, M. K. Bhunia, A. Bhaumik, *J. Solid State Chem.* **2010**, *183*, 1326–1333.
- [20] S. Anandan, *Dye. Pigment.* **2008**, *76*, 535–541.
- [21] C. M. a Parlett, K. Wilson, A. F. Lee, *Chem. Soc. Rev.* **2013**, *42*, 3876–3893.
- [22] K.-M. Choi, T. Yokoi, T. Tatsumi, K. Kuroda, *J. Mater. Chem. A* **2013**, *1*, 2485.
- [23] M. Selvaraj, *Catal. Sci. Technol.* **2014**, *4*, 2674.
- [24] T.-D. Nguyen-Phan, E. W. Shin, V. H. Pham, H. Kweon, S. Kim, E. J. Kim, J. S. Chung, *J. Mater. Chem.* **2012**, *22*, 20504.

[25] Y. Zhang, W. Zhou, S. Liu, A. Navrotsky, *Chem. Mater.* **2011**, *23*, 1166–1173.

[26] E. Kroke, *Coord. Chem. Rev.* **2004**, *248*, 493–532.

[27] J. Hu, W. Cheng, S. Huang, D. Wu, Z. Xie, *Appl. Phys. Lett.* **2006**, *89*, 261117.

[28] A. Thomas, A. Fischer, F. Goettmann, M. Antonietti, J.-O. Müller, R. Schlögl, J. M. Carlsson, *J. Mater. Chem.* **2008**, *18*, 4893.

[29] W.-J. Ong, L.-L. Tan, Y. H. Ng, S.-T. Yong, S.-P. Chai, *Chem. Rev.* **2016**, *116*, 7159–7329.

[30] X. Lin, D. Xu, J. Zheng, M. Song, G. Che, Y. Wang, Y. Yang, C. Liu, L. Zhao, L. Chang, *J. Alloys Compd.* **2016**, *688*, 891–898.

[31] X. Lin, B. Wei, X. Zhang, M. Song, S. Yu, Z. Gao, H. Zhai, L. Zhao, G. Che, *Sep. Purif. Technol.* **2016**, *169*, 9–16.

[32] S. Kumar, T. Surendar, A. Baruah, V. Shanker, *J. Mater. Chem. A* **2013**, *1*, 5333.

[33] N. Zhang, S. Liu, X. Fu, Y. Xu, *J. Phys. Chem. C* **2011**, *115*, 9136–9145.

[34] F.-J. Chen, C.-W. Shao, M.-N. Zhao, Z.-S. Bu, Y. Zhang, X.-N. Dai, G.-W. Zhou, *Chinese Chem. Lett.* **2014**, *25*, 962–966.

[35] C. T. Kresge, M. E. Leonowicz, W. J. Roth, J. C. Vartuli, J. S. Beck, *Nature* **1992**, *359*, 710–712.

[36] S. Tonda, S. Kumar, S. Kandula, V. Shanker, *J. Mater. Chem. A* **2014**, *2*, 6772.

[37] H. M. Abdelaal, *Chinese Chem. Lett.* **2014**, *25*, 627–629.

[38] T. Surendar, S. Kumar, V. Shanker, *Phys. Chem. Chem. Phys.* **2014**, *16*, 728–735.

[39] J. Sudhakarreddy, *J. Catal.* **1991**, *130*, 440–446.

[40] X. Li, J. Zhang, L. Shen, Y. Ma, W. Lei, Q. Cui, G. Zou, *Appl. Phys. A* **2009**, *94*, 387–392.

[41] G. Zhang, J. Zhang, M. Zhang, X. Wang, *J. Mater. Chem.* **2012**, *22*, 8083.

[42] L. Liu, D. Ma, H. Zheng, X. Li, M. Cheng, X. Bao, *Microporous Mesoporous Mater.* **2008**, *110*, 216–222.

[43] Y. Li, J. Wang, H. Yao, L. Dang, Z. Li, *J. Mol. Catal. A Chem.* **2011**, *334*, 116–122.

[44] S. C. Yan, Z. S. Li, Z. G. Zou, *Langmuir* **2010**, *26*, 3894–3901.

[45] (a) S. Tonda, S. Kumar, S. Kandula and V. Shanker, *J. Mater. Chem. A*, **2014**, *2*, 6772. (b) T. S. Natarajan, K. Natarajan, H. C. Bajaj, R. J. Tayade, *J. Nanopart. Res.* **2013**, *15*, 1669. (c) X. Zhou, B. Jin, R. Chen, F. Peng and Y. Fang, *Mat. Res. Bull.* **2013**, *48*, 1447.



## CHAPTER III

Development of magnetically separable and recyclable porous Titanosilicate/Fe<sub>3</sub>O<sub>4</sub> hybrid nanocomposites for photocatalytic degradation of methylene blue under UV light irradiation



### 3 Development of magnetically separable and recyclable porous Titanosilicate/Fe<sub>3</sub>O<sub>4</sub> hybrid nanocomposites for photocatalytic degradation of methylene blue under UV light irradiation

#### 3.1 Introduction

In recent years, semiconductor-mediated heterogeneous photocatalysis is a promising technology for dye degradation experiments, hydrogen evolution from water splitting, conversion of CO<sub>2</sub> into methane, methanol and environmental remediation.<sup>[1-6]</sup> Semiconductor photocatalysis is hosted by electron-hole pairs and its band gap excitations. Photocatalysts absorbing light with energies equal to or greater than its bandgap, the electron travels from the valence band into the direction of the conduction band and leave of absence the holes in the valence band. By this feature holes joined in oxidative reactions takes place at valence band is termed as photo-oxidation and electrons joined reductive reactions take place at conduction band is termed as photo-reduction<sup>[7]</sup>. Continuous investigation has been dedicated to improving photocatalysts, designed to growth light absorbing efficiency and to decrease photoinduced charge transporters of electron-hole recombination then charge migrates to the surface of the photocatalyst<sup>[8,9]</sup>. A variation of semiconductor-based photocatalysts has been explored, as well as metal oxides (TiO<sub>2</sub>, ZnO), graphene based<sup>[10-13]</sup> composites and some hybrid composites (C<sub>3</sub>N<sub>4</sub>/ Fe<sub>3</sub>O<sub>4</sub>, C<sub>3</sub>N<sub>4</sub>/TiO<sub>2</sub>) etc.<sup>[14-18]</sup>.

Heterogeneous catalysts based on metal containing porous silicates have outstanding catalytic activity due to their exceptional physical topographies like remarkably high surface area, well-defined and uniform pore construction. The discovery of titanosilicate 1983, a huge number of articles regarding the synthesis titanosilicate and its derivatives have been synthesized.<sup>[19,20]</sup> For example, loading co-catalysts and transition metals doping onto the superficial of the titanosilicate with can be obviously promoted the efficiency of photocatalytic activity.<sup>[21-29]</sup> Also, more recently Thuy-Duong Nguyen-Phan et al. reported titanosilicate/reduced graphene-oxide photocatalyst with methylene blue dye degradation using UV light irradiation.<sup>[30]</sup>

On the other hand, iron oxide nanoparticles have involved much importance for their magnetic properties, their usages in drug transfer schemes, protein departure,

wastewater management and lithium storing capacity.<sup>[31-36]</sup> Heteronano-structured photocatalysts collected of magnetic components such as metal/Fe<sub>3</sub>O<sub>4</sub>, TiO<sub>2</sub>/Fe<sub>3</sub>O<sub>4</sub> and WO<sub>3</sub>/Fe<sub>3</sub>O<sub>4</sub> have revealed enhanced performance due to their special assets and possible applications that couldn't be succeeded only with the single-component catalyst<sup>[37-41]</sup>. These revisions designed to incorporate superparamagnetic Fe<sub>3</sub>O<sub>4</sub> nanoparticles and titanosilicate into a hybrid nanocomposite as a proficient photocatalyst for the reason that Fe<sub>3</sub>O<sub>4</sub> conductivity is high.

In this work, we have demonstrated efficient photocatalytic activity of magnetically separable and recyclable nanostructured porous titanosilicate-Fe<sub>3</sub>O<sub>4</sub> hybrid nanocomposite. The synthesized nanocomposites were physically characterized by powder X-ray diffraction (PXRD), Transmission electron microscopy (TEM), Field emission scanning electron microscopy (FE-SEM), energy dispersive spectrometer (EDS), Nitrogen adsorption-desorption (BET), Fourier transform-Infrared spectroscopy (FT-IR) and UV-Visible diffuse reflectance spectroscopy (UV-Vis DRS). The morphological results were established that successful deposition of monodispersed Fe<sub>3</sub>O<sub>4</sub> nanoparticles onto the surface of titanosilicate matrix allows the diffusion of light by several paths. This enhances light harvesting capacity and therefore significantly improved photocatalytic activity was examined under UV-light irradiation. In addition, Fe<sub>3</sub>O<sub>4</sub> nanoparticles deposited onto the superficial of the photocatalysts showed by applying external magnetic field is an actual way to separated photocatalyst from the photocatalytic experiment. The recovered photocatalyst was allowed to be recycled in several series. This methodology prohibited the accumulation of the photocatalyst particles during regaining and it can grow the stability of the catalyst.

### 3.2 Experimental details

Ferrous chloride (99.0%), Tetraethyl orthosilicate (98.0%), Ferric chloride (99.9% metal-based), Titanium tetrabutoxide (97.0%), were purchased from Sigma–Aldrich. NH<sub>3</sub> solution (26%), Methylene blue, Cetyltrimethyl ammoniumbromide (CTAB, 98.0%), were purchased from SD fine chemicals and 4-chlorophenol (98%) were obtained from Sisco Res. Lab. Pvt. Ltd.. All additional chemicals were used no other extra refining. Millipore water was used for the preparation of aqueous solutions.

In a typical process, Step 1: an aq. solution of CTAB and ammonia solution were stirred for one hour at 302K until a homogeneous mixture is obtained. Step 2: An appropriate amount of tetraethyl orthosilicate was added drop by drop into a predetermined amount of titanium tetrabutoxide. Step 2 mixture is added to the Step 1 homogeneous solution and it was stirred for six hours. The suspension was shifted into an autoclave for hydrothermal process and heated at 373K for 12 h. After the centrifugation product was collected, washed with millipore water, methanol and dried at 353K. The resultant product was calcined at 823K for 6 h with a slow ramp rate processes in a programmable furnace in the presence of atmospheric air.

In a typical process (figure 3.1), an appropriate amount of titanosilicate was dispersed in 250 mL of methanol and ultrasonicated for four hours.  $\text{FeCl}_3 \cdot 6\text{H}_2\text{O}$  and  $\text{FeCl}_2 \cdot 4\text{H}_2\text{O}$  were added to the 20 mL of millipore water separately and then added to the titanosilicate. The mixture was allowed to stir at 343K for 40 min, and then 5 mL of  $\text{NH}_3$  was rapidly transferred into the mixture. The resultant reaction mixture was allowed to stir for 45 min at the same temperature, the mixture was cooled and washed with millipore water and methanol. The obtained product was dried in an oven at 353K for further evolution of physico-chemical properties. For comparison, pure  $\text{Fe}_3\text{O}_4$  was synthesized via the similar process without adding titanosilicate. The synthesized titanosilicate/ $\text{Fe}_3\text{O}_4$  photocatalysts with 5, 15 and 25wt% of  $\text{Fe}_3\text{O}_4$  were named as FTS5, FTS15 and FTS25 respectively. The pure titanosilicate named as TS and  $\text{Fe}_3\text{O}_4$  named as FO.

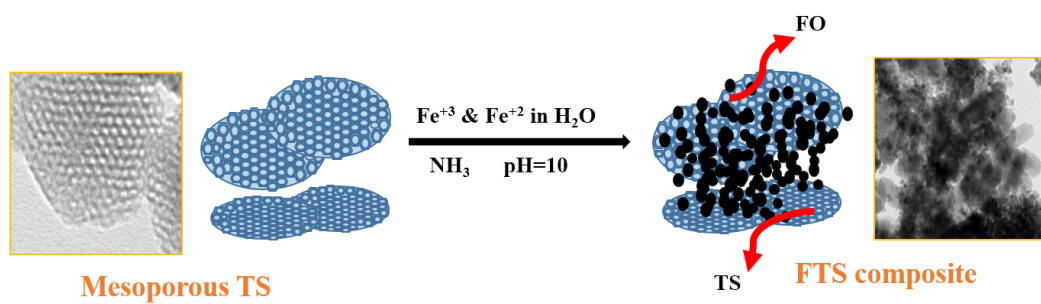


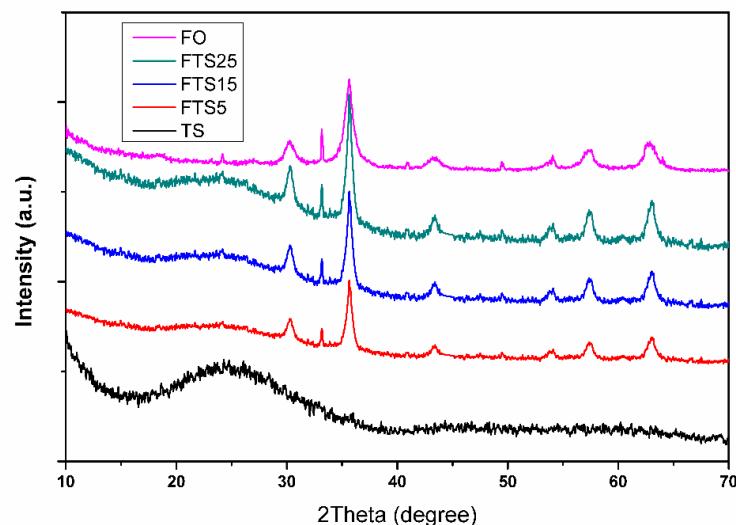
**Figure 3.1:** Schematic diagram of the FTS nanocomposite synthesis

Methylene blue (MB), a broadly used colored dye, was selected as an organic pollutant to examine the UV light photocatalytic experiment of the samples. The activity of the compounds was examined via degradation of MB organic pollutants under UV light irradiation. The UV light source was a photoreactor 400 W Hg lamp (Haber annular type

photo reactor). The photocatalyst (100 mg) was added to an aqueous solution of MB (100 mL, 10 mg L<sup>-1</sup>) in a beaker under UV light irradiation. Prior to irradiation, the solution was allowed to stir in the darkroom for 30 min to create an adsorption equilibrium. In order to carryout the photocatalytic experiments, samples were collected in the simultaneous time interval. The photocatalyst was separated from the solution by applying external magnetic field and used for the absorbance measurement. A blank test was also performed on an aqueous MB solutions of same concentration without photocatalyst under UV-light irradiation for self-degradation correction and also calculate dye degradation efficiency. The concentration of MB during the degradation process was monitored by using a UV-Visible spectrophotometer.

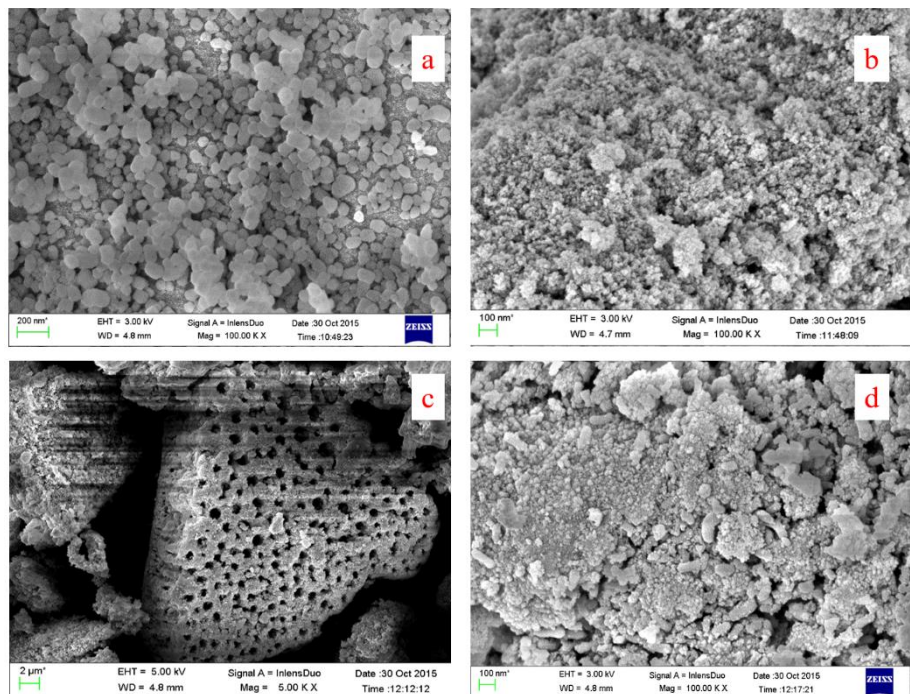
### 3.3 Results and Discussion

Figure 3.2 shows the wide angle PXRD spectra of pure TS, pure FO and FTS hybrid composites were used to elucidate the phase and structural parameters. The observed diffraction peaks of pure FO are in good agreement with those reported in the literature for pure face-centered-cubic Fe<sub>3</sub>O<sub>4</sub>.<sup>[32,42a]</sup> The broad peak at 2 $\Theta$  is 23° was indicated to the amorphous porous silica matrix of pure TS that was also present in a pattern of the FTS hybrid nanocomposites. It was also seen that FO crystal phase didn't change after hybridization with TS, but the diffraction peak positions for FO was found at a little lower angle compared to pure Fe<sub>3</sub>O<sub>4</sub>, suggesting a strong interaction between FO and TS. Furthermore, no other impurity peaks were found, representing the FTS is to be a two-phase composite.



**Figure 3.2:** a) Powder XRD of pure FO, Pure TS and FTS hybrid nanocomposites

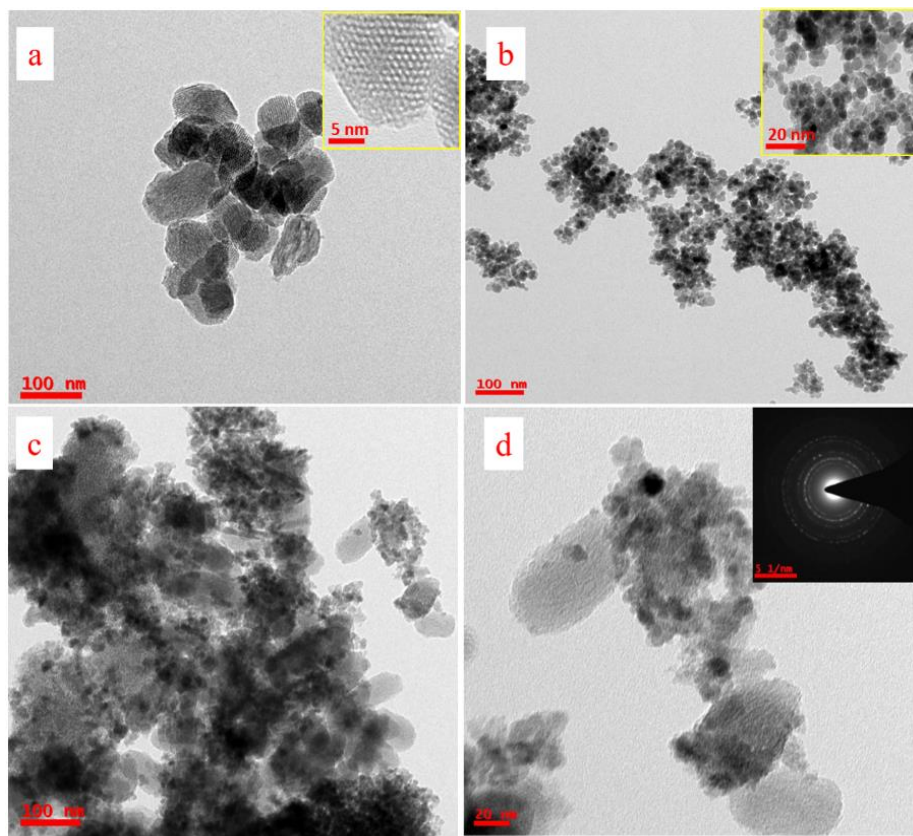
The smaller crystal always showed larger adsorption capacity and higher photocatalytic efficiency. This is attributed to the larger external surface areas of small crystalline was reported by J. Zhu et. al.<sup>[42b]</sup> When the particle size decreases surface area increases. The successful electron transfer was possible only when the particle size is small then photocatalytic efficiency is more was reported by M. Ni et.al..<sup>[42c]</sup>



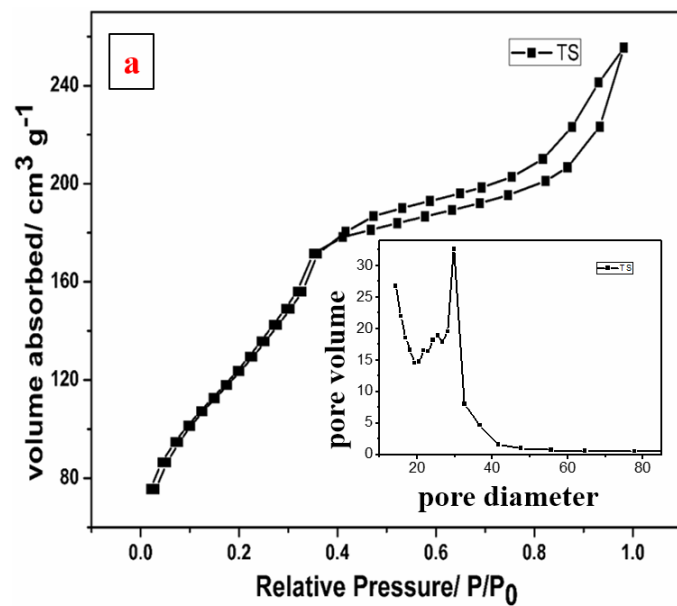
**Figure 3.3:** FE-SEM of (a) Pure TS, (b) pure FO and (c) FTS15 (d) magnified FTS15 hybrid nanocomposites

The morphology and nanostructures of the prepared samples were then investigated by FE-SEM and TEM. Figure 3.3(a-d) shows the FE-SEM images of Titanosilicate,  $\text{Fe}_3\text{O}_4$  nanoparticles and FTS15 hybrid nanocomposite. It can be seen that the  $\text{Fe}_3\text{O}_4$  possesses spherical shape morphology with high agglomeration. But, FESEM pictures have insufficient resolution for the investigation of heterostructure and particle size distributions. TEM images of figure 3.4a and inset is a well define the hexagonal porous structure of pure titanosilicate. Figure 3.4b and inset is a spherical structure of  $\text{Fe}_3\text{O}_4$  nanoparticles, the average particle size is 5-10 nm. The Titanosilicate/ $\text{Fe}_3\text{O}_4$  nanocomposite showed almost similar morphology (figure 3.4c) as compared with  $\text{Fe}_3\text{O}_4$  nanoparticles. HR-TEM studies were confirmed the interface in the middle of Titanosilicate and  $\text{Fe}_3\text{O}_4$  in the composite system (figure 3.4d). Moreover, the SAED pattern (Selected Area Electron Diffraction, inset of figure 3.4d) shows a full diffraction

ring which is indicated to the FTS representative planes. However, Titanosilicate/Fe<sub>3</sub>O<sub>4</sub> nanocomposites also show a certain degree of particle agglomeration.



**Figure 3.4:** TEM of a) Pure TS (inset is porosity of the TS), b) pure FO (inset is magnified FO), c) FTS15, d) magnified FTS15 (inset is SAED pattern of the FTS15) hybrid composite



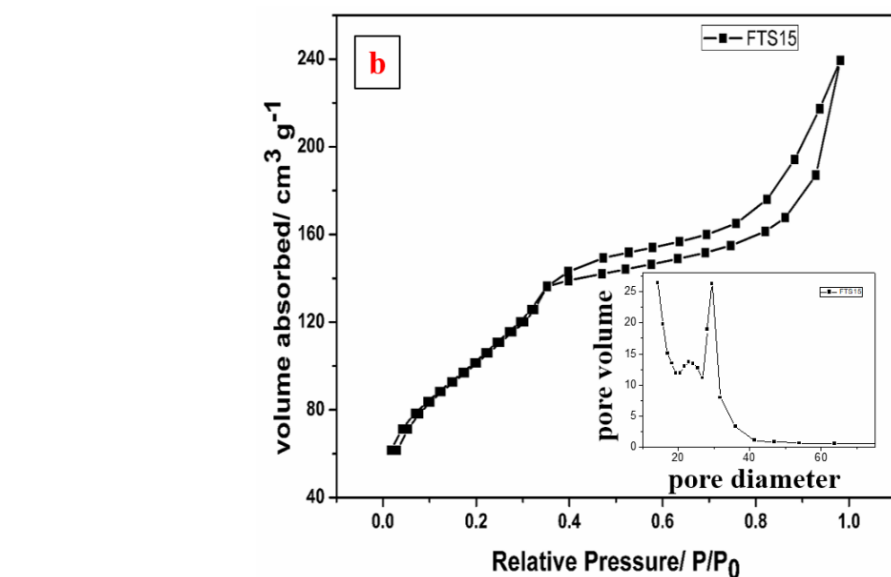


**Figure 3.5:** Nitrogen adsorption-desorption isotherm plots and pore size distribution curves (inset) of the prepared photocatalysts: (a) pure TS and (b) FTS15 hybrid composites

As shown in figure 3.5, a typical reversible type-IV adsorption isotherm of TS and FTS15 hybrid nanocomposite.<sup>[43]</sup> The nitrogen adsorption-desorption isotherm analysis was performed to examine the Brunauer–Emmett–Teller (BET) surface area of the synthesized pure Titanosilicate nanosheets and 15wt% FTS nanocomposite. As shown in figure 3.5 (a&b) the specific surface area of FTS15 was found to be  $417.31\text{ m}^2\text{ g}^{-1}$ , which is slightly higher than the pure TS ( $380.68\text{ m}^2\text{ g}^{-1}$ ). The pore-size distribution analysis of the samples were also estimated using the Barrett–Joyner–Halenda (BJH) method, and results shown in the inset of figure 3.5 (a&b). The pore distribution curves of both TS and FTS15 samples shown uniform pores with an average pore diameter of 3.0 nm, which is well consistent with the TEM observation. The large specific surface area and porous structure of Titanosilicate/Fe<sub>3</sub>O<sub>4</sub> nanocomposites were suitable for the better adsorption of organic compounds and also afford a larger number of reactive sites for the photocatalysis, thus improving the photocatalytic performance<sup>[44]</sup>.

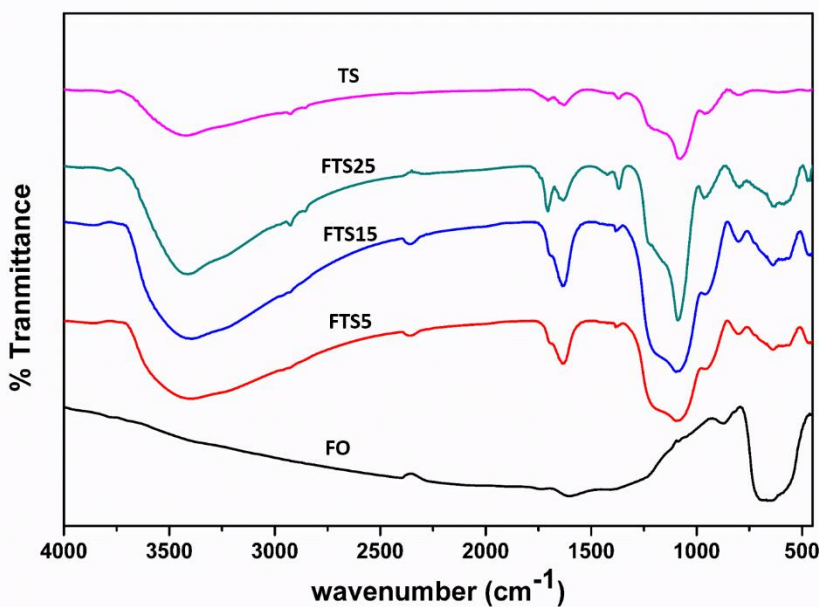


**Figure 3.6:** FTIR spectra of pure TS, pure FO, FTS5, FTS15 and FTS25 hybrid nanocomposites

Figure 3.6 shows the FTIR spectra of pure TS, pure FO, FTS5, FTS15, and FTS25 hybrid nanocomposites. The Fe-O broadband from 650 to 550  $\text{cm}^{-1}$  in the region is clearly observable in all compositions <sup>[33]</sup>. In the pure TS, the strong peaks of Si-O-Si bands observed at 467, 802 and 1100  $\text{cm}^{-1}$  and the Ti-O-Si band was observed at wavenumber 960  $\text{cm}^{-1}$  <sup>[45]</sup>. The characteristic peaks of TS and FO were retained in the titanosilicate/Fe<sub>3</sub>O<sub>4</sub> hybrid nanocomposite samples. However, 3600-3300  $\text{cm}^{-1}$  broadband around matching to OH stretching vibrations of H<sub>2</sub>O molecules, and 1300  $\text{cm}^{-1}$  peak related to the H-O-H bending band of the H<sub>2</sub>O molecules on the superficial of the products. The bands due to physically adsorbed water molecules arise from water released as a decomposition product that later gets adsorbed during the measurement.

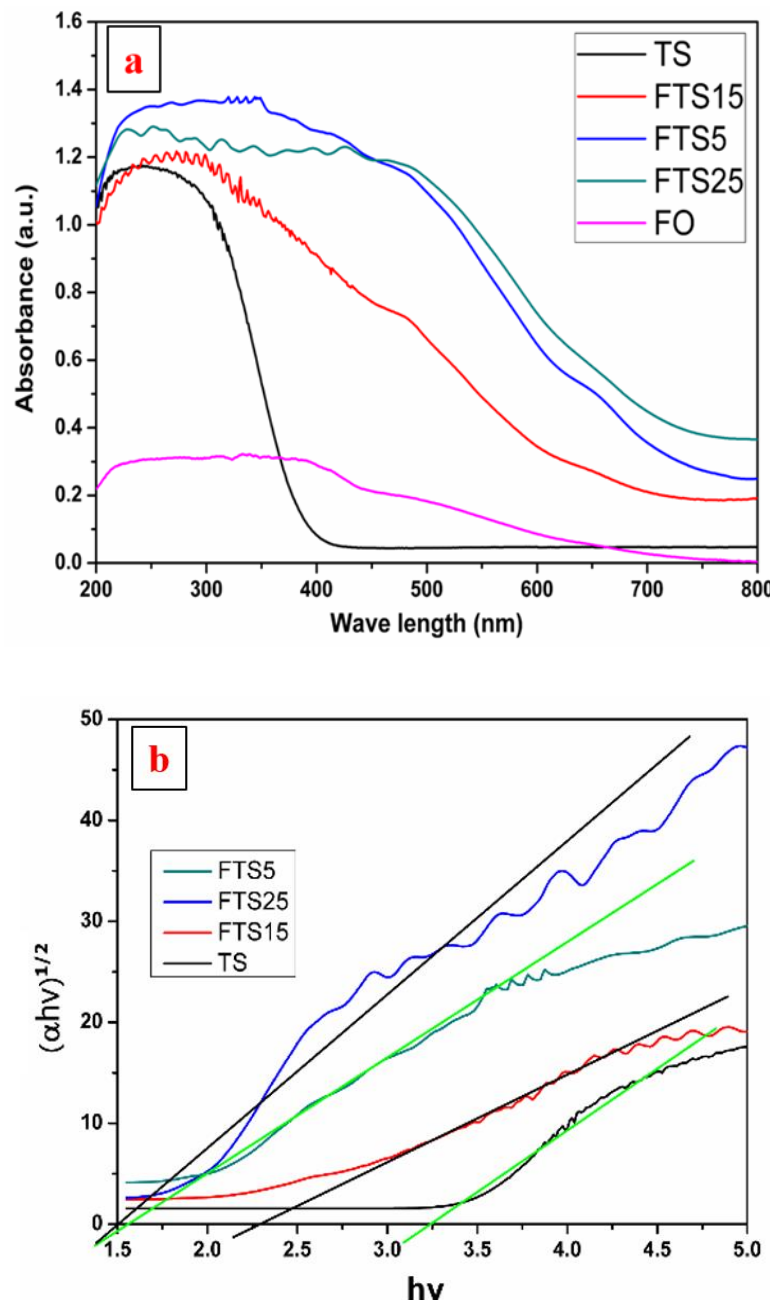


**Figure 3.7:** a) UV-Vis DRS of pure TS, Pure FO and FTS hybrid nanocomposites (b) Corresponding Tauc plots for band gap determination

Figure 3.7a illustrations the UV–Visible DRS spectra of pure  $\text{Fe}_3\text{O}_4$ , pure TS, and the FTS hybrid nanocomposites sample. The pure TS sample showed 385 nm adsorption edge, corresponding to a band gap of 3.22 eV, which implies its photocatalytic performance under UV light irradiation. The absorption of the FTS nanocomposites within the UV-light range significantly increased. These results are ascribed to the interface between the TS and the FO nanoparticles in the composite system. The improved light

absorption of the FTS nanocomposite led to the generation of more photoinduced electron-hole pairs under UV light irradiation, which subsequently resulted in enhanced photocatalytic activity. The band gap energy is found by plotting  $(\alpha h\nu)^2$  vs  $h\nu$  (figure 3.7b), where  $\alpha$  is the absorption coefficient and  $h\nu$  is the photon energy. The band gap energy is calculated by the intercept of the tangent to the plot. The band gap energies are 3.22, 1.68, 2.28 and 1.70. eV for TS, FTS5, FTS15, and FTS25 respectively.

### 3.4 Photocatalytic Activity Test

The photocatalytic performance of the as-synthesized compounds for the degradation of MB under UV light irradiation was examined (figure 3.8a). The photocatalytic degradation of MB using FTS15 hybrid nanocomposite under UV light irradiation (figure 3.8a). Furthermore, the adsorption capability of FTS15 was similarly studied in the dark for the same period (Figure 3.8b). These consequences specify that both light and catalyst are essential for photocatalytic degradation studies. The initial concentration of the MB solution was calculated and used as the initial concentration  $C_0$ . The  $C/C_0$  is taken as a Y-axis, where  $C$  is the actual concentration of MB and the irradiation time 't' is taken as a X-axis. Figure 8a shown, the MB concentration decreases more rapidly with FTS nanocomposites than pure TS and  $\text{Fe}_3\text{O}_4$ . The MB degradation was negligible in the absence of a catalyst under irradiation of the UV light, it is representing the high constancy of MB. The MB solution was allowed to stir in the dark for 30 min to reach adsorption-desorption equilibria, to study the catalyst adsorption effect. FTS nanocomposites were showed a much greater MB adsorption capability than pure TS. The results show the existence of the catalyst and UV light is necessary for MB dye degradation. Figure 3.8b shows that the plots of  $-\ln(C/C_0)$  vs irradiation time 't' were obtained straight lines, which indicates pseudo first-order kinetics of photocatalytic degradation of the MB. The optimum photocatalytic activity of FTS15 under UV light irradiation is almost 3.5 times higher than that of pure TS.

The kinetics of MB photodegradation on the catalyst surface can be defined via the pseudo-first-order kinetic equation  $-\ln(C/C_0) = kt$ , where  $k$  is the rate constant ( $\text{min}^{-1}$ ). The first-order rate constants ( $k$ ) reveal the rate of MB degradation over the synthesized photocatalysts using UV-light irradiation. As shown in figure 3.8b, the plot of the irradiation time (t) vs.  $-\ln(C/C_0)$  is closely a straight line (linear correlation coefficient,  $R^2$

$\geq 0.97$ ), indicating that the degradation curves fit with the pseudo-first-order kinetics equation model. The results revealed that the FTS15 hybrid nanocomposite shows the highest degradation rate ( $0.165 \text{ min}^{-1}$ ), which is almost 4 times higher than that of pure TS ( $0.0389 \text{ min}^{-1}$ ).

$\text{Fe}_3\text{O}_4$  spheres were loaded on porous titanosilicate, the photocatalytic performance improved apparently than the pure TS. The photocatalytic mechanism of FTS nanocomposites for MB degradation under UV light irradiation is illustrated in figure 3.9. The valence band (VB) and conduction band (CB) potentials of TS and  $\text{Fe}_3\text{O}_4$  were calculated via the following empirical formula.<sup>[46-49]</sup>

$$E_{VB} = X - E_e + 0.5 (Eg) \quad \text{and} \quad E_{CB} = E_{VB} - Eg$$

Where,  $E_{CB}$  is conduction band potential,  $E_{VB}$  is valance band potential,  $X$  is electronegativity of the compound,  $Eg$  is bandgap energy and  $E_e$  is free electrons energy on the hydrogen scale (4.5 eV). The electronegativity of TS and  $\text{Fe}_3\text{O}_4$  is 5.81 and 5.78 eV. The pure TS CB is -0.3 and VB is 2.92 eV, whereas CB and VB of  $\text{Fe}_3\text{O}_4$  is 1.13 and 1.23 eV, respectively. The band gap energy of  $\text{Fe}_3\text{O}_4$  (0.10 eV) is negligible.

When the UV light Irradiation on the FTS15 hybrid nanocomposite, electrons excited from the valence band to conduction band of the TS. The conduction band (CB) level of  $\text{Fe}_3\text{O}_4$  (1.13 eV) is lower than that of TS (-0.3 eV), so the CB electrons of TS can migrate to the CB of FO. The conductivity of FO is  $1.9 \times 10^6 \text{ S m}^{-1}$ , the electrons in iron oxide particles would have transferred to the surface of the catalyst and participated in the photocatalytic degradation. These would be the main cause for the improvement of the photocatalytic performance of FTS nanocomposites. In addition to this, by varying the amount of FO nanoparticles loading have an impact on the photocatalytic performance of the nanocomposites. Among the synthesized nanocomposites, FTS15 nanocomposite has the better activity for the degradation of MB, approximately 99% within 90 min.

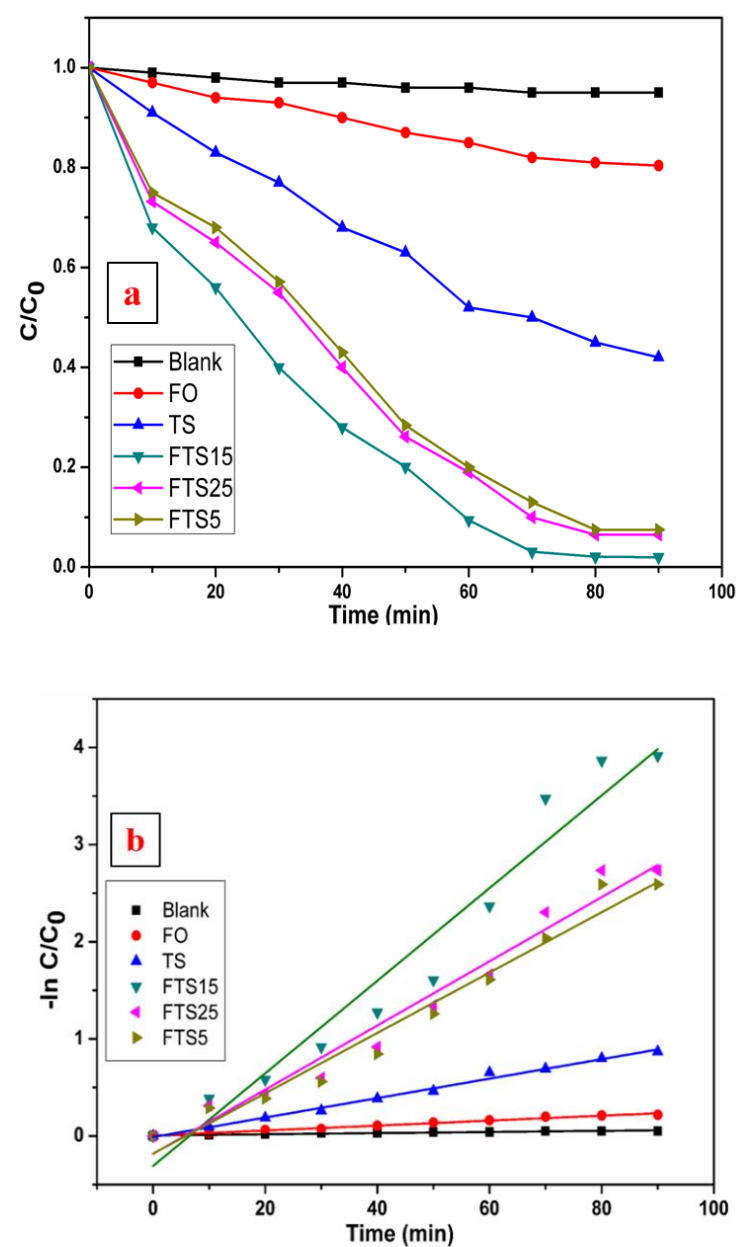


**Figure 3.8:** (a) Evaluation of the photocatalytic studies of TS, FO and FTS composites for the MB degradation under UV light irradiation and (b) pseudo first-order kinetics plots of TS, FO and FTS nanocomposites

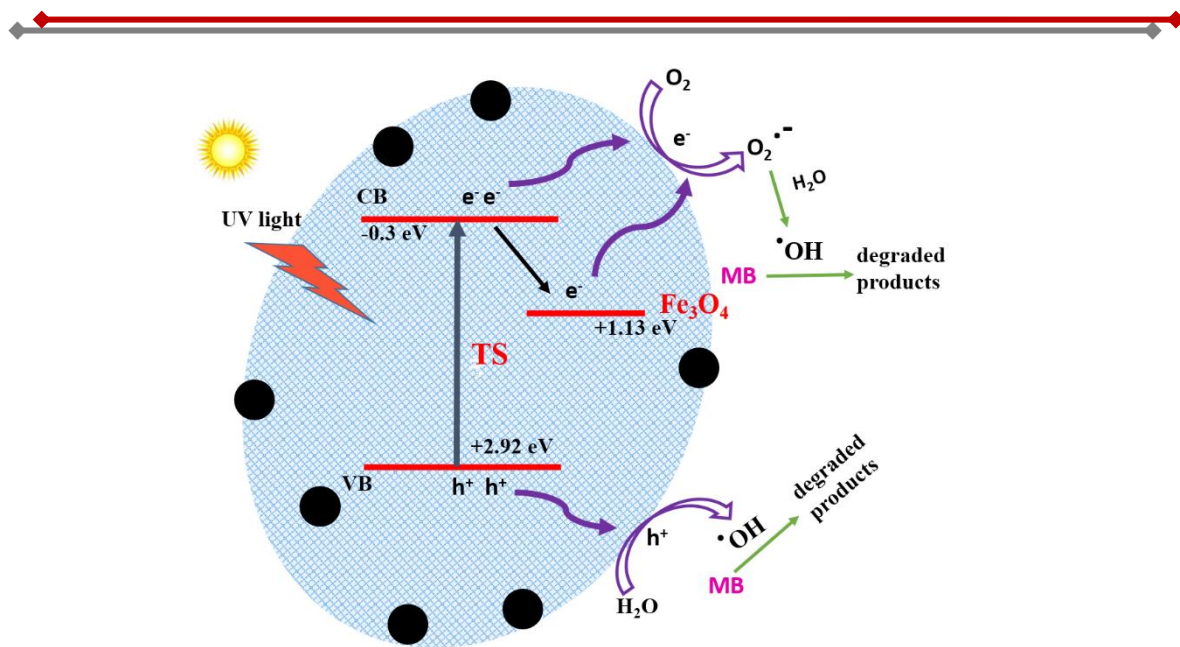


**Figure 3.9:** Photocatalytic mechanism of degradation of MB using FTS15 photocatalyst under UV light irradiation

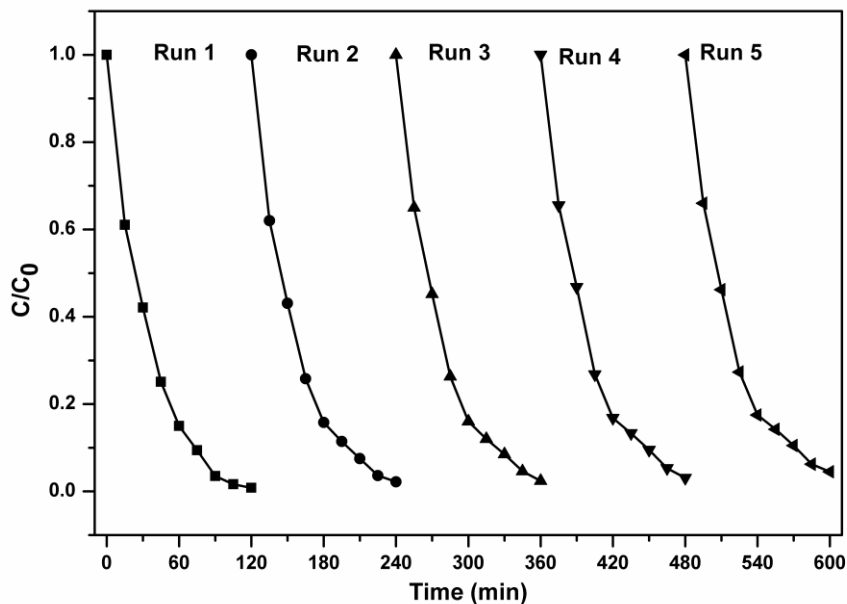


**Figure 3.10:** Reusability of the FTS15 nanocomposite for the photocatalytic degradation of MB

The photo-stability and reusability of the photocatalysts in acidic MB solution were achieved with five successive cyclic runs using the same photocatalyst (figure 3.10). In detail way, the aqueous solution of MB (10 ppm, 100 mL) was taken in 250 mL beaker, photocatalyst (0.1 g) was added and photocatalytic degradations were carried out by the

similar experimental process as that stated in the photocatalytic activity test. After the first cycle, the catalyst was separated by applying external magnetic field and washed with methanol. The recovered catalyst was transferred into another beaker with the help of a fresh MB (5 ppm, 100 mL) solution. Then, the dye-catalyst suspension was magnetically stirred for 30 min in the dark before irradiating with UV light. This procedure was repeated for five times.

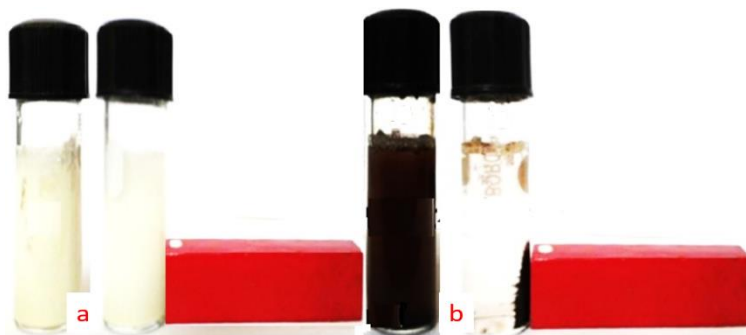


**Figure 3.11:** Pictures representing the separation of the a) Pure TS and b) separation of FTS15 nanocomposite from aqueous solution by applying external magnetic field

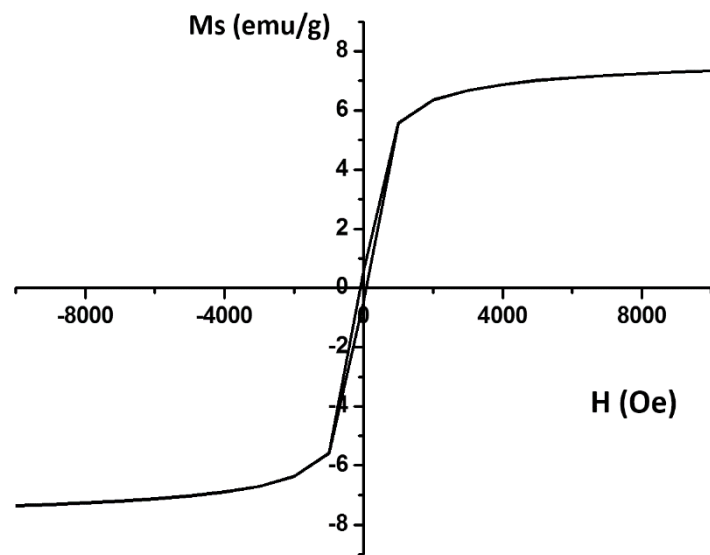


**Figure 3.12:** The room temperature magnetization curves of FTS15 hybrid nanocomposite

To accumulate and recover the photocatalyst in several cycles, its synthesis with worthy superparamagnetism is needed. Figure 3.11 shows, separation of FTS15 nanocomposite from aqueous solution by applying external magnetic field. Therefore, the FTS15 photocatalysts can be rapidly separated under an applied magnetic field. The room

temperature magnetization FTS15 hybrid nanocomposite is shown in figure 3.12. The magnetization curve has a Sigmoid shape without a hysteresis loop is indicates the superparamagnetic character of the as-prepared samples. The saturation magnetization value for FTS15 nanocomposite is 7 emu/g. the saturation magnetization of FTS15 was dropped down, compared to the pure  $\text{Fe}_3\text{O}_4$  due to a lower concentration of iron oxide NPs (ca. 15 wt.%) in FTS hybrid nanocomposite.

### 3.5 References

- [1] J. Tian, L. Zhang, X. Fan, Y. Zhou, M. Wang, R. Cheng, M. Li, X. Kan, X. Jin, Z. Liu, Y. Gao, J. Shi, *J. Mater. Chem. A* **2016**, *4*, 13814.
- [2] Y. Huang, Y. Liu, D. Zhu, Y. Xin, B. Zhang, *J. Mater. Chem. A* **2016**, *4*, 13626.
- [3] B. Liu, Z. Jin, L. Bai, J. Liang, Q. Zhang, N. Wang, C. Liu, C. Wei, Y. Zhao, X. Zhang, *J. Mater. Chem. A* **2016**, *4*, 14204.
- [4] X. Chang, T. Wang, J. Gong, *Energy Environ. Sci.* **2016**, *9*, 2177.
- [5] W.-N. Wang, *Aerosol Air Qual. Res.* **2014**, *14*, 533.
- [6] M. Marszewski, S. Cao, J. Yu, M. Jaroniec, *Mater. Horiz.* **2015**, *2*, 261.
- [7] H. Zhou, Y. Qu, T. Zeid, X. Duan, *Energy Environ. Sci.* **2012**, *5*, 6732.
- [8] H. Tong, S. Ouyang, Y. Bi, N. Umezawa, M. Oshikiri, J. Ye, *Adv. Mater.* **2012**, *24*, 229.
- [9] S. Kumar, T. Surendar, A. Baruah, V. Shanker, *J. Mater. Chem. A* **2013**, *1*, 5333.
- [10] R. Chandra, M. Nath, *ChemistrySelect* **2017**, *2*, 7711.
- [11] R. Hou, X. Chen, Y. Gao, H. Zhu, S. Li, H. Li, Y. Huo, *ChemistrySelect* **2016**, *1*, 1000.
- [12] D. D. La, A. Ranjanaware, M. Salimimaran, S. V. Bhosale, *ChemistrySelect* **2016**, *1*, 4430.
- [13] I. Majeed, M. A. Nadeem, F. K. Kanodarwala, E. Hussain, A. Badshah, I. Hussain, J. A. Stride, M. A. Nadeem, *ChemistrySelect* **2017**, *2*, 7497.
- [14] I. K. Konstantinou, T. A. Albanis, *Appl. Catal. B Environ.* **2004**, *49*, 1.
- [15] A. Fujishima, X. Zhang, D. Tryk, *Surf. Sci. Rep.* **2008**, *63*, 515.
- [16] X. Lu, Q. Wang, D. Cui, *J. Mater. Sci. Technol.* **2010**, *26*, 925.
- [17] Y. H. Sehlleier, S. Hardt, C. Schulz, H. Wiggers, *J. Environ. Chem. Eng.* **2016**, *4*, 3779.

[18] S. Kumar, S. T, B. Kumar, A. Baruah, V. Shanker, *J. Phys. Chem. C* **2013**, *117*, 26135.

[19] G. P. and B. N. M. Taramasso, *United StateS Patent [19]*, **1983**.

[20] J. H. Pan, H. Dou, Z. Xiong, C. Xu, J. Ma, X. S. Zhao, *J. Mater. Chem.* **2010**, *20*, 4512.

[21] M. Moliner, A. Corma, *Microporous Mesoporous Mater.* **2014**, *189*, 31.

[22] S. Uma, S. Rodrigues, I. N. Martyanov, K. J. Klabunde, *Microporous Mesoporous Mater.* **2004**, *67*, 181.

[23] F. X. Llabrés i Xamena, P. Calza, C. Lamberti, C. Prestipino, A. Damin, S. Bordiga, E. Pelizzetti, A. Zecchina, *J. Am. Chem. Soc.* **2003**, *125*, 2264.

[24] S. K. Das, M. K. Bhunia, A. Bhaumik, *J. Solid State Chem.* **2010**, *183*, 1326.

[25] S. Anandan, *Dye. Pigment.* **2008**, *76*, 535.

[26] C. M. a Parlett, K. Wilson, A. F. Lee, *Chem. Soc. Rev.* **2013**, *42*, 3876.

[27] K.-M. Choi, T. Yokoi, T. Tatsumi, K. Kuroda, *J. Mater. Chem. A* **2013**, *1*, 2485.

[28] M. Selvaraj, *Catal. Sci. Technol.* **2014**, *4*, 2674.

[29] M. V. Barmatova, I. D. Ivanchikova, O. a. Kholdeeva, A. N. Shmakov, V. I. Zaikovskii, M. S. Mel'gunov, *J. Mater. Chem.* **2009**, *19*, 7332.

[30] T.-D. Nguyen-Phan, E. W. Shin, V. H. Pham, H. Kweon, S. Kim, E. J. Kim, J. S. Chung, *J. Mater. Chem.* **2012**, *22*, 20504.

[31] C. Lei, F. Han, Q. Sun, W.-C. Li, A.-H. Lu, *Chem. - A Eur. J.* **2014**, *20*, 139.

[32] X. Li, X. Huang, D. Liu, X. Wang, S. Song, L. Zhou, H. Zhang, *J. Phys. Chem. C* **2011**, *115*, 21567.

[33] J. Xie, K. Chen, H. Lee, C. Xu, A. R. Hsu, S. Peng, X. Chen, S. Sun, *J. Am. Chem. Soc.* **2008**, *130*, 7542.

[34] P. Xu, G. M. Zeng, D. L. Huang, C. L. Feng, S. Hu, M. H. Zhao, C. Lai, Z. Wei, C. Huang, G. X. Xie, Z. F. Liu, *Sci. Total Environ.* **2012**, *424*, 1.

[35] Q. Yan, Z. Zhang, Y. Zhang, A. Umar, Z. Guo, D. O'Hare, Q. Wang, *Eur. J. Inorg. Chem.* **2015**, *2015*, 4182.

[36] L. Zhang, T. Wang, L. Yang, C. Liu, C. Wang, H. Liu, Y. A. Wang, Z. Su, *Chem. - A Eur. J.* **2012**, *18*, 12512.

[37] L. Ren, S. Huang, W. Fan, T. Liu, *Appl. Surf. Sci.* **2011**, *258*, 1132.

[38] G. Xi, B. Yue, J. Cao, J. Ye, *Chem. - A Eur. J.* **2011**, *17*, 5145.

[39] R. Chalasani, S. Vasudevan, *ACS Nano* **2013**, *7*, 4093.

[40] X. Yang, X. Zhang, Y. Ma, Y. Huang, Y. Wang, Y. Chen, *J. Mater. Chem.* **2009**, *19*, 2710.

[41] J. Su, M. Cao, L. Ren, C. Hu, *J. Phys. Chem. C* **2011**, *115*, 14469.

[42] (a) P. Xu, G. M. Zeng, D. L. Huang, C. L. Feng, S. Hu, M. H. Zhao, C. Lai, Z. Wei, C. Huang, G. X. Xie, Z. F. Liu, *Sci. Total Environ.* **2012**, *424*, 1. (b) J. Zhu, W. Zheng, B. He, J. Zhang, and M. Anpo, *J. Mol. Cat. A: Chemical* **2004**, *216*, 35. (c) M. Ni, M. K.H. Leung, D. Y.C. Leung and K. Sumathy, *Renewable and Sustainable Ene. Rev.* **2007**, *11*, 401.

[43] H. M. Abdelaal, *Chinese Chem. Lett.* **2014**, *25*, 627.

[44] S. Tonda, S. Kumar, V. Shanker, *J. Environ. Chem. Eng.* **2015**, *3*, 852.

[45] J. Sudhakareddy, R. Kumar, *J. Catal.* **1991**, *130*, 440.

[46] A. K. Adepu, R. Anumula, V. Narayanan, *Microporous Mesoporous Mater.* **2017**, *247*, 86.

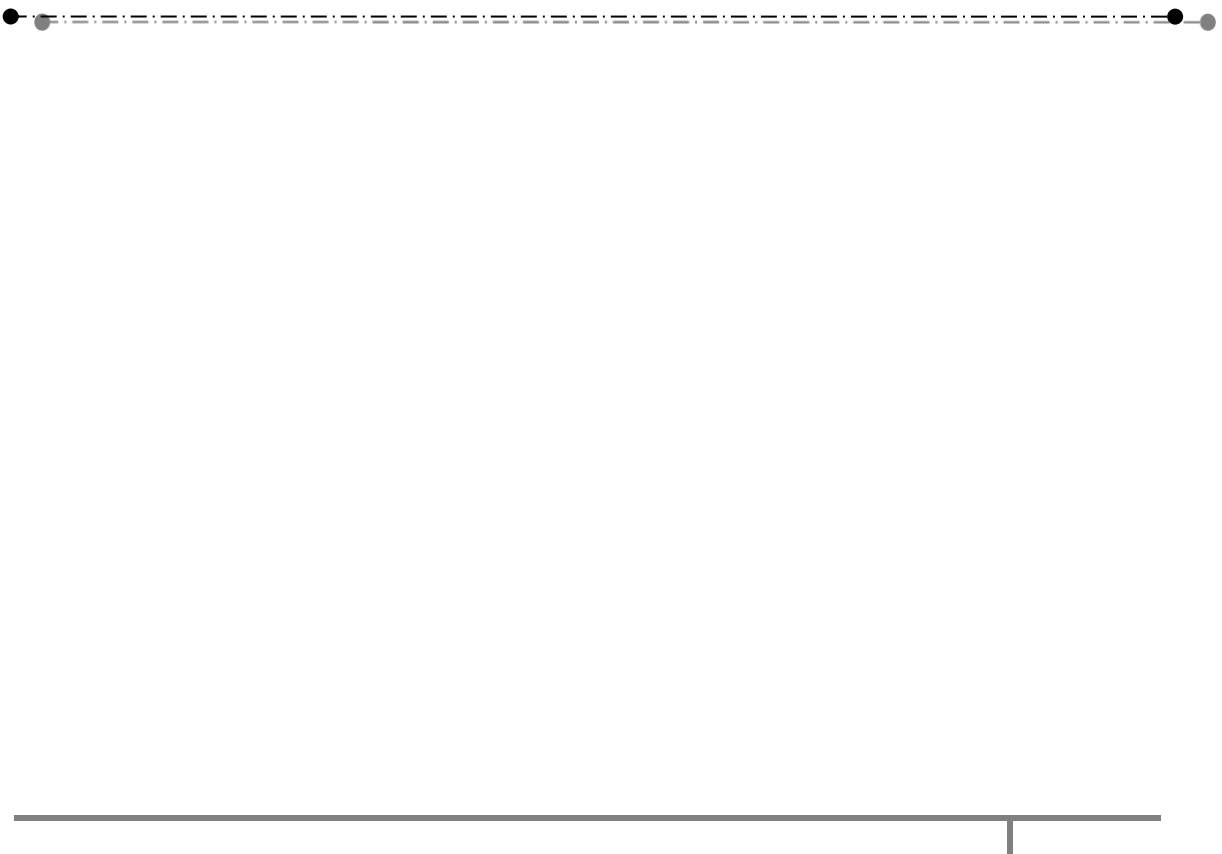
[47] Y. Cao, C. Li, J. Li, Q. Li, J. Yang, *Nanoscale Res. Lett.* **2015**, *10*, 251.

[48] A. K. Adepu, V. Katta, V. Narayanan, *New J. Chem.* **2017**, *41*, 2498.

[49] S. Xuan, W. Jiang, X. Gong, Y. Hu, Z. Chen, *J. Phys. Chem. C* **2009**, *113*, 553.

## CHAPTER IV

**Synthesis and Characterization of  
 $\text{Fe}_3\text{O}_4@\text{Titanosilicate}/\text{g-}\text{C}_3\text{N}_4$   
nanocomposites and their photocatalytic  
effect on the degradation of Rhodamine B  
under Sunlight irradiation**



## 4 Synthesis and Characterization of $\text{Fe}_3\text{O}_4$ @Titanosilicate/g-C<sub>3</sub>N<sub>4</sub> nanocomposites and their photocatalytic effect on the degradation of Rhodamine B under Sunlight irradiation

### 4.1 Introduction

Development of alternative clean energy supplies and pollution-free technologies for environmental remediation in the sustainable development of human society is an urgent need. Therefore, search for renewable energy sources and sustainable environmental technologies are primary challenges for enhancing the quality of human life.<sup>[1-5]</sup> Since the discovery of water splitting by Fujishima and Honda, the semiconductor photocatalysis technology has attracted considerable attention because of its potential applications in the photodegradation of organic pollutants, self-cleaning technology, hydrogen evolution from water and bacterial elimination using non-toxic, low cost methods.<sup>[6-11]</sup> Photocatalysis, in which sunlight is used as an energy source is one of the most promising technologies to overcome the present day energy and water pollution problems. The advantage of solar energy lies in its ecological purity. It offers the possibility of accomplishing energy cycles without environmental pollution and additional heating of the Earth. In the past few decades, tremendous efforts have been made for improving photocatalytic efficiency under visible light irradiation.<sup>[12-15]</sup> However, photocatalytic applications under the visible light are still limited due to the low efficiency caused by some challenging issues like narrow light-response range, surface structure, high recombination rate of charge carriers, poor material stability. Therefore, development of highly efficient visible light active photocatalysts is the current need.

Porous Titanosilicate (TS) material has been found to be able to catalyze the oxidation of aromatics, olefins and alcohols with hydrogen peroxide. Which is exclusively used in cyclohexanone ammoximation for its extremely high catalytic activity and selectivity. It has been proved that the active sites inside the mesoporous channels of TS are easily accessible. Titanosilicate is a semiconducting material that chemically activated by light. It has similar energy band gap of 3.0-3.2 eV like titanium dioxide. Titanosilicate also useful for photocatalytic dye degradation studies while the material is composite with another semiconductor. In each reaction, the Titanosilicate shows different physicochemical properties.<sup>[16-20]</sup> From the viewpoint of photocatalysis, previously reported that photocatalytic decomposition of NO and also Mesoporous

Titanosilicate/reduced graphene oxide composites doping effect and application in MB dye removal from water was reported by Thuy-Duong Nguyen-Phan *et al.*<sup>[21]</sup>

Graphitic carbon nitride ( $\text{g-C}_3\text{N}_4$ ) is a two-dimensional old synthetic polymer and its precursors were first defined by Berzelius and Liebig. Many challenges (non-metal loading and metal doping and combination with another suitable semiconductor) for the developments of the photocatalytic performance of  $\text{g-C}_3\text{N}_4$  were made by encouraging the parting of photo-generated charges. Among them, the novel  $\text{g-C}_3\text{N}_4$  based heterostructure photocatalysts were broadly synthesized to increase  $\text{H}_2$  and  $\text{O}_2$  growth performances, decomposition of formaldehyde in air and photodegradation of organic pollutants.<sup>[15,22–28]</sup> However, the photoactivity of  $\text{g-C}_3\text{N}_4$  is still low compared with the traditional photocatalysts, such as  $\text{TiO}_2$  and  $\text{ZnO}$ .<sup>[29,30]</sup>

In this chapter, synthesis of magnetic  $\text{Fe}_3\text{O}_4$ @Titansilicate/ $\text{g-C}_3\text{N}_4$  (FTSCN) nanocomposite, even though the photocatalytic activities of  $\text{g-C}_3\text{N}_4$ , Titansilicate and its hetero nanostructures are extensively known and have initiated widespread research interest. In the current research work, to develop magnetically separable and cost-effective material with estimated to be outstanding photocatalytic properties in the direction of dye degradation under irradiation of solar-light. These photocatalysts can be easily recovered by an external magnetic field and can be separated from a photocatalytic reaction system several times without any significant reduction in photocatalytic performance. The FTSCN photocatalyst more efficient in direct sun light compared to visible light. Direct sunlight has 45% of visible light, 5% of UV light and 50% of IR light.

## 4.2 Experimental details

### 4.2.1 Materials

Tetraethyl orthosilicate (TEOS, 98.0%, Sigma-Aldrich) and Titanium isopropoxide (TTIP, 97.0%, Sigma-Aldrich), Melamine (99.0%, Sigma-Aldrich), Ferrous chloride (99.0%, Sigma-Aldrich), Ferric chloride (99.9% metal-based, 10.0% w/v, Sigma-Aldrich) Cetyltrimethyl ammoniumbromide (CTAB, 98.0%, SD fine), Ethanol (97.0%, SD fine) and ammonia solution (25.0%, SD fine). All aqueous solution were prepared with millipore water.

## 4.2.2 Method

### 4.2.2.1 Preparation of $\text{Fe}_3\text{O}_4$ Magnetic nanoparticles (FO)

0.198 g of  $\text{FeCl}_2 \cdot 4\text{H}_2\text{O}$ , 0.338 g of  $\text{FeCl}_3 \cdot 6\text{H}_2\text{O}$  were taken in a beaker containing 50 mL of millipore water and sonication for 40 min then heated to 343 K with stirring for 1 h. 5 mL of ammonia solution was added to the reaction mixture and the solution turns to black color. The final mixture was taken into an autoclave at 453 K for 8 h. The obtained product was collected by centrifugation after washing and dried at 353 K for 12 h.

### 4.2.2.2 Preparation of $\text{Fe}_3\text{O}_4@\text{Titanosilicate}$ (FTS)

In the typical synthesis of magnetically separable porous Titanosilicate was completed using a two-step one-pot process. The above synthesized FO 150 mg was dispersed in 160 mL of ethanol and 40 mL of millipore water and 5 mL of aqueous ammonia were added to the mixture. The mixture was sonicated in an ultrasonic bath for 30 min. 100 mL of 0.3 mg CTAB solution in water was added to the mixture under vigorous stirring. After 30 min, the appropriate ratio of the Ti:Si mixture was dropwise added to the above mixture under vigorous stirring and the suspension was additionally stirred for 8 h at RT. The above reaction mixture was placed in an autoclave for hydrothermal treatment at 393 K for 24 h. Then the solid sample was separated by centrifugation, washed two times with millipore water and dried at 353 K. The obtained product was calcined at 550 °C for 5 h in the presence of air to remove the structure directing agent from the material.<sup>26</sup> The calcined sample was collected,  $\text{Fe}_3\text{O}_4@\text{Titanosilicate}$  named as FTS.

### 4.2.2.3 Preparation of $\text{Fe}_3\text{O}_4@\text{Titanosilicate/g-C}_3\text{N}_4$ (FTSCN) hybrid nanocomposite

Porous magnetically separable  $\text{Fe}_3\text{O}_4@\text{Titanosilicate/g-C}_3\text{N}_4$  (FTSCN) heterojunction photocatalysts were fabricated by calcining the mixtures of the melamine and highly magnetic porous FTS. An appropriate amount of melamine was dispersed in 100 mL of methanol and then 0.5 g of highly magnetic porous FTS was added. The suspension was transferred to a beaker and heated upto 80 °C until the evaporation of the methanol. Subsequently, this dried mixture was placed in an alumina boat and then calcined at 550 °C for 2 h with a ramping rate of 5 °C min<sup>-1</sup> in the presence of atmospheric air. After cooling down to RT, the final pale yellow porous FTSCN hybrid nanocomposites

were collected. In order to discuss the role of g-C<sub>3</sub>N<sub>4</sub> content on the photocatalytic activity of FTSCN heterojunction photocatalysts, samples with different amount of melamine in the precursors were prepared under the similar conditions. The products were named as FTSCNx, where the 'x' referred to the weight of melamine used. For example, FTSCN3 represented the sample prepared from 3 g of melamine and 0.5 g of FTS, similarly FTSCN3.5, FTSCN4 synthesized.<sup>[31]</sup> Pure g-C<sub>3</sub>N<sub>4</sub> was directly annealed at the above condition by using melamine. The obtained light yellow product of g-C<sub>3</sub>N<sub>4</sub> named as CN.

#### 4.2.3 Photocatalytic activity of FTSCN nanocomposites

Rhodamine B (RhB) dye was used to study the photocatalytic performance of the synthesized pure samples, FTSCN nanocomposites. Nanocomposites (10 mg) was dispersed in 100 ml of MB dye solution and maintained at constant stirring in a dark room for 30 min for the adsorption equilibrium of the dye molecules. Then the suspended solution was irradiated by sunlight, UV and visible light sources for different time intervals. All the experiments were conducted in a similar environment at the temperature of 35 °C. The absorbance of the collected samples was recorded by using the UV-Visible spectrophotometer. 150 W tungsten visible lamp used for visible light. The wave length range is 400 to 800 nm.

### 4.3 Results and Discussion

#### 4.3.1 Powder-XRD Analysis

The figure 4.1 shows, PXRD spectra of the pure FO, FTS, pure CN, FTSCN3, FTSCN3.5 and FTSCN4 nanocomposites. For the pure CN, the characteristic diffraction peaks at 13.1° and 27.4° which exactly analogous to g-C<sub>3</sub>N<sub>4</sub> (JCPDS No. 87-1526).<sup>[31]</sup> A small broad peak centered at 23° was ascribed to the porous Titanosilicate (JCPDS No. 29-0085). All diffraction peaks of Fe<sub>3</sub>O<sub>4</sub> are in good agreement with the bulk Fe<sub>3</sub>O<sub>4</sub> crystal phase (JCPDS: 01-1111).<sup>[32]</sup> No other phase of impurity peaks has been detected, indicating high purity of Fe<sub>3</sub>O<sub>4</sub>. Similar peaks were found in Fe<sub>3</sub>O<sub>4</sub>@TS/g-C<sub>3</sub>N<sub>4</sub> composites FTSCN3, FTSCN3.5 and FTSCN4. No additional diffraction peaks of other phases have been detected.

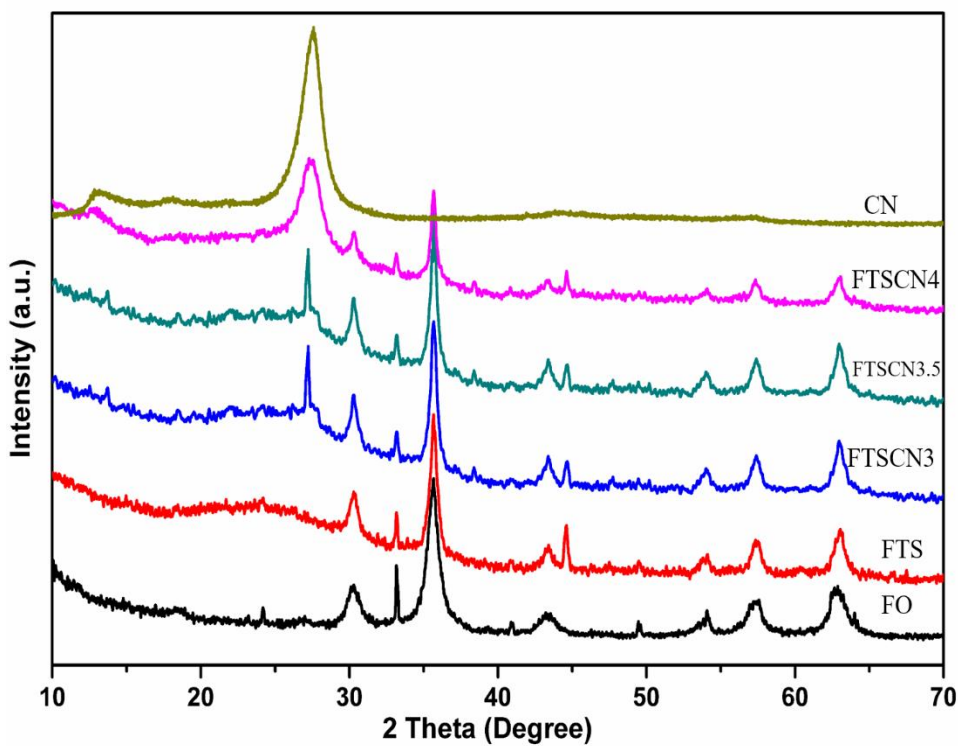


**Figure 4.1.** XRD spectra of, pure FO, pure CN, FTS and FTSCN3, FTSCN3.5, FTSCN4 nanocomposites

#### 4.3.2 Morphology characterization and EDX Analysis

The morphology and structure of the ternary nanocomposites were investigated by FE-SEM, TEM and HR-TEM. Figure 4.2 shows that the pure FO particles, FTS and FTSCN3, FTSCN3.5, FTSCN4 nanocomposites. Figure 4.2a shows agglomeration of the spherical shape of the pure FO magnetic nanoparticles. Titanosilicate was successfully coated on the  $\text{Fe}_3\text{O}_4$  nanoparticles of as-prepared FTS composite shown in figure 4.2b. The FESEM image (figure 4.2c) clearly shown that many particles in homogeneous size were deposited on the  $\text{g-C}_3\text{N}_4$ . The layered structure of  $\text{g-C}_3\text{N}_4$  was clearly distinguished in FESEM image (figure 4.2 d-f). High loading concentration of  $\text{Fe}_3\text{O}_4$  gave severe aggregation of the FTS nanoparticles and uneven dispersion across the  $\text{g-C}_3\text{N}_4$  surface.

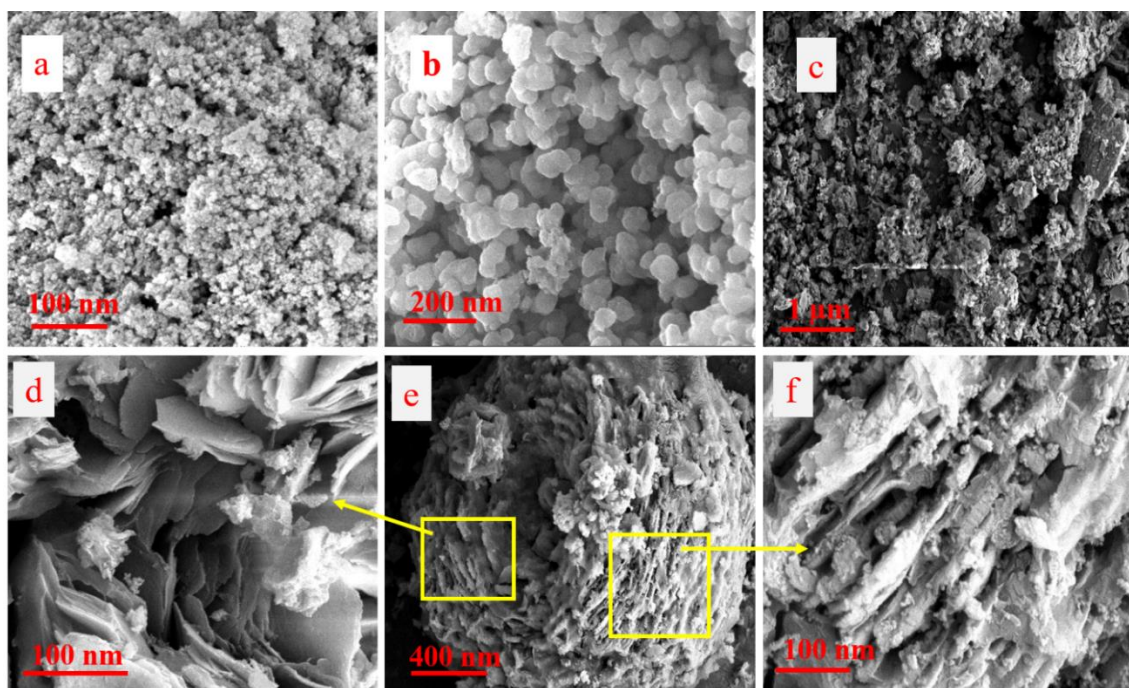


**Figure 4.2:** FE-SEM images of a) pure  $\text{Fe}_3\text{O}_4$ , b) FTS, C) FTSCN3.5 and d-f) magnified FTSCN3.5

From the TEM analysis spherical structure of the pure  $\text{Fe}_3\text{O}_4$  nanoparticles was confirmed and shown in figure 4.3a and figure 4.3(b&c) shows that core-shell structure of the  $\text{Fe}_3\text{O}_4$ @Titanosilicate nanocomposite. These images indicate that the surfaces of  $\text{Fe}_3\text{O}_4$ @titanosilicate microspheres were rough and porous. A large number of  $\text{Fe}_3\text{O}_4$  nanoparticles are encapsulated in the core of titanosilicate shell, forming the pomegranate-like structure. The measured interplanar spacing of the core is 0.25 nm, confirmed that the XRD plane is 311 which corresponds to the  $\text{Fe}_3\text{O}_4$ . Figure 4.3(d&e) shows Core-shell of the  $\text{Fe}_3\text{O}_4$ @Titanosilicate deposited on the  $\text{g-C}_3\text{N}_4$  nanosheets. Which can make the dyes better contact with the catalysts so as to achieve the purpose of degradation. Figure 4.3f shows the measured interplanar spacing is 0.32 nm, which corresponds to the  $\text{g-C}_3\text{N}_4$  (002) plane.

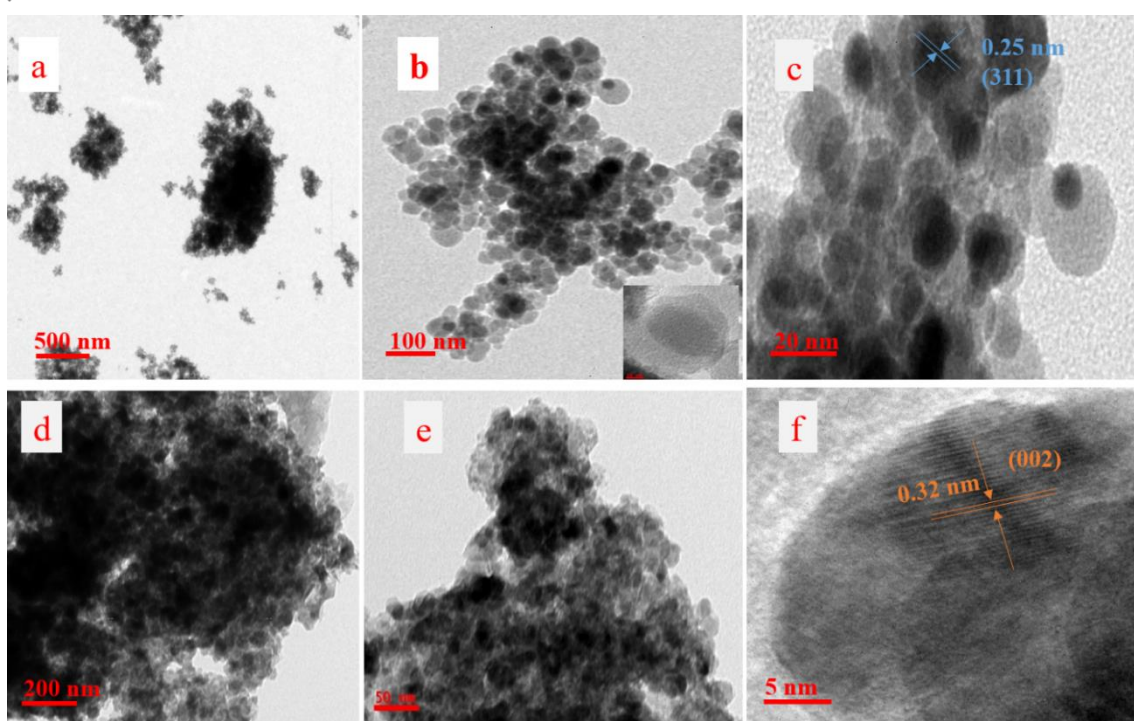


**Figure 4.3:** TEM images of a) pure  $Fe_3O_4$ , b&c) FTS (inset is core-shell of FTS), d) FTSCN3.5, e) magnified FTSCN3.5 and f) HR-TEM image of FTSCN3.5

### 4.3.3 FTIR Analysis

The figure 4.4 shows, FTIR spectrum of the pure FO, pure CN, FTS, FTSCN3, FTSCN3.5 and FTSCN4 nanocomposites. For the pure CN, the peaks ranging from 1200 to 1640  $cm^{-1}$  confirmed the presence of two main bands in the products. The peak at 1638  $cm^{-1}$  corresponded to the  $sp^2$  C=N stretching vibration modes, while the peaks at 1242  $cm^{-1}$ , 1324  $cm^{-1}$  and 1411  $cm^{-1}$  were assigned to the aromatic  $sp^3$  C-N bonds. In addition, the peak at 807  $cm^{-1}$  was due to the out of plane skeletal bending modes of triazine.<sup>[33,34]</sup> For the sample of pure  $Fe_3O_4$ , the vibrational bands at around 520  $cm^{-1}$  is characteristic of the (Fe–O) lattice vibrations.<sup>[35]</sup> FT-IR spectra of the FTS nanocomposite, shows that peaks around 1700 and 3430  $cm^{-1}$  corresponding to the carboxyl and hydroxyl groups respectively. The strong peaks near 1100, 802 and 467  $cm^{-1}$  agree to the Si-O-Si band, 960  $cm^{-1}$  bands is observed that the Ti peak in Titanosilicate. Thangaraj *et al.* have verified that the 960  $cm^{-1}$  band shown by TS zeolites can also be attributed to a stretching mode of a  $[SiO_4]$  unit bonded to a  $Ti^{+4}$  ion  $[O_3SiOTi]$ . The characteristic peaks of FTS and CN have retained in the FTSCN3, FTSCN3.5, FTSCN4 hybrid nanocomposites.<sup>[36]</sup>

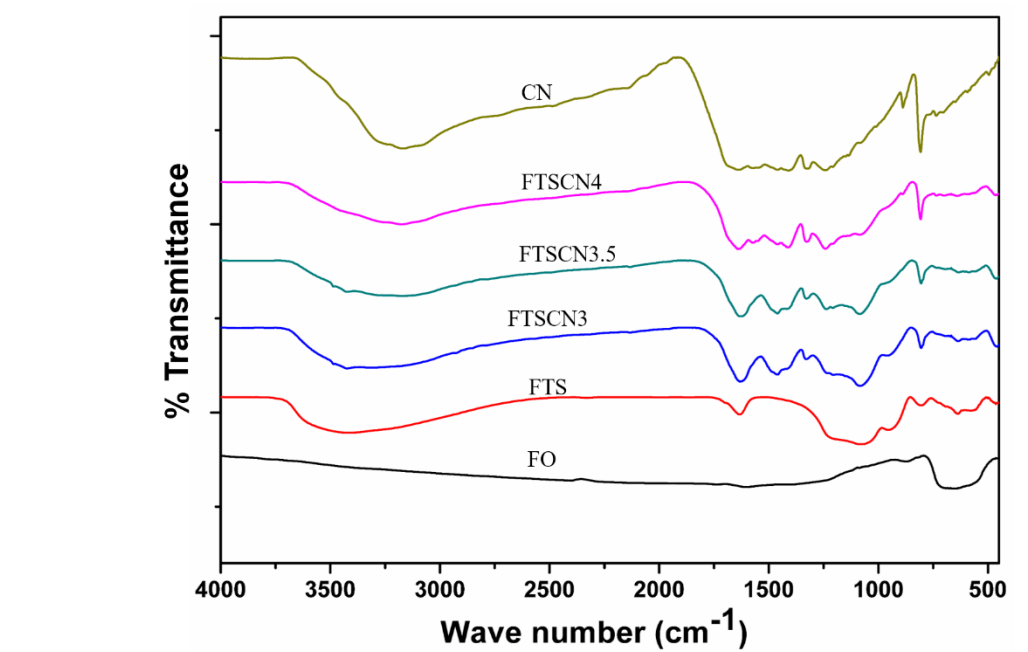


**Figure 4.4:** FTIR Spectra of pure FO, FTS, pure CN, FTSCN3, FTSCN3.5 and FTSCN4 nanocomposites

#### 4.3.4 UV-Visible DRS Spectra

In general, the optical absorption assets of photocatalyst show a significant role in determining the photocatalytic activity, mainly for photocatalytic degradation of organic pollutants under irradiation of visible light. The figure 4.5 shows, UV-visible DRS to studies of pure FO, pure CN, FTS and the FTSCN3, FTSCN3.5, FTSCN4 nanocomposites. Pure  $\text{g-C}_3\text{N}_4$  exhibited a wider photo absorption from UV to visible light, and its band gap is 2.80 eV, the absorption edge was around 450 nm. Which resulted from the charge-transfer response from valence band (VB) migrated by N 2p orbit to the conduction band (CB) formed by C 2p orbit.<sup>[37]</sup>

It is notable that the FTSCN hybrid nanocomposites displayed the broader absorption edge and extended to the visible region as compared to that of pure FTS. This may be ascribed to the presence FTS of on  $\text{g-C}_3\text{N}_4$  surface. Further observation showed that with increasing the melamine content in the precursors, there was a red shift of the UV-vis absorption edge for all FTSCN nanocomposites, indicating the decrease in the band gap.<sup>[38]</sup> In this work, the band gaps are estimated to be 1 eV, 2.8 eV, 2.1 eV, 2.20 eV, 2.16 eV and 2.14 eV from the absorption edge, corresponding to the pure  $\text{Fe}_3\text{O}_4$ , pure  $\text{g-C}_3\text{N}_4$ , FTS, FTSCN3, FTSCN3.5 and FTSCN4 samples, respectively.

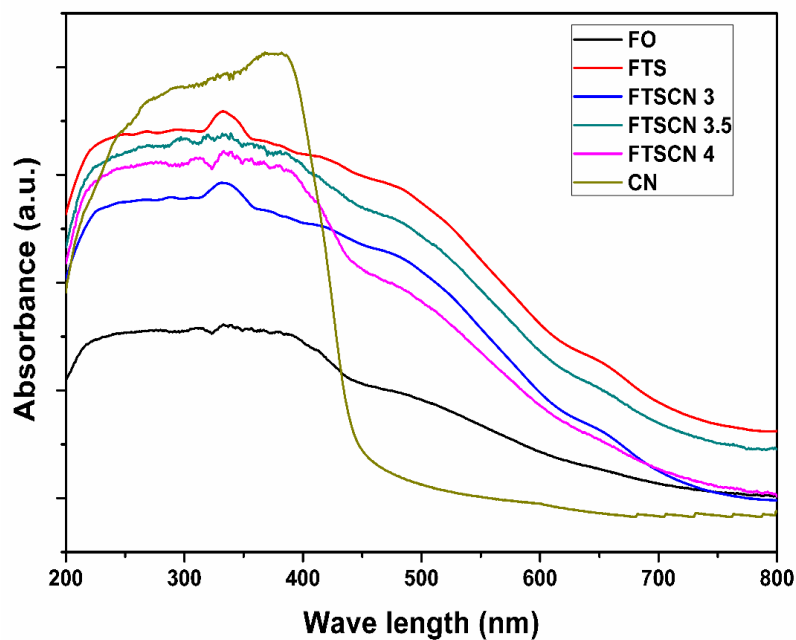


**Figure 4.5:** UV-DRS Spectra of pure FO, pure CN, FTS, FTSCN3, FTSCN3.5 and FTSCN4 nanocomposites

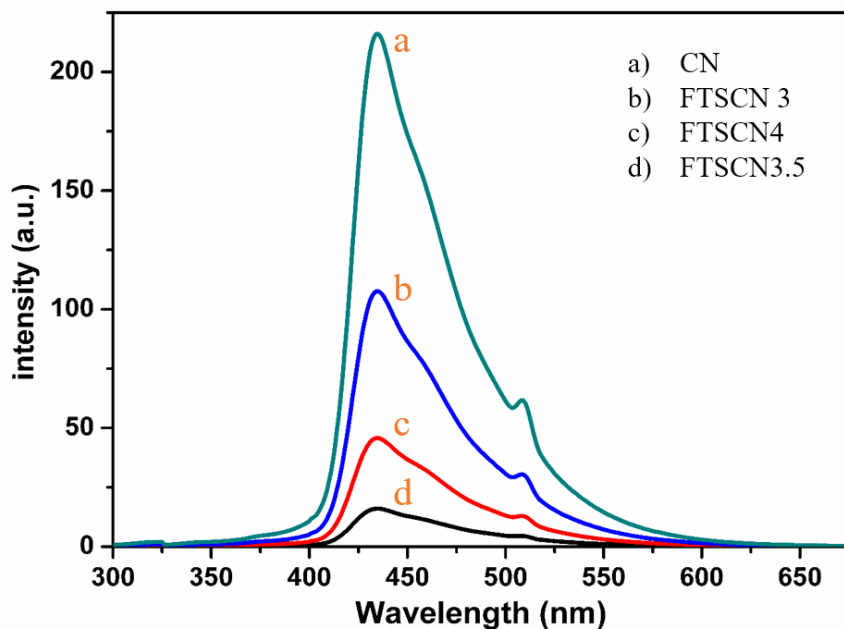


**Figure 4.6:** Photoluminescence Spectra of pure CN and FTSCN3, FTSCN3.5, FTSCN4 nanocomposites exited at 365 nm

#### 4.3.5 Photoluminescence analysis

The Photoluminescence spectra of the synthesized pure g-C<sub>3</sub>N<sub>4</sub>, FTSCN3, FTSCN3.5 and FTSCN4 recorded at RT with an excitation wavelength of 365 nm as shown in figure 4.6. A lower PL intensity for FTSCN3.5 clearly indicates a larger

concentration and increase the lifetime of electron-hole pairs. The PL data support the results of RhB photodegradation experiment showing enhanced activity over FTSCN3.5. It is broadly established that improvement of the photocatalytic activity of a photo-catalyst is ascribed to efficient photogenerated electron-hole pair separation. The recombination rate of photogenerated and lifetime of electron-holes in the semiconductor catalysts could be investigated by PL analysis.

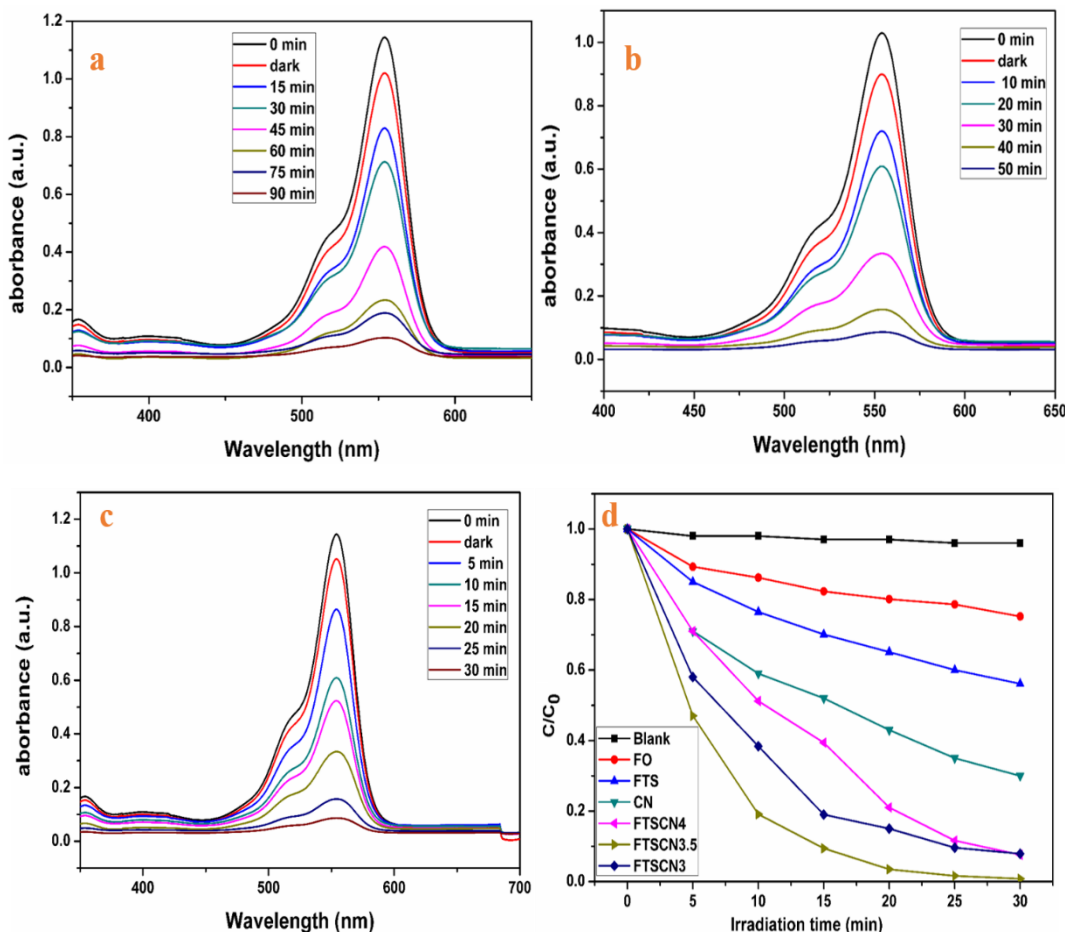


**Figure 4:** Photodegradation of RhB dye under the irradiation of (a) UV- light, (b) visible light, (c) direct sunlight and (d)  $C/C_0$  Vs time (min) for the FTSCN nanocomposites

#### 4.4 Photocatalytic degradation

Figure 4.7 shows the photocatalytic performance of the synthesized FTSCN nanocomposite was analyzed using RhB dye under direct sunlight, UV and visible light irradiations. Figure 4.7a shows the UV light irradiation for different time intervals and the RhB dye degradation rate was observed. The absorption spectra of the RhB dye solution with FTSCN nanocomposite under irradiation of visible light for different time intervals

as shown in figure 4.7b. This result shows that visible light irradiated RhB dye with FTSCN nanocomposite solution was degraded quickly within 50 min compared to UV irradiation. Figure 4.7c shows the absorption spectra of RhB dye solution with FTSCN nanocomposite under direct sunlight irradiation for different time intervals. The dye degrades at a faster rate under sunlight (30 min) compared to UV and visible light sources as the sunlight has a higher intensity. To demonstrate the influence of  $\text{g-C}_3\text{N}_4$  on the photodegradation, the degradation of RhB with pure FTS was studied under visible light. Figure 4.7d shows the variation of  $\text{C}/\text{C}_0$  with time for pure samples and nanocomposite, where  $\text{C}_0$  is the initial concentration of the dye solution and  $\text{C}$  is the concentration of the dye solution with respect to the degradation time ‘ $t$ ’. It is obvious from the figure 4.7d that the rate of degradation was quite faster in the FTSCN3.5 composite compared to pure samples and other FTSCN nanocomposites, which shows the beneficial impact of  $\text{g-C}_3\text{N}_4$  on the photocatalytic performance of the composite.

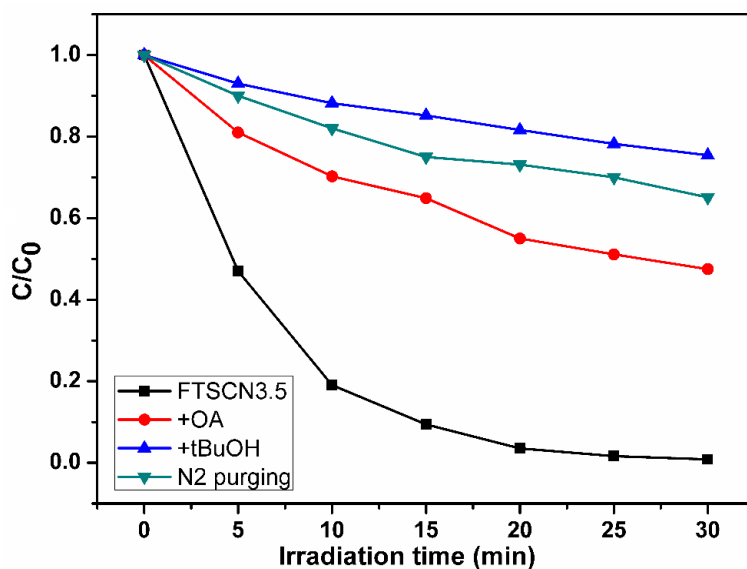


**Figure 4.8:** Scavengers effects on the RhB photodegradation in the existence of FTSCN3.5 nanocomposite under visible-light irradiation

#### 4.4.1 Reactive species

Mostly reactive species  $\cdot\text{OH}$ ,  $\text{O}_2^{\cdot-}$ , and  $\text{h}^+$  are played an important role in the photocatalysis. As shown from figure 4.8, the addition of *tert*butanol (*t*-BuOH) it is acting as a hydroxyl radical scavenger, the rate of photodegradation was considerably suppressed for RhB degradation compared with only photocatalyst (without scavenger). The addition

of  $\text{N}_2$  purging acting as a superoxide radical scavenger, a major variation was detected in the rate of degradation. Meanwhile, the addition of ammonium oxalate (AO) was conducted which acting as a hole scavenger, some variation in the degradation of RhB was observed. These results are revealed that the  $\cdot\text{OH}$ ,  $\text{O}_2^{\cdot-}$ , and  $\text{h}^+$  are significant reactive species in FTSCN hybrid nanocomposites.

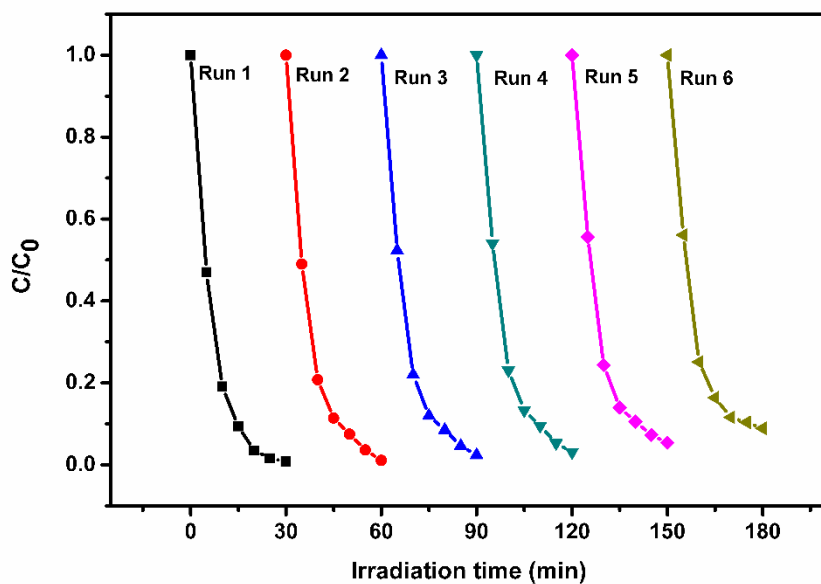


**Figure 4.9:** Recyclability of the FTCN3.5 photocatalyst for the RhB photodegradation under visible-light irradiation

The photo-stability and reusability of the photocatalysts in RhB solution were achieved with five successive cyclic runs using the same photocatalyst (figure 4.9). In detail way, the aqueous solution of RhB (5 ppm, 100 mL) was taken in 250 mL beaker, photocatalyst (0.1 g) was added and photocatalytic degradations were carried out by the similar experimental process as that stated in the photocatalytic activity test. After the first cycle, the catalyst was separated by applying external magnetic field and washed with methanol. The recovered catalyst was transferred into another beaker with the help of a fresh RhB (5 ppm, 100 mL) solution. Then, the dye-catalyst suspension was magnetically stirred for 30 min in the dark before irradiating with UV light. This procedure was repeated for five times.

The room temperature magnetization pure FO, FTSCN3.5 hybrid nanocomposite are shown in figure 4.10. The magnetization curve has a Sigmoid shape without a hysteresis loop is indicates the superparamagnetic character of the as-prepared samples.

The saturation magnetization value for FTSCN3.5 nanocomposite is 9 emu/g. the saturation magnetization of FTSCN3.5 dropped down compared to the pure FO due to a lower concentration of iron oxide NPs in FTSCN3.5 hybrid nanocomposite. To accumulate and recover the photocatalyst in several cycles, its synthesis with worthy superparamagnetism is needed. Figure 4.10 (inset) shows, separation of FTSCN3.5 nanocomposite from aqueous solution by applying external magnetic field. Therefore, the FTSCN3.5 photocatalysts can be rapidly separated under an applied magnetic field.

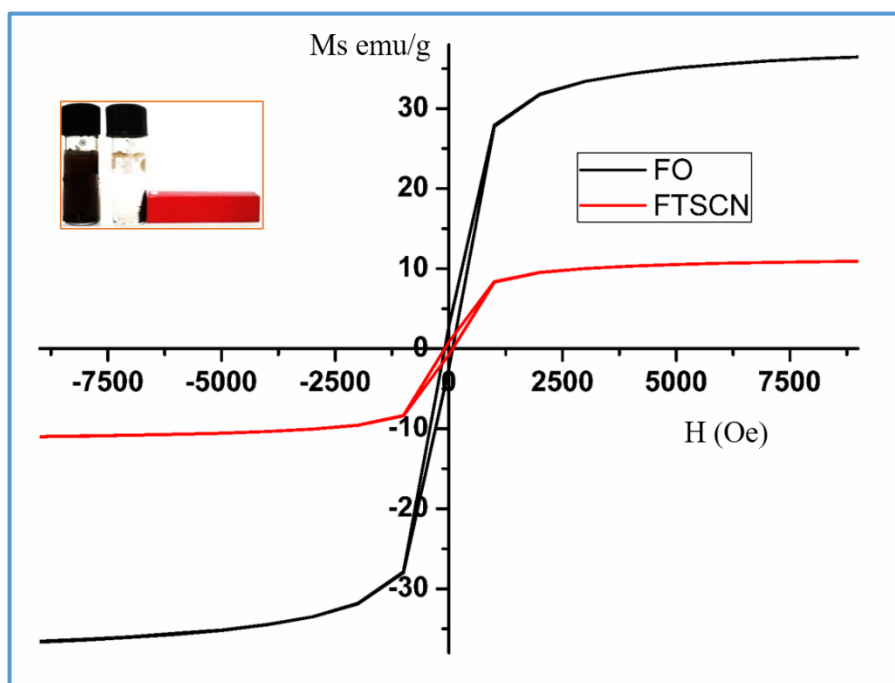


**Figure 4.10:** The magnetization curves of FTSCN3.5 hybrid nanocomposite at RT and separation of FTSCN3.5 hybrid nanocomposite from aqueous solution by applying external magnetic field (inset figure)

#### 4.5 References

- [1] M. R. Hoffmann, S. T. Martin, W. Choi, D. W. Bahnemann, *Chem. Rev.* **1995**, *95*, 69.
- [2] P. V. Kamat, *Chem. Rev.* **1993**, *93*, 267.
- [3] A. L. Linsebigler, G. Lu, J. T. Yates, *Chem. Rev.* **1995**, *95*, 735.
- [4] A. Mills, S. Le Hunte, *J. Photochem. Photobiol. A Chem.* **1997**, *108*, 1.
- [5] A. Fujishima, T. N. Rao, D. A. Tryk, *J. Photochem. Photobiol. C Photochem. Rev.* **2000**, *1*, 1.
- [6] A. Fujishima, K. Honda, *Nature* **1972**, *238*, 37.

[7] X. Chen, S. Shen, L. Guo, S. S. Mao, *Chem. Rev.* **2010**, *110*, 6503.

[8] B. Wawrzyniak, A. W. Morawski, B. Tryba, *Int. J. Photoenergy* **2006**, *2006*, 1.

[9] P. Roy, T. Dey, K. Lee, D. Kim, B. Fabry, P. Schmuki, *J. Am. Chem. Soc.* **2010**, *132*, 7893.

[10] Y. Y. Song, F. Schmidt-Stein, S. Bauer, P. Schmuki, *J. Am. Chem. Soc.* **2009**, *131*, 4230.

[11] B. G. Apperrot, A. Lipovsky, R. Dror, N. Perkas, Y. Nitzan, R. Lubart, A. Gedanken, *Adv. Funct. Mater.* **2009**, *19*, 842.

[12] H. Gerischer, A. Heller, *J. Am. Chem. Soc.* **1991**, *95*, 5261.

[13] X. Guo, N. Chen, C. Feng, Y. Yang, B. Zhang, G. Wang, Z. Zhang, *CATCOM* **2013**, *38*, 26.

[14] G. Li, L. Mao, *RSC Adv.* **2012**, *2*, 5108.

[15] H. Yan, H. Yang, *J. Alloys Compd.* **2011**, *509*, L26.

[16] G. P. and B. N. M. Taramasso, *United StateS Patent*, **1983**.

[17] C. M. a Parlett, K. Wilson, A. F. Lee, *Chem. Soc. Rev.* **2013**, *42*, 3876.

[18] K.-M. Choi, T. Yokoi, T. Tatsumi, K. Kuroda, *J. Mater. Chem. A* **2013**, *1*, 2485.

[19] M. Selvaraj, *Catal. Sci. Technol.* **2014**, *4*, 2674.

[20] Y. Q. Zhang, W. Zhou, S. Liu, A. Navrotsky, *Chem. Mater.* **2011**, *23*, 1166.

[21] T.-D. Nguyen-Phan, E. W. Shin, V. H. Pham, H. Kweon, S. Kim, E. J. Kim, J. S. Chung, *J. Mater. Chem.* **2012**, *22*, 20504.

[22] H. Yan, X. Zhang, S. Zhou, X. Xie, Y. Luo, Y. Yu, *J. Alloys Compd.* **2011**, *509*, L232.

[23] J. Yu, S. Wang, J. Low, W. Xiao, *Phys. Chem. Chem. Phys.* **2013**, *15*, 16883.

[24] X. Bai, L. Wang, R. Zong, Y. Zhu, *J. Phys. Chem. C* **2013**, *117*, 9952.

[25] T. Li, L. Zhao, Y. He, J. Cai, M. Luo, J. Lin, *Appl. Catal. B Environ.* **2013**, *129*, 255.

[26] C. Miranda, H. Mansilla, J. Yáñez, S. Obregón, G. Colón, *J. Photochem. Photobiol. A Chem.* **2013**, *253*, 16.

[27] S. Kumar, T. Surendar, A. Baruah, V. Shanker, *J. Mater. Chem. A* **2013**, *1*, 5333.

[28] F. Dong, Z. Zhao, T. Xiong, Z. Ni, W. Zhang, Y. Sun, W. K. Ho, *ACS Appl. Mater. Interfaces* **2013**, *5*, 11392.

[29] S. K. Choi, S. Kim, S. K. Lim, H. Park, *J. Phys. Chem. C* **2010**, *114*, 16475.

[30] H. Qin, W. Li, Y. Xia, T. He, *ACS Appl. Mater. Interfaces* **2011**, *3*, 3152.

[31] R. Hao, G. Wang, H. Tang, L. Sun, C. Xu, D. Han, *Appl. Catal. B Environ.* **2016**,

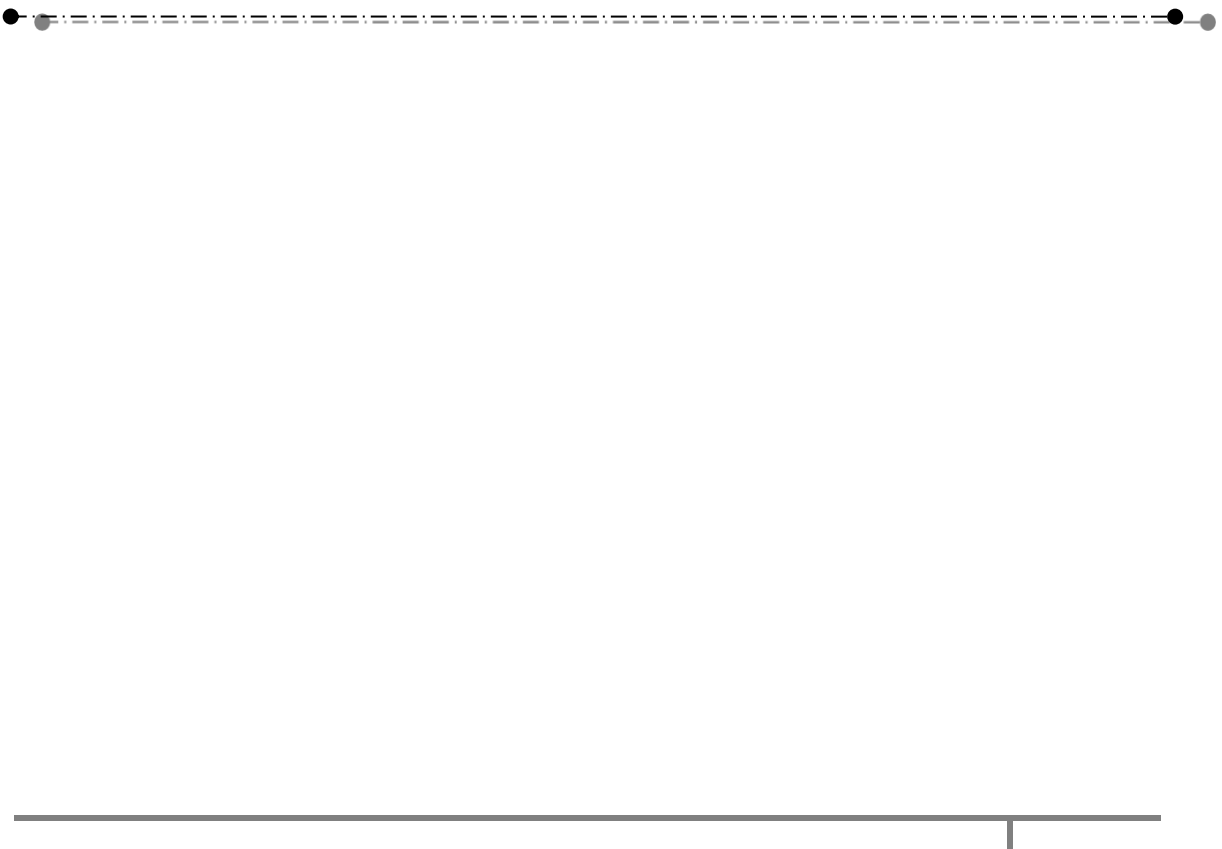


187, 47.

- [32] L. Wang, H. Ji, S. Wang, L. Kong, X. Jiang, G. Yang, *Nanoscale* **2013**, *5*, 3793.
- [33] G. Zhang, J. Zhang, M. Zhang, X. Wang, *J. Mater. Chem.* **2012**, *22*, 8083.
- [34] X. Li, J. Zhang, L. Shen, Y. Ma, W. Lei, Q. Cui, G. Zou, *Appl. Phys. A* **2009**, *94*, 387.
- [35] J. Xie, K. Chen, H. Lee, C. Xu, A. R. Hsu, S. Peng, X. Chen, S. Sun, *J. Am. Chem. Soc.* **2008**, *130*, 7542.
- [36] J. Sudhakareddy, K. R, *J. Catal.* **1991**, *130*, 440.
- [37] D. J. Martin, K. Qiu, S. A. Shevlin, A. D. Handoko, X. Chen, Z. Guo, J. Tang, *Angew. Chemie Int. Ed.* **2014**, *53*, 9240.
- [38] D. Fu, G. Han, F. Liu, Y. Xiao, H. Wang, R. Liu, C. Liu, *Mater. Sci. Semicond. Process.* **2014**, *27*, 966.

## CHAPTER V

**Synthesis and Characterization of porous  
Titanosilicate/Vanadium pentoxide  
nanocomposites and their applications for  
the degradation of methylene blue under  
sunlight irradiation**



## 5 Synthesis and Characterization of porous Titanosilicate/Vanadium pentoxide nanocomposites and their applications for the degradation of methylene blue under sunlight irradiation

### 5.1 Introduction

In recent years, semiconductor as photocatalysis is the most exciting multidisciplinary research area in the field of materials, energy, and environmental technology because of the potential use of this technology in the degradation of organic pollutants, hydrogen production by splitting of water, and the conversion of carbon dioxide into hydrocarbons by using light energy.<sup>[1-5]</sup> These applications play a significant role in resolving present environmental problems and the energy crisis. In semiconductor photocatalysis, photocatalyst absorbs light energy, which is equal to or greater than the band gap of the photocatalyst. In this phenomenon electron and hole pairs are generated, and migrate to the surface of the photocatalyst where the oxidation and reduction reactions occur.<sup>[6-9]</sup> In general, most photocatalysts are still limited to electron-hole pair generation due to absorbing only UV light, very inefficient in absorbing photons and high recombination of electron-hole pairs. To overcome these problems, several efforts have been made to improve the performance of photocatalysts such as metal doping, another semiconductor doping and loading co-catalyst.<sup>[7,10-12]</sup> Therefore, development of an efficient and recyclable visible light driven photocatalysts are the current need.

Vanadium pentoxide ( $V_2O_5$ ), has been broadly exploited for various applications such as, catalysts, actuators, sensors, photocatalysis, UV-driven reversible switch and lithium ion electrode materials.<sup>[13-17]</sup> In recent times,  $V_2O_5$  crystallite has been applied as a photocatalyst. H.L. Fei et al synthesized  $V_2O_5$  hollow spheres via the solvo-thermal method and then obtained hollow spheres were calcined.<sup>[16]</sup> The result shows that  $V_2O_5$  hollow spheres revealed the excellent photodegradation of RhB under UV-light irradiation. J.H. Liu et al. synthesized  $V_2O_5$ /Titania nanocomposite photocatalysts via a binary sol-gel method and in-situ intercalation method and confirmed that  $V_2O_5$  crystallites on the surface of titania could efficiently improve the photocatalytic performance of  $V_2O_5$ /titania in the MB degradation under UV light region.<sup>[17]</sup>

$V_2O_5$  photocatalyst, has been studied widely owing to its strong oxidizing power and long-term stability against photochemical decay and chemical inertness.<sup>[18-21]</sup>

However, the  $V_2O_5$  experimental application is limited and the structure of well-defined  $g\text{-}C_3N_4/V_2O_5$  heterostructures has been showed to be useful for the parting and carrying of photogenerated carriers, and thus subsequent in the improvement of the visible-light-driven photocatalyst.<sup>[22]</sup>

Porous titanosilicate (TS) is a semiconductor it has similar energy band gap of titanium dioxide. Porous titanosilicate successfully synthesized using the template by hydrothermal method.<sup>[23]</sup> Titanosilicate has been an initiate to be able to catalyze the aromatic oxidations, olefins and alcohols using hydrogen peroxide.<sup>[24–27]</sup> The titanosilicate also suitable for photodegradation experiments while it is combined with other material and the titanosilicate showed diverse photochemical assets.<sup>[28–32]</sup> Thuy-Duong Nguyen-Phan *et al* has been reported MB dye removal from water under UV light Irradiation using Titanosilicate/reduced graphene oxide composites.<sup>10</sup>

In current work, synthesized a sequence of porous Titanosilicate-Vanadium pentoxide (VTS) hybrid nanocomposites. The VTS hybrid nanocomposites physicochemical properties were characterized by PXRD, UV–Visible DRS, FTIR, and morphological structures investigated by FE-SEM EDX, HR-TEM. Based on practical results, a proposed mechanism is discussed for improved visible light photocatalysis. The as-synthesized VTS hybrid nanocomposites showed a broader absorption in visible light area than pure TS and  $V_2O_5$  showed enhanced MB degradation under sunlight irradiation.

## 5.2 Experimental details

### 5.2.1 Materials

Tetraethyl orthosilicate (TEOS, 98.0%, Sigma-Aldrich) and Titanium isopropoxide (TTIP, 97.0%, Sigma-Aldrich). Tetrahydrofuran (THF, 98.0%, SD fine), Oxalic acid (OA, 99.0%, SD fine), Ammonium vanadate ( $NH_4VO_3$ , 98.0%, SD fine), Cetyltrimethyl ammoniumbromide (CTAB, 98.0%, SD fine) and ammonia solution (25%, SD fine).

### 5.2.2 Method

#### 5.2.2.1 Preparation of highly porous Titanosilicate (TS)

Porous Titanosilicate was prepared via hydrothermal route. In the synthesis procedure, 0.3 g of CTAB is dissolved in 60 mL of water to form a homogenous solution, and then 1.38 mL of ammonium hydroxide was added. About 0.60 g of TEOS was added

drop wise into this mixture under vigorous stirring, followed by the addition of 0.40 g of TTIP stirring was continued for another 6 h. The mixture was placed into a 100 mL Stainless steel autoclave and heated at 120 °C for 12 h. After the centrifugation Solid product was collected and dried at 80 °C for 12 h. The obtained product was collected after the calcination at 550 °C for 5 h.

#### 5.2.2.2 Preparation of pure V<sub>2</sub>O<sub>5</sub> nanoparticles

In a brief procedure, 0.01 mol OA was added in the mixture of 25 mL deionized water and 5 mL Tetrahydrofuran, and then 0.005 mol NH<sub>4</sub>VO<sub>3</sub> was added into the mixture under stirring for 2 h at RT. The reaction mixture was shifted into a 250-mL Teflon-lined autoclave at 180°C for 24 h. The precursor was filtered, washed with deionized water and ethanol, and dried at 60 °C for 12 h. The obtained product was collected after the calcintion at 500 °C for 2 h.

#### 5.2.2.3 Preparation of VTS inorganic hybrid nanocomposite

In the synthesis procedure, above synthesized V<sub>2</sub>O<sub>5</sub> and TS were added to 50mL of methanol in a beaker and ultrasonicated for 45 min. The nanocomposites were collected after the evaporation of methanol at 80 °C.<sup>11</sup> The VTS hybrid nanocomposites VTS1 (TS and V<sub>2</sub>O<sub>5</sub> ratio is 2:1), VTS2 (TS and V<sub>2</sub>O<sub>5</sub> ratio is 1:1), VTS3 (TS and V<sub>2</sub>O<sub>5</sub> ratio is 1:2) were prepared.

### 5.2.3 Photocatalytic activity

The photocatalytic performance of the VTS nanocomposites were evaluated by the MB degradation under sunlight irradiation. 50 mg of VTS photocatalyst was added into 100 mL of MB solution (10<sup>-4</sup> M). To reach the adsorption equilibrium, experiment was carriedout in dark condition for 30 min. During the photocatalytic experiment, the solution was collected from time to time, the photocatalyst separated from the solution by centrifugation. The collected samples absorbance were verified by using Thermo fisher UV-visible spectrophotometer. 150 W tungsten visible lamp used for visible light. The wave length range is 400 to 800 nm.

### 5.3 Results and discussion

#### 5.3.1 Powder X-ray Diffraction Analysis

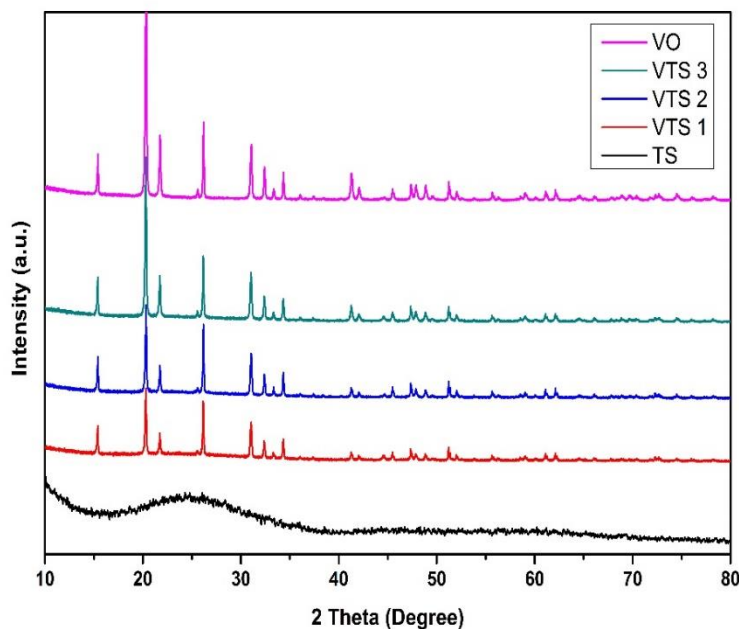


**Figure 5.1:** PXRD spectra of pure TS, pure VO, VTS1, VTS2 and VTS3 nanocomposites

The figure 5.1 shows, PXRD spectra of pure VO, pure TS, VTS1, VTS2 and VTS3 hybrid nanocomposites. For VO, the strong peaks were detected at  $2\theta$  of 15.46, 20.36, 21.8, 25.56, 26.22, 31.10, 32.42, 33.40, 34.41, 36.16, 37.48 and 41.36. According to the literature JCPDS-41-1426 data, the  $2\theta$  values were resembled with the orthorhombic crystal structure of VO with cell dimensions of  $11.516 \times 3.5656 \times 4.3727$ . The high crystallinity and good arrangement crystal lattice of VO due to the noise free, sharp peaks.<sup>12</sup> A broad peak centered at  $23^\circ$  was ascribed to the mesoporous TS. The impurity peaks of no other phases were found.<sup>13</sup> Due to high intensity peaks of VO at the same  $2\theta$  value of TS, porous TS peak unable to found by PXRD pattern for the VTS nanocomposites.

### 5.3.2 Morphology Characterization

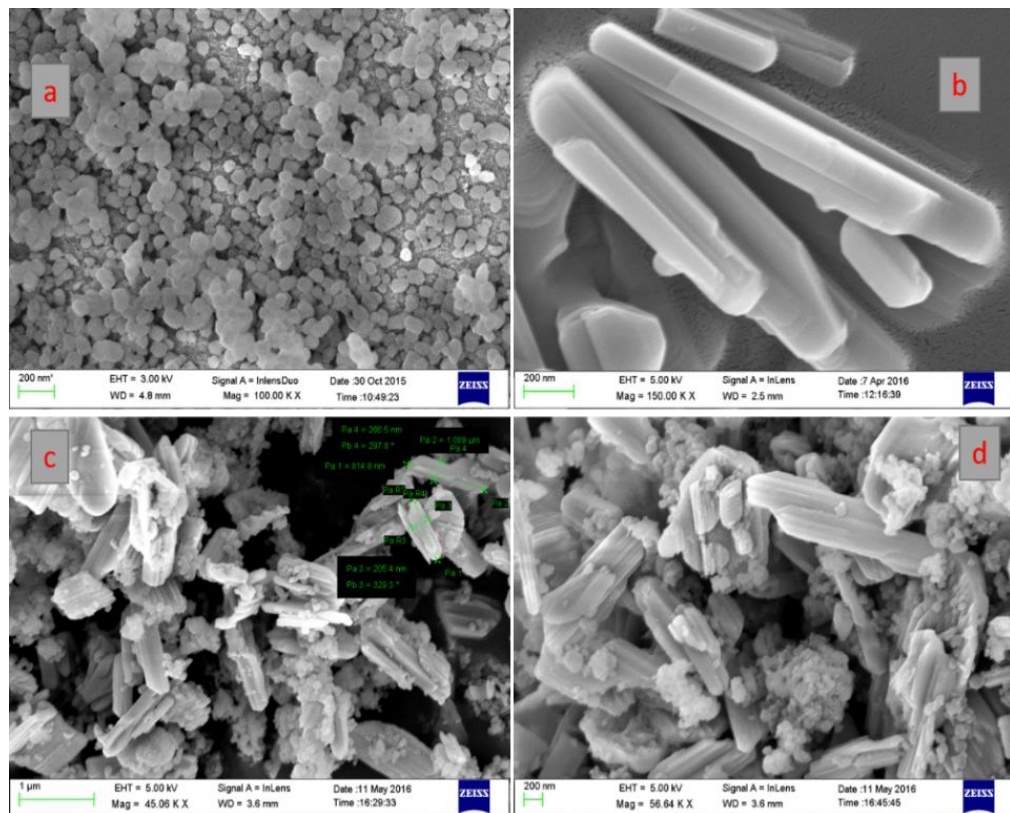
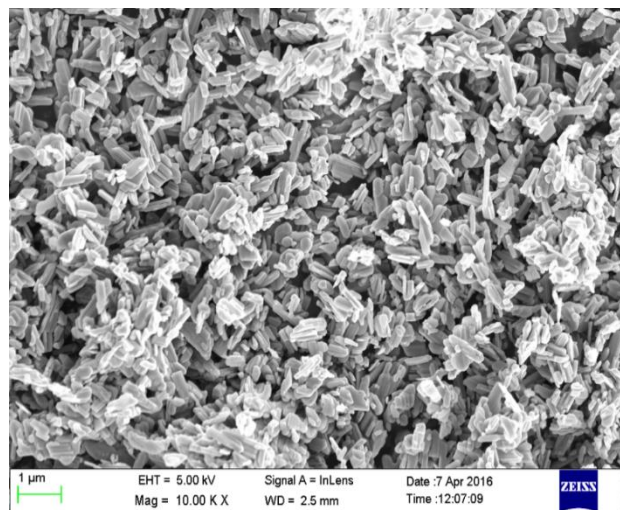


**Figure 5.2:** FE-SEM images of a) pure TS, b) pure VO nanorods and c&d) VTS1 hybrid nanocomposite

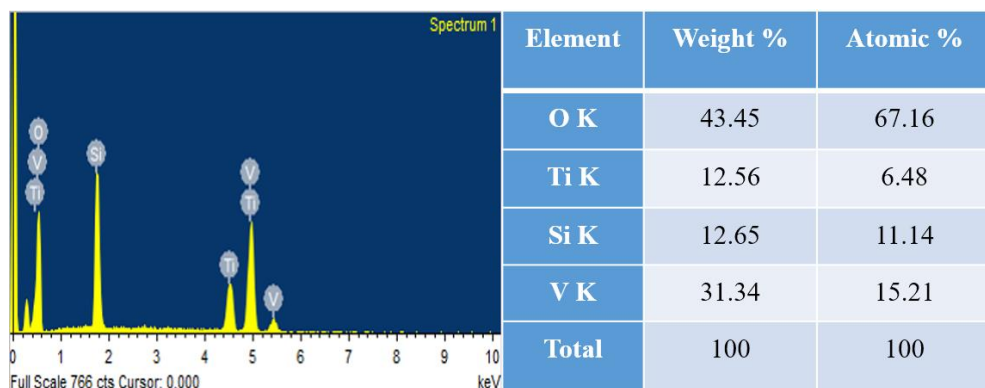
The morphological structures of pure TS, pure VO and VTS nanocomposites were studied by FE-SEM analysis as shown in figure 5.2. Figure 5.2 (a&e) shows the image of pure TS with uniform distribution of spherical shaped particles. Figure 5.2b represents the nanorod like structures of the pure VO and the average grain size was found to be 318 nm. Figure 5.2 (c&d) shows VTS1 nanocomposite, which clearly emphasis the successful distribution of TS particles on the VO nanorods. The tightly packed surface morphology of the composite particles is beneficial for the efficient charge carrier separation. Figure 5.3 shown EDS analysis of VTS1, which contains following elements composition like V, O, Ti, Si and the elemental mapping of VTS1 was shown in figure 5.4.

Figure 5.5 represents TEM images of the pure TS, VTS1 hybridnanocomposite. Figure 5.5 (a&b) shows the morphology of pure TS which contains hexagonal porous like structure. The figure 5.5 (c-e) represents TEM and HR-TEM images of VTS1 hybrid nanocomposite, which clearly reveals that a good heterojunction was formed between the

TS and VO nanorods. Figure 5.5f shows the selected area electron diffraction (SAED) of VTS nanocomposite. FE-SEM image of the  $V_2O_5$  nanoparticles. Average particle size is 400 nm.



**Figure 5.2e:** FE-SEM image of pure  $V_2O_5$  nanorods



**Figure 5.3:** EDS Analysis of VTS1 nanocomposite

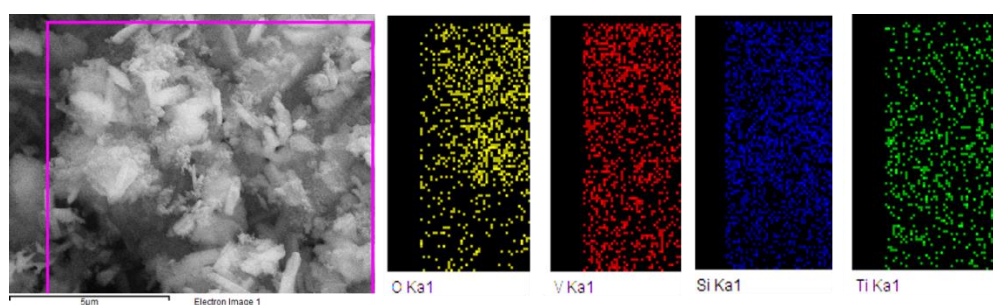


**Figure 5.4:** Elemental mapping of respective elements of VTS1 nanocomposite

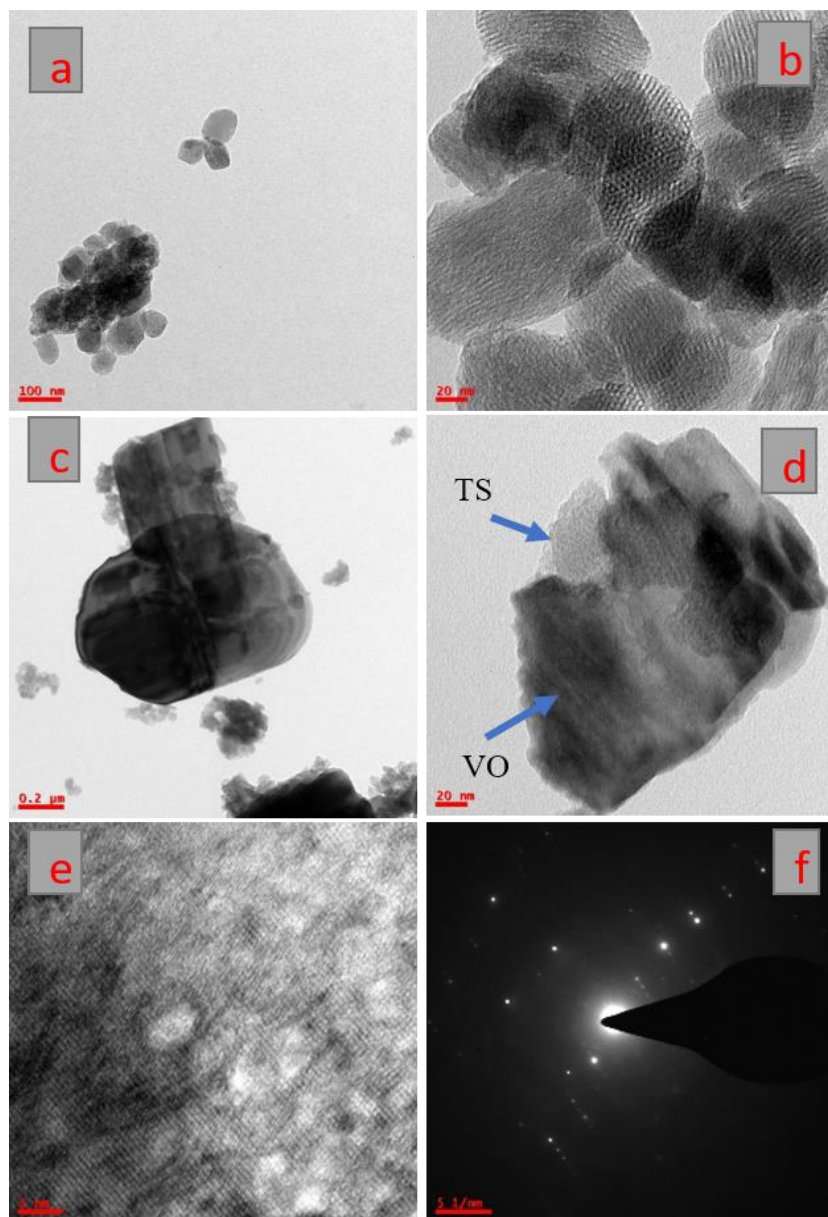


**Figure 5.5:** TEM images of a&b) pure TS, b&c) VTS1nanocomposite, e) HR-TEM of VTS1 nanocomposite and f) SAED pattern of VTS1 nanocomposite

### 5.3.3 FTIR Analysis

Figure 5.6 shows FT-IR spectra of the prepared pure TS, pure VO, VTS1, VTS2 and VTS3 nanocomposites. In the TS, Si-O-Si band 1100, 802 and 467  $\text{cm}^{-1}$  strong peaks of which indicates the condensation of silicon alkoxide. It was shown that the 960  $\text{cm}^{-1}$  band is Ti-O- peak of TS. Thangaraj *et al.* have verified that the 960  $\text{cm}^{-1}$  band shown by TS zeolites can also be ascribed to a stretching mode of a  $[\text{SiO}_4]$  unit bonded to a  $\text{Ti}^{+4}$  ion

[O<sub>3</sub>SiOTi]. In V<sub>2</sub>O<sub>5</sub>, 829 cm<sup>-1</sup> and 1018 cm<sup>-1</sup> two characteristic absorption bands were observed.<sup>14</sup> The V-O-V band at 829 cm<sup>-1</sup> is ascribed to the asymmetric stretching vibration and the other V-O band at 1018 cm<sup>-1</sup> is ascribed to the stretching vibration.<sup>15</sup> In VTS nanocomposites represent the overlap of TS and VO. All the FT-IR spectra of the composites exhibit the characteristic bands of both TS and VO, and no impurity band was detected.

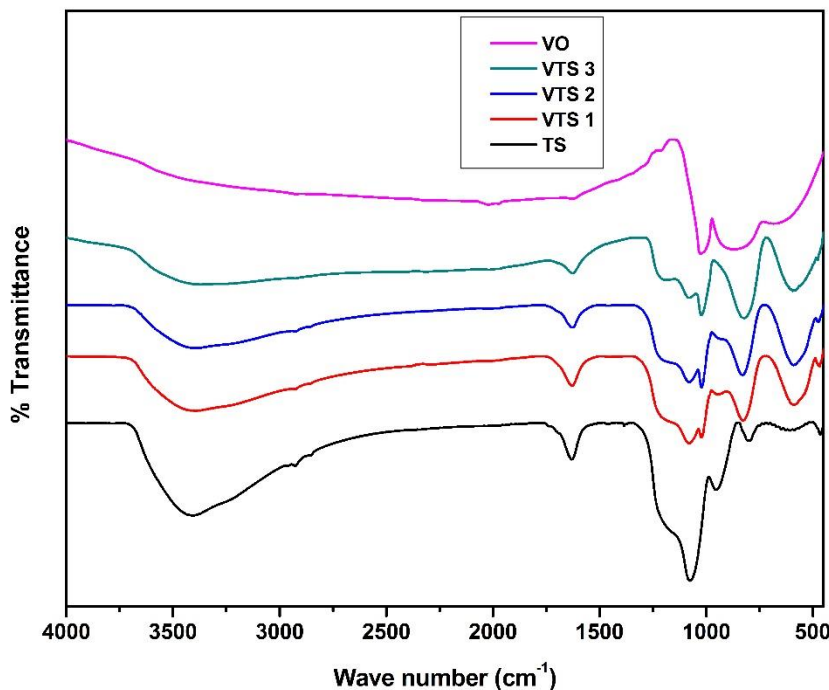
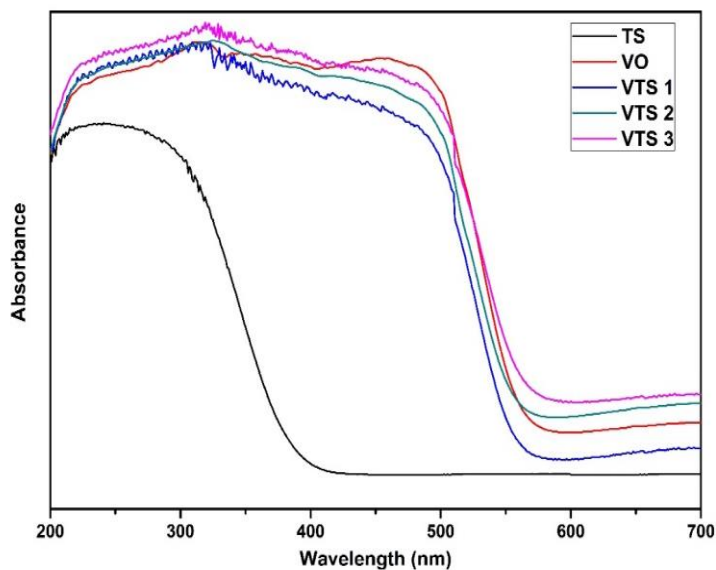


**Figure 5.6:** FTIR Spectra of pure TS, pure VO, VTS1, VTS2 and VTS3 nanocomposites

### 5.3.4 UV-Visible DRS Spectra

The figure 5.7 shows, UV-visible diffuse reflectance spectra of pure TS, pure VO, VTS1, VTS2 and VTS3 nanocomposites. It can be seen that TS and V<sub>2</sub>O<sub>5</sub> absorption edges of around at 390 nm, 530 nm respectively. The absorption edge of VTS nanocomposites were moved to higher wavelength in comparison with TS. This may be attributed to the inorganic hybrid structure between TS and V<sub>2</sub>O<sub>5</sub> interfaces. No obvious difference is observed among the composites, indicating that the content of V<sub>2</sub>O<sub>5</sub> does not influence the light-harvesting property of prepared composites. It is notable that the VTS nanocomposites also exhibit a broad background absorption in the visible light region, which could be attributed to the presence of V<sub>2</sub>O<sub>5</sub> nanoparticles. The results also show that

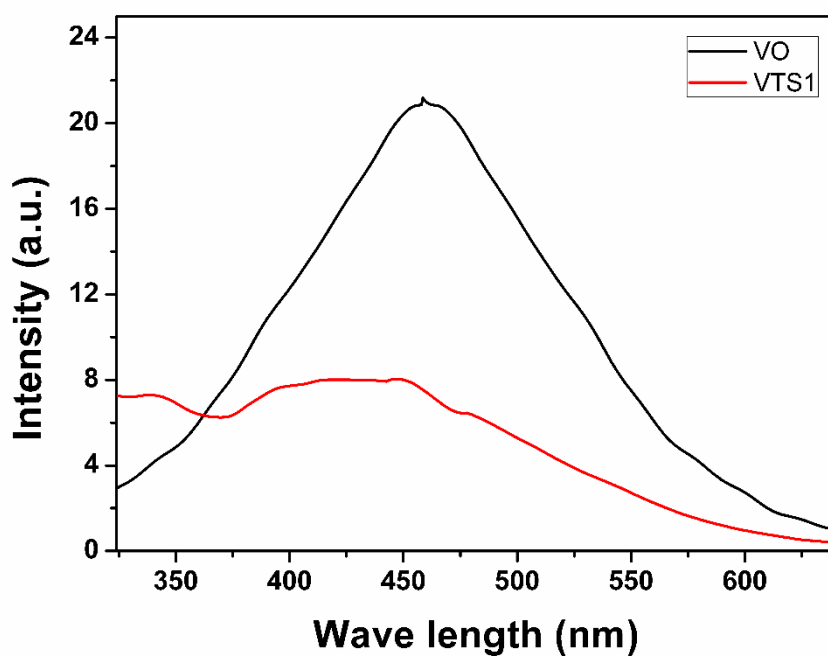
all VTS nanocomposites are able to function under visible light illumination. The band gaps of TS and V<sub>2</sub>O<sub>5</sub> are expected to be 3.1 and 2.30 eV, respectively.<sup>16</sup>



**Figure 5.7:** UV-Visible DRS Spectra of pure TS, pure VO, VTS1, VTS2 and VTS3 nanocomposites

### 5.3.5 Photoluminescence

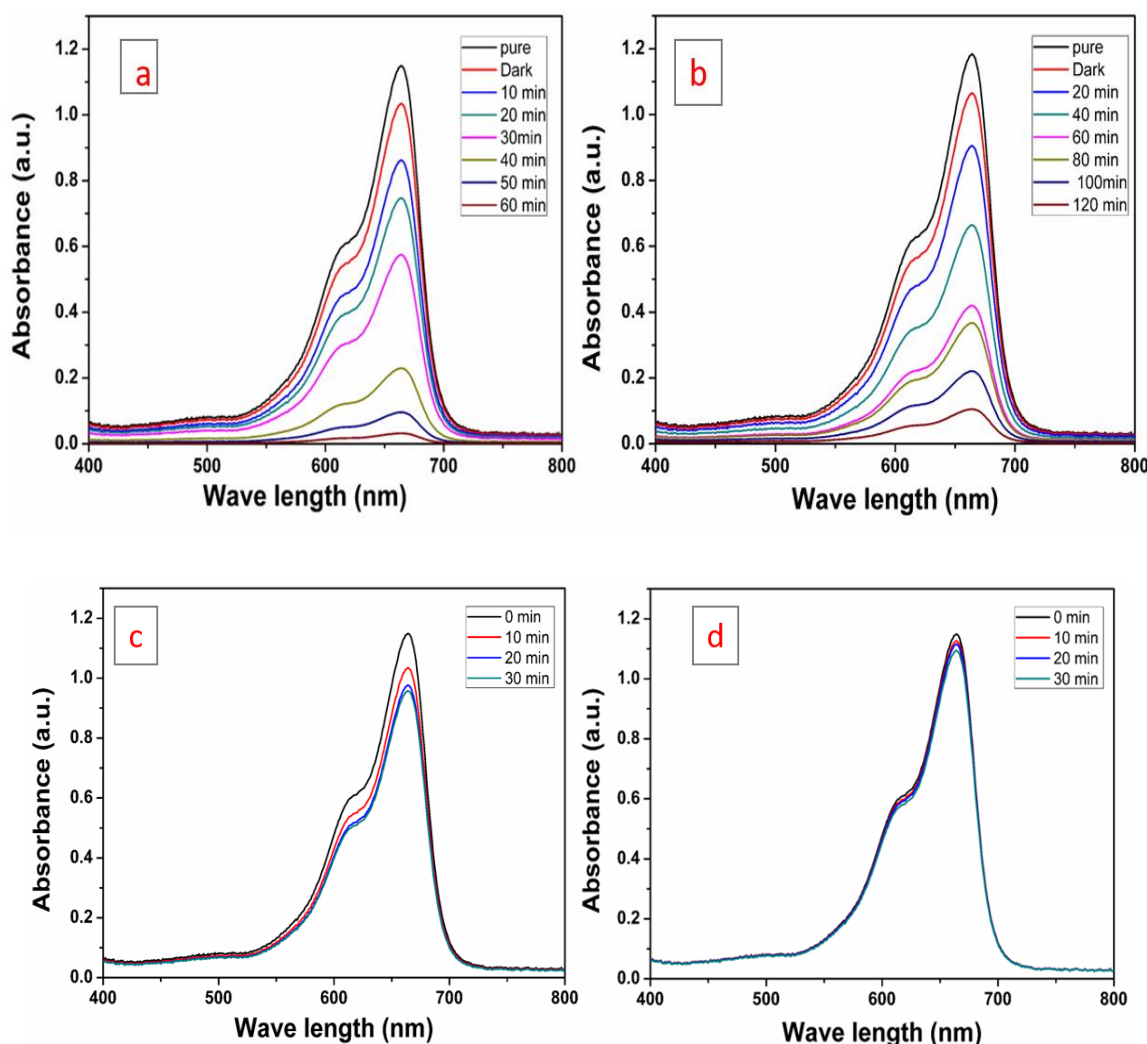
To further confirm the separation mechanism of electron-hole pairs in VTS1 hybrid nanocomposite as discussed above, the room temperature PL properties of the as-prepared pure VO and VTS1 hybrid nanocomposite were investigated as shown in figure 5.8. The PL spectra of pure VO and VTS1 hybrid nanocomposite were obtained at an excitation wavelength of 325 nm. As shown in figure 5.8, an emission at about 546 nm was obviously detected in both pure VO and VTS1 hybrid nanocomposite. However, the fluorescence intensity of VTS1 hybrid nanocomposite (red line) was weaker than that of pure VO (black line), clearly demonstrating that the recombination of photogenerated electron-hole pairs was inhibited greatly in VTS1 hybrid nanocomposite. This result is good agreement with the analysis by the energy band position of VO and TS, as discussed above. Thus, the PL spectra offer direct evidence for the efficient separation of photogenerated electron-hole pairs in VTS1 hybrid nanocomposite, leading to enhanced photocatalytic degradation of MB, compared to pure VO and pure TS.



**Figure 5.8:** Photoluminescence spectra of pure VO and VTS1 Hybrid nanocomposite

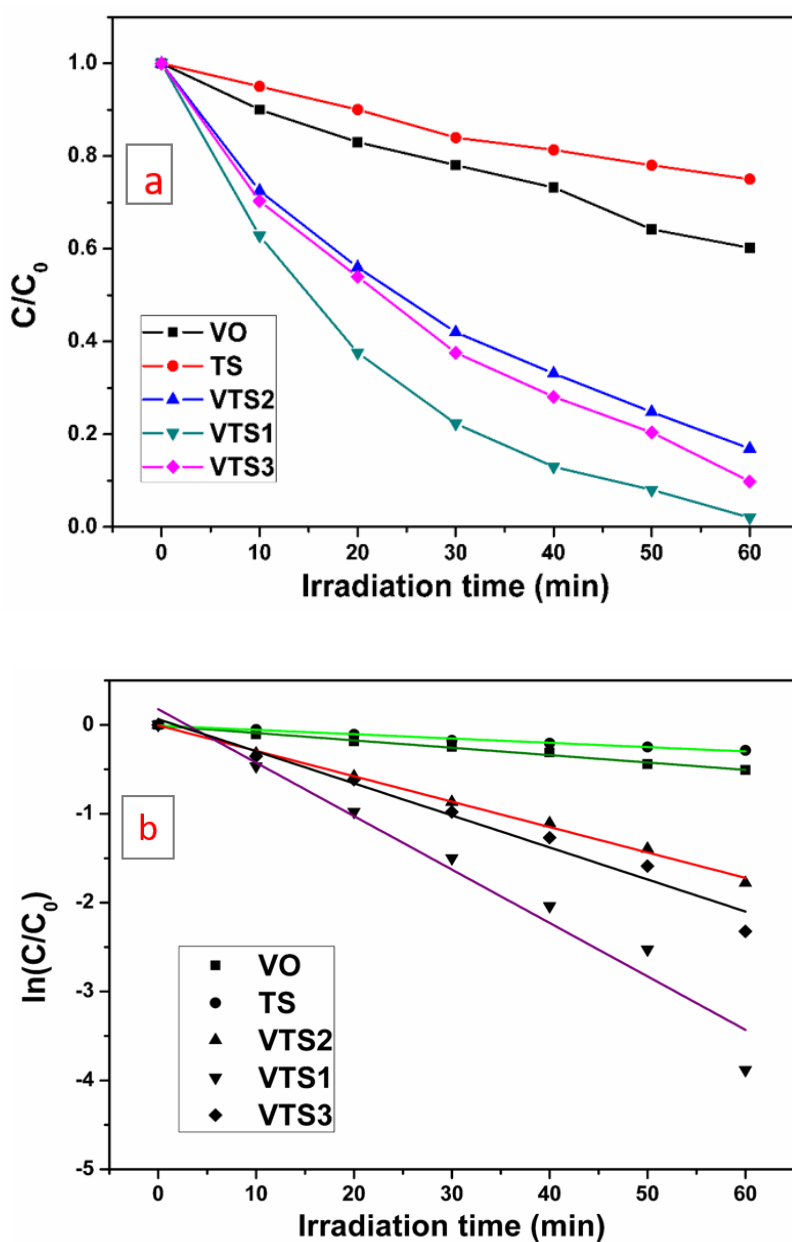
#### 5.4 Photocatalytic activity

Figure 5.9 shows the photocatalytic performance of the synthesized VTS nanocomposite was analyzed using MB dye under direct sunlight, visible light irradiations and effect of catalyst adsorption, photolysis capacity. MB shows a maximum absorbance at 655 nm. Figure 5.9a shows the sunlight irradiation at different time intervals and the MB dye degradation rate was observed. The degradation of MB dye solution with VTS nanocomposite under irradiation of visible light for different time intervals as shown in figure 5.9b. This result shows that sunlight irradiated MB dye with VTS nanocomposite solution was degraded quickly within 60 min compared to visible light irradiation. Figure 5.9c shows the effect of catalyst adsorption of MB dye solution with VTS nanocomposite under dark conditions with different time intervals. Figure 5.9d The MB dye under sunlight (30 min) without a catalyst to check the photolysis of the MB dye. To demonstrate the influence of TS on the VO nanorods, the MB degradation was studied under sunlight.



**Figure 5.9:** Photodegradation of MB dye under the irradiation of (a) direct sunlight, (b) visible light, (c) catalyst adsorption for the VTS nanocomposites and (d) photolysis of MB

The photocatalytic activity of VTS nanocomposites was calculated in terms of the photocatalytic MB degradation under sunlight irradiation. The figure 5.10 shows the absorption spectra of MB solution under direct sunlight irradiation for different time intervals. The dye degrades at a faster rate under sunlight (60 min). The MB concentrations were recorded on Thermo fisher UV-visible spectrophotometer.



**Figure 5.10:** Photodegradation of MB dye under the irradiation of direct sunlight with pure TS, pure VO, VTS1, VTS2 and VTS3 nanocomposites

The figure 5.10a Shown, the  $C/C_0$  vs irradiation time for VTS nanocomposites, pure TS and Pure VO. Where the MB solution initial concentration is  $C_0$  and MB solution concentration  $C$  with respect to the degradation time 't'. It is observable from the figure 5.10b, the degradation rate was quite faster in the composite compared to pure VO, which shows the beneficial impact of titanosilicate on the photocatalytic performance of the composite.

## 5.5 Photocatalytic mechanism

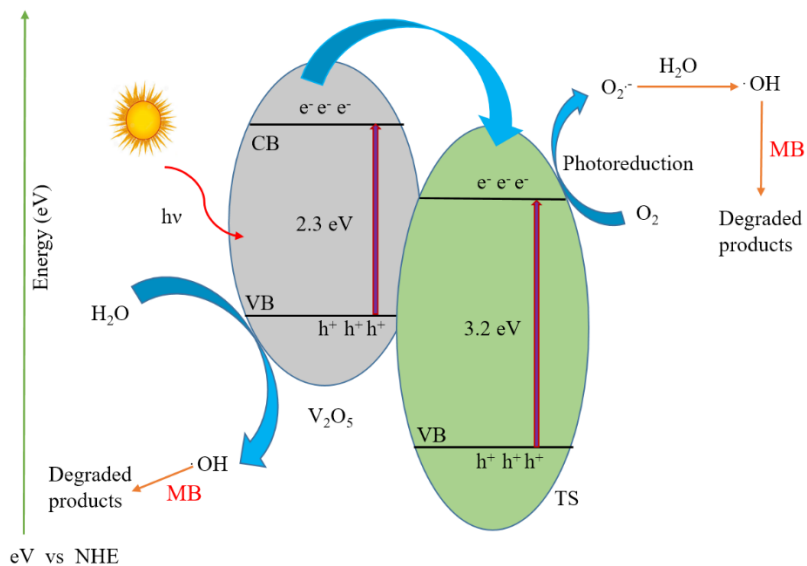


**Figure 5.11:** Schematic illustration of the photocatalytic degradation mechanism of MB over VTS hybrid nanocomposite under sunlight irradiation

The energy band diagram of the Titanosilicate/V<sub>2</sub>O<sub>5</sub> heterostructure photocatalyst after the thermodynamic equilibrium was presented in figure 5.11. The calculated conduction band (CB) and valence band (VB) of TS is -0.3 and 2.86 eV, whereas CB and VB of BiVO<sub>4</sub> are 0.44 and 2.64 eV, respectively. V<sub>2</sub>O<sub>5</sub> is considered as an intrinsic semiconductor, so the Fermi level in V<sub>2</sub>O<sub>5</sub> lies in the middle of the conduction band and valence band, which is approximately equal to 1.6 eV. According to the literature survey band energy level of V<sub>2</sub>O<sub>5</sub>, E<sub>C</sub> and E<sub>V</sub> increase from 0.4 eV to -1.2 eV, 2.8 eV to 1.1 eV respectively<sup>[33]</sup>. Obviously, the difference of E<sub>CB</sub> between V<sub>2</sub>O<sub>5</sub> and TS allowed the transfer of an electron from the conduction band of V<sub>2</sub>O<sub>5</sub> to that of TS. When the system is irradiated with visible light, an electron (e<sup>-</sup>) is promoted from the valence band into the conduction band of V<sub>2</sub>O<sub>5</sub> leaving a hole (h<sup>+</sup>) behind. Then the excited-state electrons produced by V<sub>2</sub>O<sub>5</sub> can be injected into the conduction band of the coupled TS due to the joint of the electric fields between two materials. The conduction electrons are good reductants which could capture the adsorbed O<sub>2</sub> on the surface of the catalyst and reduce it to O<sub>2</sub><sup>·-</sup>. It can be further dissociated or reduced by photoinduced electrons, so there would be a constant stream of the surface 'OH groups to come into being. In the presence of hydroxyl radicals, the efficiently photocatalytic degradation of MB can be carried out smoothly. In addition, the photogenerated hole in

$\text{V}_2\text{O}_5$  also may activate some unsaturated organic pollutants, resulting in subsequent decomposition.

## 5.6 References

- [1] A. Mills, S. Le Hunte, *J. Photochem. Photobiol. A Chem.* **1997**, *108*, 1–35.
- [2] Z. Yi, J. Ye, N. Kikugawa, T. Kako, S. Ouyang, H. Stuart-Williams, H. Yang, J. Cao, W. Luo, Z. Li, et al., *Nat. Mater.* **2010**, *9*, 559–564.
- [3] A. Fujishima, X. Zhang, D. Tryk, *Int. J. Hydrogen Energy* **2007**, *32*, 2664–2672.
- [4] D. Bahnemann, *Sol. Energy* **2004**, *77*, 445–459.
- [5] M. R. Hoffmann, S. T. Martin, W. Choi, D. W. Bahnemann, *Chem. Rev.* **1995**, *95*, 69–96.
- [6] D. Chatterjee, S. Dasgupta, *J. Photochem. Photobiol. C Photochem. Rev.* **2005**, *6*, 186–205.
- [7] Y. Li, J. Wang, H. Yao, L. Dang, Z. Li, *J. Mol. Catal. A Chem.* **2011**, *334*, 116–122.
- [8] M. Litter, *Appl. Catal. B Environ.* **1999**, *23*, 89–114.
- [9] K. Pirkanniemi, M. Sillanpää, *Chemosphere* **2002**, *48*, 1047–1060.
- [10] D. Ljubas, *Energy* **2005**, *30*, 1699–1710.
- [11] J. M. Herrmann, *Top. Catal.* **2005**, *34*, 49–65.
- [12] Y. Liang, H. Wang, H. Sanchez Casalongue, Z. Chen, H. Dai, *Nano Res.* **2010**, *3*, 701–705.
- [13] R. T. Rajendra Kumar, B. Karunagaran, D. Mangalaraj, S. K. Narayandass, P. Manoravi, M. Joseph, V. Gopal, *Sensors Actuators A Phys.* **2003**, *107*, 62–67.
- [14] J. Liu, X. Wang, Q. Peng, Y. Li, *Adv. Mater.* **2005**, *17*, 764–767.
- [15] Y. Wang, K. Takahashi, K. H. Lee, G. Z. Cao, *Adv. Funct. Mater.* **2006**, *16*, 1133–1144.
- [16] H.-L. Fei, H.-J. Zhou, J.-G. Wang, P.-C. Sun, D.-T. Ding, T.-H. Chen, *Solid State Sci.* **2008**, *10*, 1276–1284.
- [17] J. LIU, R. YANG, S. LI, *Rare Met.* **2006**, *25*, 636–642.
- [18] J. Sun, X. Li, Q. Zhao, J. Ke, D. Zhang, *J. Phys. Chem. C* **2014**, *118*, 10113–10121.
- [19] M. G. Kim, H. Kim, J. Cho, *J. Electrochem. Soc.* **2010**, *157*, A802.
- [20] Y. Li, S. Ji, Y. Gao, H. Luo, M. Kanehira, *Sci. Rep.* **2013**, *3*, 1370.

[21] Y. N. Ko, Y. C. Kang, S. Bin Park, *Chem. Commun.* **2013**, *49*, 3884.

[22] T. Jayaraman, S. Arumugam Raja, A. Priya, M. Jagannathan, M. Ashokkumar, *New J. Chem.* **2015**, *39*, 1367–1374.

[23] G. P. and B. N. M. Taramasso, *United StateS Patent*, **1983**.

[24] F. X. Llabrés i Xamena, P. Calza, C. Lamberti, C. Prestipino, A. Damin, S. Bordiga, E. Pelizzetti, A. Zecchina, *J. Am. Chem. Soc.* **2003**, *125*, 2264–2271.

[25] C. M. a Parlett, K. Wilson, A. F. Lee, *Chem. Soc. Rev.* **2013**, *42*, 3876–3893.

[26] K.-M. Choi, T. Yokoi, T. Tatsumi, K. Kuroda, *J. Mater. Chem. A* **2013**, *1*, 2485.

[27] M. Selvaraj, *Catal. Sci. Technol.* **2014**, *4*, 2674.

[28] M. Moliner, A. Corma, *Microporous Mesoporous Mater.* **2014**, *189*, 31–40.

[29] S. Uma, S. Rodrigues, I. N. Martyanov, K. J. Klabunde, *Microporous Mesoporous Mater.* **2004**, *67*, 181–187.

[30] S. K. Das, M. K. Bhunia, A. Bhaumik, *J. Solid State Chem.* **2010**, *183*, 1326–1333.

[31] S. Anandan, *Dye. Pigment.* **2008**, *76*, 535–541.

[32] Y. Q. Zhang, W. Zhou, S. Liu, A. Navrotsky, *Chem. Mater.* **2011**, *23*, 1166–1173.

[33] Y. Hu, D. Li, Y. Zheng, W. Chen, Y. He, Y. Shao, X. Fu, G. Xiao, *Appl. Catal. B Environ.* **2011**, *104*, 30–36.

## CHAPTER VI

Photocatalytic degradation of Rhodamine B  
under direct sunlight irradiation using  
porous Titanosilicate/Bismuth Vanadate  
hybrid nanocomposites



## 6 Photocatalytic degradation of Rhodamine B under direct sunlight irradiation using porous Titanosilicate/Bismuth Vanadate hybrid nanocomposites

### 6.1 Introduction

Organic dyes in fabric and other industrial discharges have become one of the main environmental pollutants. As many dyes are highly water-soluble, outdated treatment procedures including flocculation, activated carbon adsorption, and biological treatment do not work proficiently. Lately, photocatalysis process has played a vital role in the degradation of organic dyes in wastewater.<sup>[1,2]</sup> Related with other procedures, photocatalysis has numerous benefits, such as the usage of eco-friendly oxidant O<sub>2</sub>, complete mineralization, no waste disposal problem, and a necessity of only mild temperature and pressure conditions.<sup>[3-6]</sup> Moreover, the photocatalysis is able to work out even at a much lesser concentration of organic dyes. Therefore, photocatalysis is a promising solution to organic dyes. Early studies on photocatalysts mainly focused on the Ultraviolet-driven TiO<sub>2</sub> photocatalyst.<sup>[7,8]</sup> However, UV light takes up only ca. 4% of the solar energy while visible-light ca. 43%. Hereby, visible-light-driven photocatalysts have been the new focus.<sup>[9]</sup>

Our research group is working on photocatalytic studies of Titanosilicate (TS), which is completely used in the past as the catalyst in cyclohexanone ammoximation for its extremely high catalytic activity and selectivity.<sup>[10-12]</sup> Porous Titanosilicate material has been found to be able to catalyze the oxidation of aromatics, olefins and alcohols with hydrogen peroxide.<sup>[13-15]</sup> The novel discovery of Titanosilicate also beneficial for photodegradation experiments while the material is composite with other. In each reaction, the Titanosilicate shows different physicochemical properties. From the photocatalysis point of view, NO photocatalytic decomposition has been reported. Thuy-Duong Nguyen-Phan *et al* reported Mesoporous Titanosilicate/reduced graphene oxide composites doping effect on the application in MB dye removal from waste water.<sup>[16]</sup>

Since BiVO<sub>4</sub> was an initiate to be an active photocatalyst for O<sub>2</sub> growth from the aqueous AgNO<sub>3</sub> solution under visible-light irradiation and more attention has been involved in the synthesis of BiVO<sub>4</sub> photocatalyst under visible-light irradiation.<sup>[17-25]</sup> Among the 3 crystalline phases of BiVO<sub>4</sub>, i.e. tetragonal scheelite (s-t), monoclinic scheelite (s-m) and tetragonal zircon (z-t) structures,<sup>[26]</sup> it is found that the monoclinic

scheelite  $\text{BiVO}_4$  (m- $\text{BiVO}_4$ ) shows much greater photocatalytic performance than the other two tetragonal phases.<sup>[27]</sup> Therefore, several procedures have been employed for the preparation of m- $\text{BiVO}_4$ , such as solution combustion process, ultrasound or microwave-assisted method, aqueous process, flame spray pyrolysis, solid-state reaction, metallorganic decomposition and hydrothermal or solvo-thermal process.<sup>[28-41]</sup> Related to other procedures, the aqueous process delivers a milder atmosphere for the preparation of m- $\text{BiVO}_4$ .

In this report a facile, active preparation of porous Titanosilicate/Bismuth vanadate (BVTS) inorganic hybrid nanocomposites to accomplish the enhanced visible light driven photocatalyst. The novel BVTS inorganic hybrid nanocomposite were characterized by powder X-ray diffraction (PXRD), Field emission scanning electron microscopy (FE-SEM), Energy Dispersive X-Spectroscopy (EDS or EDX), Transmission electron microscopy (TEM), Fourier transform infrared spectroscopy (FTIR) and UV–Visible diffuse reflectance spectroscopy (UV–Vis DRS). Based on our experimental results, we proposed a plausible mechanism and is discussed for enhanced visible light photocatalysis. However, to the best of our knowledge there is no report on the synthesis of BVTS inorganic hybrid nanocomposite photocatalyst.

## 6.2 Experimental Section

Tetraethyl orthosilicate (TEOS, 98.0%, Sigma-Aldrich) and Titanium isopropoxide (TTIP, 97.0%, Sigma-Aldrich), Bismuth nitrate ( $\text{Bi}(\text{NO}_3)_3 \cdot 5\text{H}_2\text{O}$ , 99.0%, Sigma-Aldrich), Rhodamine B (RhB, 95.0%, Sigma-Aldrich). Ammonium vanadate ( $\text{NH}_4\text{VO}_3$ , 98.0%, SD fine), Cetyltrimethyl ammoniumbromide (CTAB, 98.0%, SD fine) and Ammonia Solution (25.0%, SD fine). All aqueous solution were prepared with millipore water.

### 6.2.1 Synthesis of photocatalysts

Porous Titanosilicate was synthesized by hydrothermal method. In a typical procedure, 0.3 g of CTAB is dissolved in 60 ml of Millipore water to form a homogenous solution, 1.38 ml of ammonium hydroxide was added. About 0.60 g of TEOS was added dropwise into this mixture under vigorous stirring, followed by the addition of 0.40 g of TTIP stirring was continued for another 6 h. The reaction mixture was kept in a 100 mL

autoclave and heated at 120 °C for 12 h. The solid products were collected by centrifugation and dried at 80 °C overnight. The obtained product was calcined at 550 °C for 5 h.

In a typical synthesis, 2 mmol of  $\text{NH}_4\text{VO}_3$  was added into 20 mL of de-ionized water at 96 °C. The  $\text{NH}_4\text{VO}_3$  solution was added dropwise into a 250 mL RB having 40 mL of 0.05M CTAB in an oil bath at 60 °C. Afterwards, 2 mmol of  $\text{Bi}(\text{NO}_3)_3 \cdot 5\text{H}_2\text{O}$  was added into 20 mL of de-ionized water and stirred for about 10 min to form a hydrolyzed white floccule. The floccule suspension was added dropwise into the flask at 60 °C under stirring. After that, the flask was connected with a condenser and heated in oil bath at 80 °C for 12 h. The product was centrifuged, washed with water, ethanol and dried in air. The obtained product was calcined at 550 °C for 4 h. The synthesized m- $\text{BiVO}_4$  crystals were reported and denoted as BVO.<sup>[42]</sup>

An appropriate amount of Titanosilicate was suspended in 50 mL of water and ultrasonicated for 1h. The TS solution was added dropwise into a 250 mL round bottom flask containing 40 mL of 0.05 M CTAB solution in an oil bath at 60 °C. Separately 2 mmol of  $\text{NH}_4\text{VO}_3$  was first dissolved into 20 mL of de-ionized water at 96 °C and then the solution was cooled to room temperature. The  $\text{NH}_4\text{VO}_3$  solution was added dropwise into a 250 mL flask containing CTAB, Titanosilicate solutions afterward, 2mmol  $\text{Bi}(\text{NO}_3)_3 \cdot 5\text{H}_2\text{O}$  was added into 20mL of de-ionized water and stirred for about 10 min to form a hydrolyzed white floccule. The floccule suspension was added dropwise into the flask at 60 °C under stirring. After that, the flask was connected with a condenser and heated in oil bath at 80 °C for 12 h. The product was centrifuged, washed with water, ethanol and dried in air. The obtained product was calcined at 550 °C for 4 h. The as-prepared BVTS nanocomposites BVTS1 (TS and  $\text{BiVO}_4$  ratio is 2:1), BVTS2 (TS and  $\text{BiVO}_4$  ratio is 1:1), BVTS3 (TS and  $\text{BiVO}_4$  ratio is 1:2) were prepared and reported. Titanosilicate named as TS and  $\text{BiVO}_4$  named as BVO.

### 6.2.2 Dye photodegradation experiment

Rhodamine B (RhB) shows a maximum absorbance at 553nm which is used to monitor the photocatalytic RhB degradation. The photocatalytic performance of the BVTS nanocompoites were evaluated by the degradation of RhB under sunlight

irradiation. 0.1 g of BPTS photocatalyst was added into 100 mL of RhB solution with a concentration of 5 ppm. Prior to irradiation, solutions suspended with photocatalysts were stirred in dark condition for 30 min to ensure that the adsorption-desorption equilibrium. During photocatalytic processes, the sample was periodically withdrawn, centrifuged to separate the photocatalyst from the solution and used for the absorbance measurement. The sample absorbances were recorded by using Thermo fisher UV–Visible spectrophotometer.

### 6.3 Results and Discussion

#### 6.3.1 Morphology and composition characterization

Figure 6.1 shows the PXRD patterns of pure TS, pure BVO the inorganic hybrid nanocomposites BPTS1, BPTS2 and BPTS3 which were used to elucidate the phase and structural parameters. In pure BVO, all the diffraction peaks can be indexed to BVO which is identical to the standard (JCPDS no. 14-0688). Monoclinic crystal structure of Characteristic peaks at  $18.5^\circ$ ,  $35^\circ$ , and  $46^\circ$  of  $2\theta$  is observed for m-BiVO<sub>4</sub>.<sup>[42]</sup> The high crystallinity of the m-BiVO<sub>4</sub> due to the sharp and narrow diffraction peaks. A broad peak centered at  $23^\circ$  was ascribed to the mesoporous Titanosilicate. Similar bands were found for the BPTS nanocomposites. Moreover, no other impurity phase was seen, indicating the BPTS to be a two-phase composite.

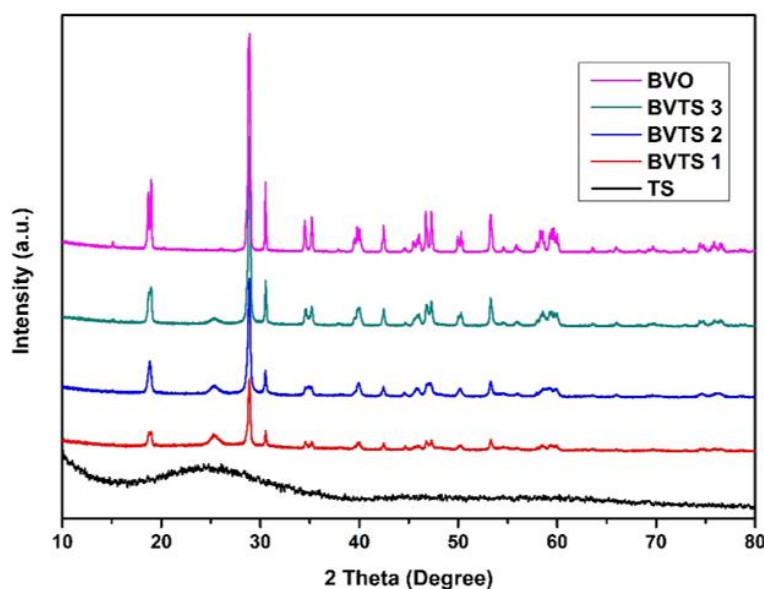


**Figure 6.1:** XRD spectra of pure TS, pure BVO, BPTS1, BPTS2 and BPTS3 nanocomposites

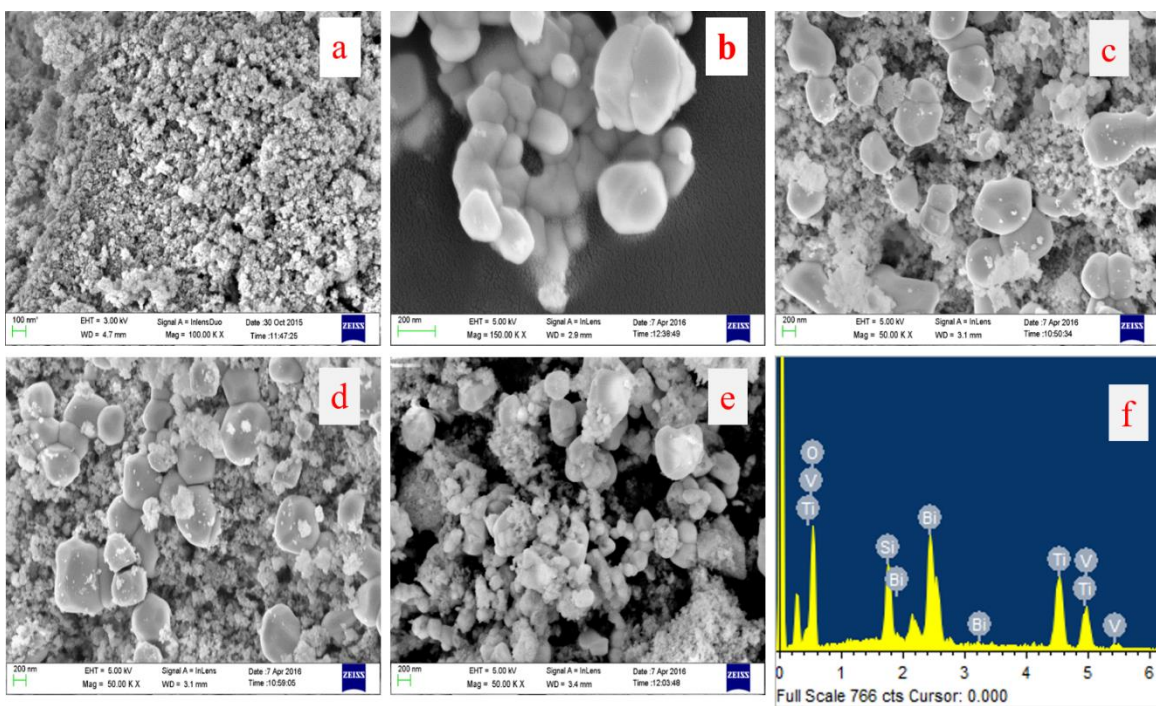


**Figure 6.2:** FE-SEM images of a) pure TS, b) pure BVO, c) BVTS1 d) BVTS2 and e) BVTS3 f) EDX Analysis of BVTS1 nanocomposites

The figure 6.2 shown, morphological structure of pure TS, pure BVO and BVTS nanocomposites. Spherical shapes with porous nature of TS observed in both pure TS and BVTS nanocomposites. The morphology and particle size of prepared BVTS nanocomposites was observed by taking FE-SEM images with different magnifications. The images obtained at higher magnifications suggested that the nanoparticles formed aggregates or clusters. EDS spectrum is elucidating that the synthesized coupled catalyst is made up of O, Si, Ti, V and Bi only (table 6.1). No other notable impurities were detected. From the FE-SEM images, it was decided that synthesized sample is composed of agglomerated the porous pure TS is well distributed over the BVO surface and form a heterojunction between this inorganic TS and BVO which makes facile electron transfer for various catalytic applications.

TEM images (figure 6.3a) is the porous structure of pure titanosilicate. Figure 6.3 (b&c) indicated BVTS 1 hybrid nanocomposite, from these results we confirmed a good heterojunction formed between the TS and BVO. HR-TEM studies confirm the formation of the interface between Titanosilicate and BiVO<sub>4</sub> in the composite system (figure 6.3d). Furthermore, the selected area electron diffraction (SAED) pattern (inset of figure 6.3d) shows a faint but full diffraction ring which is indexed to the characteristic planes of

Titanosilicate/BiVO<sub>4</sub>. However, Titanosilicate/BiVO<sub>4</sub> hybrid nanocomposites also exhibit a certain degree of particle agglomeration. From the XRD, pure TS broad peak at 23°. BVTS hybrid nanocomposite TS peak shifted to 25°. In addition to the microscopic results as the evidence for hetero-junction formation between TS and BVO.

S.No.	Elements	Atomic %	Weight %
1	O	70.11	34.17
2	Si	6.37	5.45
3	Ti	12.48	18.21
4	V	5.84	9.06
5	Bi	5.20	33.11

**Table 6.1:** FE-SEM EDX of elemental composition BVTS1 hybrid nanocomposite

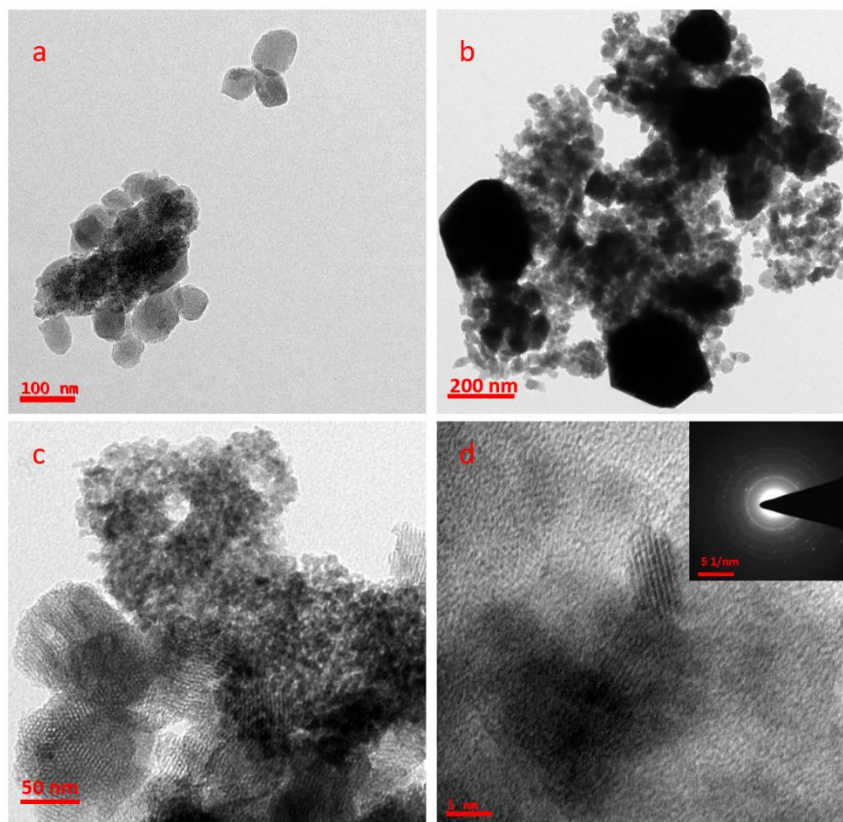


**Figure 6.3:** TEM images of a) pure TS, b) BVTS1 c) magnified BVTS1 and d) HR-TEM of BVTS1 (SAED pattern of BVTS1 inset figure)

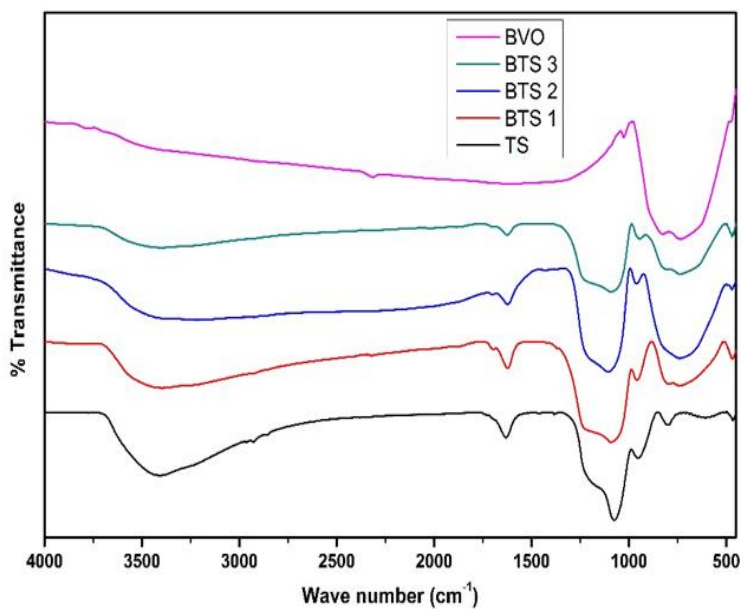


**Figure 6.4:** FT-IR Spectra of pure TS, pure BVO, BVTS1, BVTS2 and BVTS3 composites

The FT-IR spectra of the prepared samples were shown in figure 6.4. The pure BVO, which is attributed to Bi-O and V-O vibration bands at 650 and 850  $\text{cm}^{-1}$ .<sup>[42]</sup> pure TS, shows that peaks around 1700 and 3430  $\text{cm}^{-1}$  corresponding to the carboxyl and hydroxyl groups respectively. The Si-O-Si bands at near 1100, 802 and 467  $\text{cm}^{-1}$  strong peaks to the which implies the condensation of silicon alkoxide. It is observed that the 960  $\text{cm}^{-1}$  band is Ti peak in TS. Thangaraj *et al.* have demonstrated that the IR band around 960  $\text{cm}^{-1}$  exhibited by TS zeolites can also be attributed to a stretching mode of a  $[\text{SiO}_4]$  unit bonded to a  $\text{Ti}^{+4}$  ion  $[\text{O}_3\text{SiOTi}]$ .<sup>[43]</sup> The characteristic peaks of Titanosilicate and BVO are retained in the BVTS in organic hybrid nanocomposite samples.

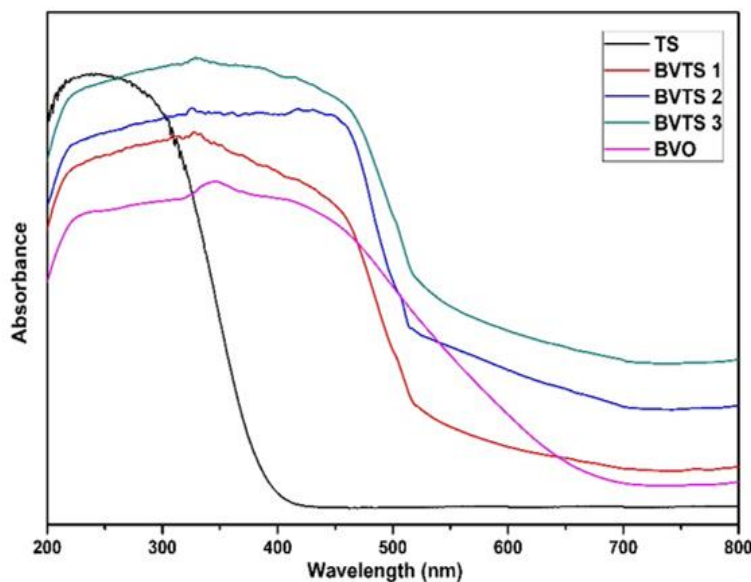


**Figure 6.5:** UV-Vis DRS Spectra of pure TS, pure BVO, BVTS1, BVTS2 and BVTS3 hybrid nanocomposites

The energy band structure feature of a semiconductor is considered as a key factor in determining its photocatalytic activity. Figure 6.5 shows the UV-Vis diffuse reflectance absorption spectra of the as-prepared samples. All of the samples show the strong absorption in the UV and Visible light regions. The steep shape of the spectrum indicates that the visible light absorption is not due to the transition from the impurity level but due to the band gap transition.<sup>[44,45]</sup> For a crystalline semiconductor, the optical absorption near the band edge follows the equation  $\alpha h\nu = \frac{1}{4}A(h\nu - E_g)^{n/2}$ , where  $\alpha$ ,  $\nu$ ,  $E_g$  and  $A$  are an absorption coefficient, a light frequency, the band gap, and a constant, respectively. In this work, the band gaps are estimated to be 3.1 eV, 2.2 eV, 2.40 eV, 2.36 eV and 2.34 eV from the absorption edge corresponding to the pure TS, pure BVO, BVTS1, BVTS2 and BVTS3 nanocomposites, respectively.

### 6.3.2 Photoluminescence

To further confirm the separation mechanism of electron-hole pairs in BVTS1 hybrid nanocomposite as discussed above, the room temperature PL properties of the as-prepared pure BVO and BVTS1 hybrid nanocomposite were investigated as shown in figure 6.6. The PL spectra of pure BVO and BVTS1 hybrid nanocomposite were obtained at an excitation wavelength of 325 nm. An emission at about 546 nm was obviously detected in both pure BVO and m- BVTS1 hybrid nanocomposite. However, the

fluorescence intensity of BVTS1 hybrid nanocomposite (red line) was weaker than that of pure BVO (black line), clearly demonstrating that the recombination of photogenerated electron-hole pairs was inhibited greatly in the BVTS1 hybrid nanocomposite. This result is in good agreement with the analysis by the energy band position of BVO and TS, as discussed above. Thus, the PL spectra offer direct evidence for the efficient separation of photogenerated electron-hole pairs in the BVTS1 hybrid nanocomposite, leading to enhanced photocatalytic degradation of RhB, compared to pure BVO and pure TS.

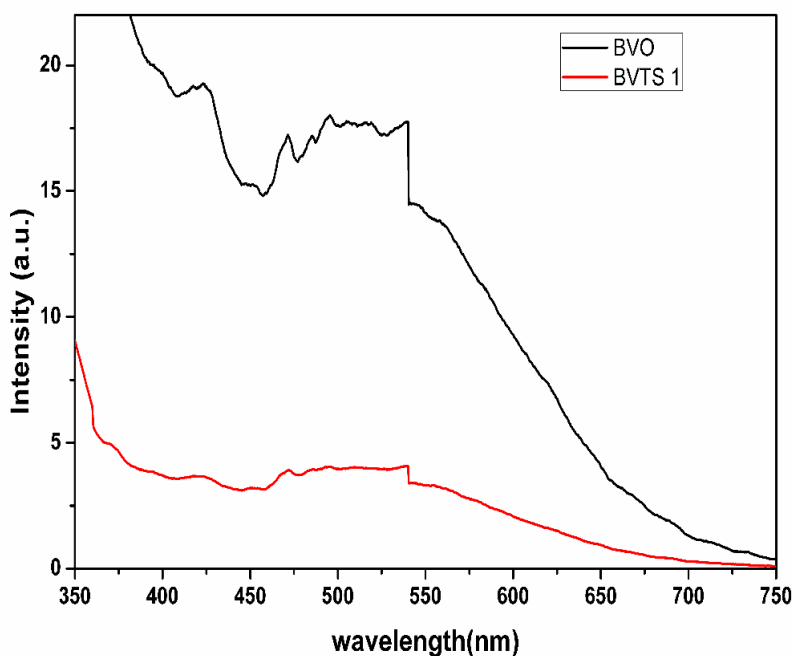


**Figure 6.6:** Photoluminescence spectra of pure BVO and BVTS1 hybrid nanocomposite

### 6.3.3 Photocatalytic activity and the mechanism:

The results indicate that the visible-light-response of BVTS1 nanocomposite photocatalyst is greatly improved by coupling the appropriate amount of Titanosilicate (TS). Therefore, BVTS1 composite photocatalyst exhibits the higher photocatalytic efficiency than others. The photocatalytic performance of BVTS1 powder synthesized by the combustion route was evaluated in terms of the photocatalytic degradation of RhB in aqueous solution under sunlight irradiation. The following figure 6.7 shows the absorption spectra of RhB dye solution with BVTS1 nanocomposite under direct sunlight irradiation for different time intervals. The dye degrades at a faster rate under sunlight (60 min). The concentration was recorded on Perkin Elmer (Lambda 25) UV-visible spectrophotometer.

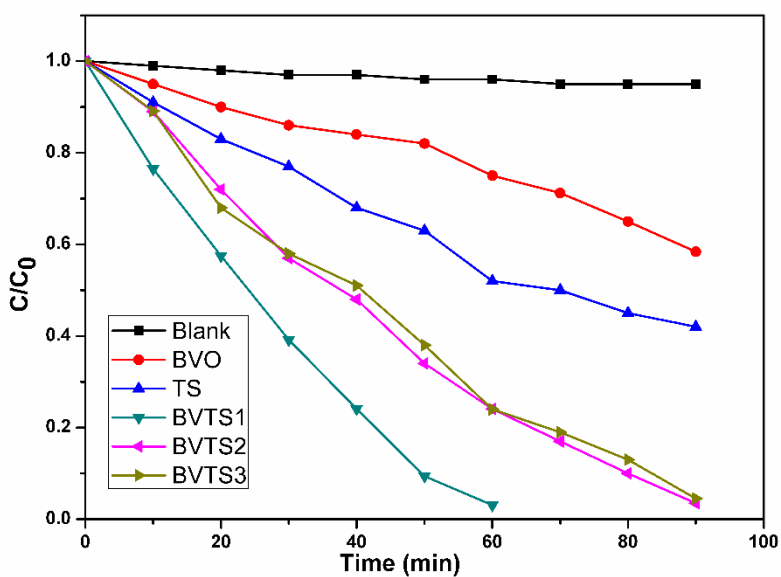


**Figure 6.7:** Photodegradation of RhB dye under the irradiation of direct sunlight with pure TS, pure BVO and BVTS hybrid nanocomposites

To demonstrate the influence of Titanosilicate on the photodegradation, the degradation of RhB with pure BVO was studied under visible light. The following figure 6.7 shows the variation of  $C/C_0$  vs time for pure TS, Pure BVO and BVTS nanocomposites, where  $C_0$  is the RhB initial concentration and  $C$  is the RhB concentration with respect to the degradation time 't'. It is obvious from the figure 6.7 that the rate of degradation was quite faster in the composite compared to pure BVO, which shows the beneficial impact of Titanosilicate on the photocatalytic performance of the composite. The photocatalytic activity of the BVTS nanocomposites prepared by the present method is higher than the BVO based composites prepared by hydrothermal method.

The photocatalytic performances of TS, BVO and BVTS composites are evaluated by photocatalytic removal of RhB in the liquid phase as shown in figure 6.7. The blank experiment in the absence of photocatalysts demonstrates that no RhB is photodegraded by the sunlight. All the samples exhibit the photocatalytic activity in RhB degradation under visible light irradiation. However, the photocatalytic activity of TS and BVO is low. All of the BVTS nanocomposites exhibit higher photocatalytic activities than that of TS and BVO.

Based on the above experimental results, a possible photocatalytic mechanism

has been proposed to explain the enhanced photocatalytic activity of the as-synthesized BVTS for the photocatalytic degradation of RhB. The visible-light driven electron-hole separation and the transport of photogenerated charge carriers on the BVTS nanocomposite are illustrated in figure 6.8 The conduction band (CB) and valence band (VB) potentials of TS and BVO were calculated using the following equation.<sup>[46,47]</sup>

$$E_{VB} = X - E_e + 0.5(E_g)$$

$$E_{CB} = E_{VB} - E_g$$

Where  $E_{VB}$  and  $E_{CB}$  are valance and conduction band potentials,  $X$  is the electronegativity of the semiconductor,  $E_e$  is the energy of free electrons on the hydrogen scale (4.5 eV) and  $E_g$  is the bandgap energy of the semiconductor. The absolute electronegativity of TS and BVO is 5.81 and 6.04 eV. The calculated CB and VB of TS is -0.24 and 2.96 eV, whereas CB and VB of BVO are 0.44 and 2.64 eV, respectively. The conduction band (CB) of TS (-0.24) is more negative than that of BVO (0.44). Thus, the photogenerated electrons transfer from the CB of TS to that of BVO, while the holes remain in the VB of TS.

The photogenerated electrons and holes are easily separated in the transfer process, thereby enhancing the activity of the photocatalyst for the degradation of RhB. The electron would subsequently transfer to the photocatalyst surface to react with water and oxygen to generate some active species such as hydroxyl radicals ( $\cdot OH$ ) and superoxide radicals ( $O_2\cdot$ ) These radicals are able to oxidize the pollutant due to their high oxidative capacities. The possible photocatalytic reactions are similar to the reports available in the literature and figure 6.7 shows the schematic illustration of the photocatalytic degradation of RhB over the BVTS photocatalyst under sunlight irradiation.

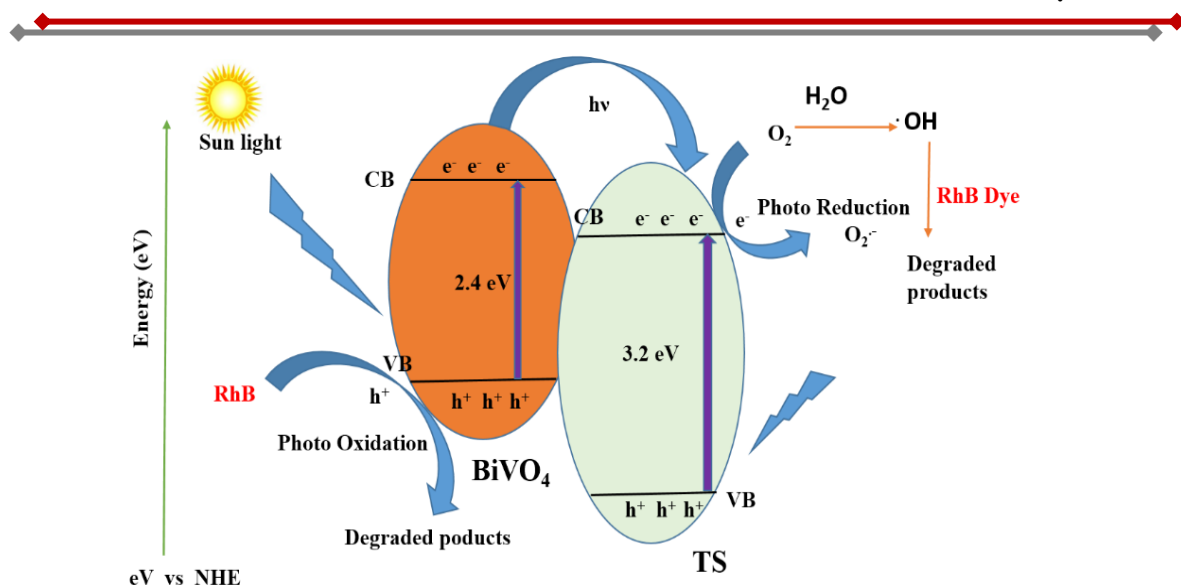


**Figure 6.8:** Schematic illustration of the photocatalytic degradation mechanism of RhB over TS/BiVO<sub>4</sub> under sunlight irradiation

The energy band diagram of the Titanosilicate/BiVO<sub>4</sub> heterostructure photocatalyst after the thermodynamic equilibrium is presented in figure 6.8. BiVO<sub>4</sub> is considered as an intrinsic semiconductor, so the Fermi level in BiVO<sub>4</sub> lies in the middle of the conduction band and valence band, which is approximately equal to 1.6 eV. According to the literature survey band energy level of BiVO<sub>4</sub>, E<sub>C</sub> and E<sub>V</sub> increase from 0.4 eV to -1.3 eV, 2.8 eV to 1.1 eV respectively<sup>[47]</sup>. Obviously, the difference of E<sub>CB</sub> between BiVO<sub>4</sub> and TS allowed the transfer of an electron from the conduction band of BiVO<sub>4</sub> to that of TS. When the system is irradiated with visible light, an electron (e<sup>-</sup>) is promoted from the valence band into the conduction band of BiVO<sub>4</sub> leaving a hole (h<sup>+</sup>) behind. Then the excited-state electrons produced by BiVO<sub>4</sub> can be injected into the conduction band of the coupled TS due to the joint of the electric fields between two materials. The conduction electrons are good reductants which could capture the adsorbed O<sub>2</sub> on the surface of the catalyst and reduce it to O<sub>2</sub><sup>•-</sup>. It can be further dissociated or reduced by photoinduced electrons, so there would be a constant stream of the surface 'OH groups to come into being. In the presence of hydroxyl radicals, the efficiently photocatalytic degradation of RhB can be carried out smoothly. In addition, the photogenerated hole in BiVO<sub>4</sub> also may activate some unsaturated organic pollutants, resulting in subsequent decomposition.

**Table 6.1:** Detailed comparison and correlation between vanadium pentoxide and bismuth vandate

Properties	<b>V<sub>2</sub>O<sub>5</sub></b>	<b>BiVO<sub>4</sub></b>
<b>Nature</b>	Mono metallic	Bi metallic
<b>Synthesis method</b>	Hydrothermal	Reflux
<b>XRD</b>	Orthorhombic crystal structure	Monoclinic Crystal structure
<b>UV-Visible DRS</b>	Band gap 2.30 eV	Band gap 2.40 eV
<b>FT-IR</b>	V-O-V , V-O at 829 and 1018 cm <sup>-1</sup>	Bi-O, V-O at 650 and 850 cm <sup>-1</sup>
<b>PL</b>	Emission peak at 549 nm	Emission peak at 546 nm
<b>FE-SEM</b>	Nano rods	Irregular spherical

#### 6.4 References:

- [1] B. Neppolian, *J. Hazard. Mater.* **2002**, *89*, 303–317.
- [2] D. S. Bhatkhande, V. G. Pangarkar, A. A. Beenackers, *J. Chem. Technol. Biotechnol.* **2002**, *77*, 102–116.
- [3] J. Li, W. Zhao, Y. Guo, Z. Wei, M. Han, H. He, S. Yang, C. Sun, *Appl. Surf. Sci.* **2015**, *351*, 270–279.
- [4] X. Lin, D. Xu, S. Jiang, F. Xie, M. Song, H. Zhai, L. Zhao, G. Che, L. Chang, *Catal. Commun.* **2017**, *89*, 96–99.
- [5] W. Ma, J. Li, X. Tao, J. He, Y. Xu, J. C. Yu, J. Zhao, *Angew. Chemie Int. Ed.* **2003**, *42*, 1029–1032.
- [6] M. R. Hoffmann, S. T. Martin, W. Choi, D. W. Bahnemann, *Chem. Rev.* **1995**, *95*, 69–96.
- [7] A. L. Linsebigler, G. Lu, J. T. Yates, *Chem. Rev.* **1995**, *95*, 735–758.
- [8] A. Fujishima, T. N. Rao, D. A. Tryk, *J. Photochem. Photobiol. C Photochem. Rev.* **2000**, *1*, 1–21.
- [9] D. Chatterjee, S. Dasgupta, *J. Photochem. Photobiol. C Photochem. Rev.* **2005**, *6*, 186–205.
- [10] M. Selvaraj, *Catal. Sci. Technol.* **2014**, *4*, 2674.
- [11] F. X. Llabrés i Xamena, P. Calza, C. Lamberti, C. Prestipino, A. Damin, S.

Bordiga, E. Pelizzetti, A. Zecchina, *J. Am. Chem. Soc.* **2003**, *125*, 2264–2271.

[12] J.-W. Jang, S. H. Choi, S. Cho, M. Seol, K.-H. Lee, K. Yong, J. S. Lee, *J. Phys. Chem. C* **2012**, *116*, 15427–15431.

[13] D. H. Wells, W. N. Delgass, K. T. Thomson, *J. Am. Chem. Soc.* **2004**, *126*, 2956–2962.

[14] C. Yu, H. Chu, Y. Wan, D. Zhao, *J. Mater. Chem.* **2010**, *20*, 4705.

[15] C. Shi, W. Wang, N. Liu, X. Xu, D. Wang, M. Zhang, P. Sun, T. Chen, *Chem. Commun.* **2015**, *51*, 11500–11503.

[16] T.-D. Nguyen-Phan, E. W. Shin, V. H. Pham, H. Kweon, S. Kim, E. J. Kim, J. S. Chung, *J. Mater. Chem.* **2012**, *22*, 20504.

[17] A. Kudo, K. Ueda, H. Kato, I. Mikami, *Catal. Letters* **1998**, *53*, 229–230.

[18] J. Xu, W. Wang, J. Wang, Y. Liang, *Appl. Surf. Sci.* **2015**, *349*, 529–537.

[19] S. Xue, Z. Wei, X. Hou, W. Xie, S. Li, X. Shang, D. He, *Appl. Surf. Sci.* **2015**, *355*, 1107–1115.

[20] S. Yang, D. Xu, B. Chen, B. Luo, X. Yan, L. Xiao, W. Shi, *Appl. Surf. Sci.* **2016**, *383*, 214–221.

[21] X. Lin, D. Xu, J. Zheng, M. Song, G. Che, Y. Wang, Y. Yang, C. Liu, L. Zhao, L. Chang, *J. Alloys Compd.* **2016**, *688*, 891–898.

[22] P. Madhusudan, J. Ran, J. Zhang, J. Yu, G. Liu, *Appl. Catal. B Environ.* **2011**, *110*, 286–295.

[23] X. Lin, D. Xu, Y. Xi, R. Zhao, L. Zhao, M. Song, H. Zhai, G. Che, L. Chang, *Colloids Surfaces A Physicochem. Eng. Asp.* **2017**, *513*, 117–124.

[24] R. Sharma, Uma, S. Singh, A. Verma, M. Khanuja, *J. Photochem. Photobiol. B Biol.* **2016**, *162*, 266–272.

[25] X. Lin, B. Wei, X. Zhang, M. Song, S. Yu, Z. Gao, H. Zhai, L. Zhao, G. Che, *Sep. Purif. Technol.* **2016**, *169*, 9–16.

[26] L. Zhang, D. Chen, X. Jiao, *J. Phys. Chem. B* **2006**, *110*, 2668–2673.

[27] S. Tokunaga, H. Kato, A. Kudo, *Chem. Mater.* **2001**, *13*, 4624–4628.

[28] W. Yao, H. Iwai, J. Ye, *Dalt. Trans.* **2008**, 1426.

[29] Y. Zhao, Y. Xie, X. Zhu, S. Yan, S. Wang, *Chem. - A Eur. J.* **2008**, *14*, 1601–1606.

[30] O. F. Lopes, K. T. G. Carvalho, G. K. Macedo, V. R. de Mendonça, W. Avansi, C. Ribeiro, *New J. Chem.* **2015**, *39*, 6231–6237.

[31] P. Wang, J. Y. Zheng, D. Zhang, Y. S. Kang, *New J. Chem.* **2015**, *39*, 9918–9925.

[32] L. Ge, *J. Mol. Catal. A Chem.* **2008**, *282*, 62–66.

[33] L. Ren, L. Jin, J.-B. Wang, F. Yang, M.-Q. Qiu, Y. Yu, *Nanotechnology* **2009**, *20*, 115603.

[34] A. K. Bhattacharya, K. K. Mallick, A. Hartridge, *Mater. Lett.* **1997**, *30*, 7–13.

[35] S. Kohtani, S. Makino, A. Kudo, K. Tokumura, Y. Ishigaki, T. Matsunaga, O. Nikaido, K. Hayakawa, R. Nakagaki, *Chem. Lett.* **2002**, *31*, 660–661.

[36] L. Zhou, W. Wang, S. Liu, L. Zhang, H. Xu, W. Zhu, *J. Mol. Catal. A Chem.* **2006**, *252*, 120–124.

[37] H. M. Zhang, J. B. Liu, H. Wang, W. X. Zhang, H. Yan, *J. Nanoparticle Res.* **2008**, *10*, 767–774.

[38] M. C. Neves, T. Trindade, *Thin Solid Films* **2002**, *406*, 93–97.

[39] R. He, S. Cao, P. Zhou, J. Yu, *Chinese J. Catal.* **2014**, *35*, 989–1007.

[40] R. Strobel, H. J. Metz, S. E. Pratsinis, *Chem. Mater.* **2008**, *20*, 6346–6351.

[41] X. Lin, S. Yu, Z. Gao, X. Zhang, G. Che, *J. Mol. Catal. A Chem.* **2016**, *411*, 40–47.

[42] W. Yin, W. Wang, L. Zhou, S. Sun, L. Zhang, *J. Hazard. Mater.* **2010**, *173*, 194–199.

[43] A. Thangaraj, R. Kumar, P. Ratnasamy, *J. Catal.* **1991**, *131*, 294–297.

[44] M. Shang, W. Wang, L. Zhou, S. Sun, W. Yin, *J. Hazard. Mater.* **2009**, *172*, 338–344.

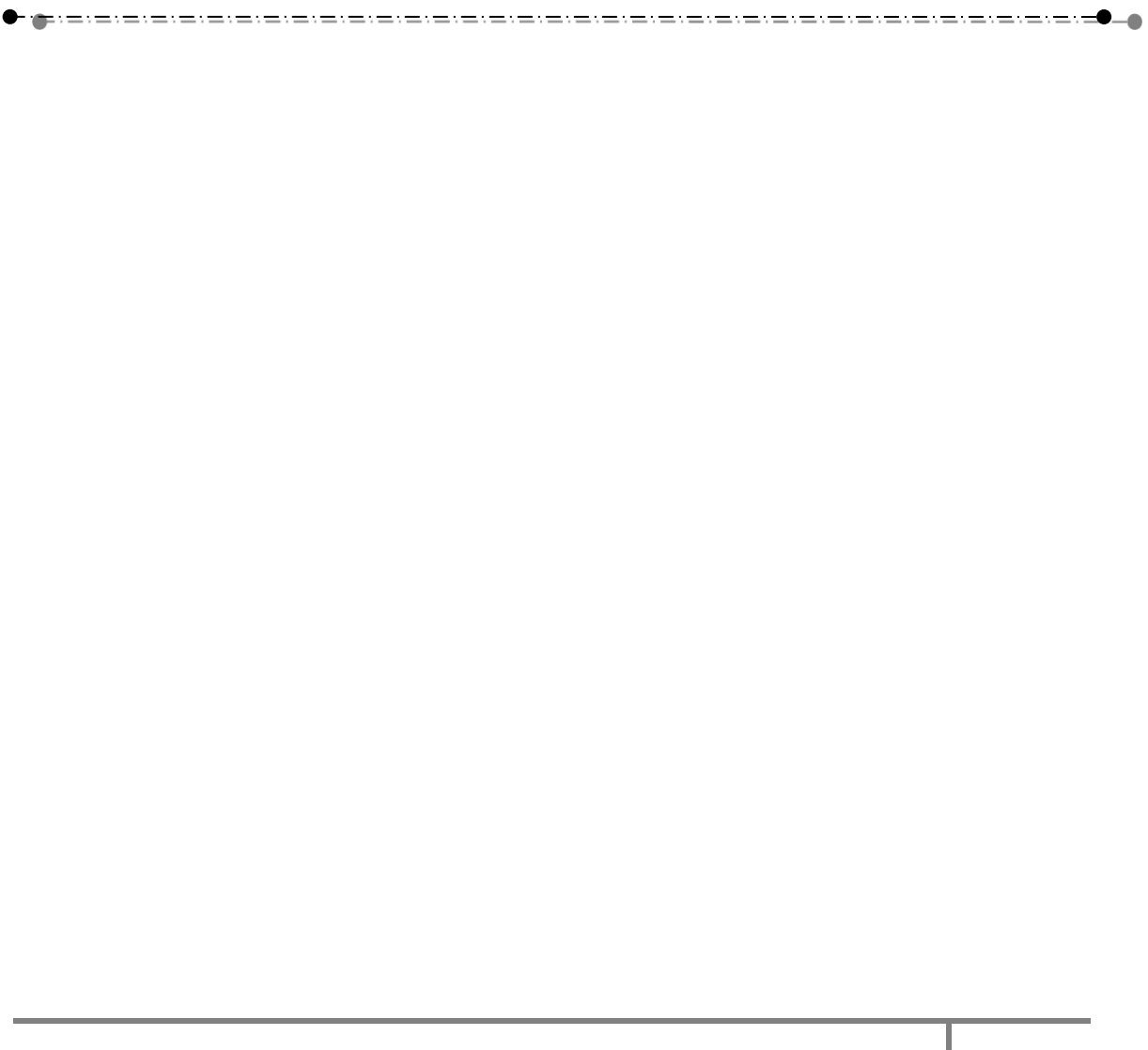
[45] L. Zhou, W. Wang, L. Zhang, H. Xu, W. Zhu, *J. Phys. Chem. C* **2007**, *111*, 13659–13664.

[46] J. Sun, X. Li, Q. Zhao, J. Ke, D. Zhang, *J. Phys. Chem. C* **2014**, *118*, 10113–10121.

[47] Y. Hu, D. Li, Y. Zheng, W. Chen, Y. He, Y. Shao, X. Fu, G. Xiao, *Appl. Catal. B Environ.* **2011**, *104*, 30–36.

## CHAPTER VII

### Summary and Conclusions



## 7 Summary and Conclusions

### 7.1 Present thesis

This thesis consists of 7 chapters. Chapter 1 describes the general introduction of the present work and chapters 2, 4, 5 and 6 are presented original research work on the development of visible light active photocatalysts, Chapter 3 deals with the development of UV light active photocatalyst for environmental application. Finally, chapter 7 (This chapter) focuses on a summary and conclusions.

### 7.2 Conclusions

During the course of this research work, a number of conclusions have been reached, regarding the preparation, characterization and utilization of visible light based photocatalysts for the degradation of organic pollutants.

**Chapter 1:** This chapter describes the general background of photocatalysis, state of the problem, objective and scope of the present work. It is also described Literature review on present work, visible light photocatalysis and nanotechnology, characterization techniques, synthetic methodology and evolution of photocatalytic activity.

**Chapter 2:** This chapter investigates the porous titanosilicate/g-C<sub>3</sub>N<sub>4</sub> hybrid nanocomposite for enhanced visible light photocatalysis. The Titanosilicate/g-C<sub>3</sub>N<sub>4</sub> nanocomposites have been successfully prepared by a facile and *sonochemical* treatment method. The TSCN nanocomposite exhibits enhanced photocatalytic activity for the degradation of RhB under visible light irradiation. More importantly, TSCN photocatalyst could be recovered and reused for photocatalytic activity even after five successive cycles. Therefore, it can be used as a promising photocatalyst for practical applications in environmental purification and clean hydrogen energy production from water splitting. This chapter was published in *Microporous Mesoporous Materials*, March 2017.

**Chapter 3:** This chapter examines Fe<sub>3</sub>O<sub>4</sub> nanoparticles decorated on porous titanosilicate for enhanced UV light irradiation. The Titanosilicate/Fe<sub>3</sub>O<sub>4</sub> nanocomposites have been successfully prepared by a facile, effective, and reproducible *in situ* growth mechanism. The monodispersed Fe<sub>3</sub>O<sub>4</sub> nanoparticles with a size of about 10 nm were deposited on porous titanosilicate and effectively prevented the Fe<sub>3</sub>O<sub>4</sub> nanoparticles from aggregating together. The TSFO nanocomposite exhibits enhanced photocatalytic activity for the

degradation of MB under UV light irradiation. More importantly, TSFO photocatalyst could be recovered by external magnetic field and recycled without loss of photocatalytic activity even after six successive cycles. This chapter was published in *Materials Today proceedings*, March 2017.

**Chapter 4:** This chapter deals with  $\text{Fe}_3\text{O}_4@\text{Titaniumsilicate}/\text{g-C}_3\text{N}_4$  hybrid nanocomposite for visible light induced photocatalytic degradation of Rhodamine B. The FTSCN hybrid nanocomposites have been successfully prepared via a facile *insitu* growth mechanism. Significantly, the enhanced visible light photocatalysis is achieved due to prolong life time of charge carrier transfer at the interface of the FTSCN. Photocatalytic mechanism is proposed for prolong life time of charge carrier transfer at the interface of the  $\text{Fe}_3\text{O}_4@\text{Titaniumsilicate}/\text{g-C}_3\text{N}_4$  by trapping experiments of photoinduced electrons and holes under visible light irradiation. More importantly, the synthesized FTSCN hybrid nanostructure possesses high photostability. This idealize versatile hybrid nanostructure prepared from a cost-free and environmentally friendly process would be useful for various applications, including catalysis, sensors, photonics and energy storage and conversion.

**Chapter 5:** This chapter examines the detail study of Titanosilicate/Vanadium pentoxide which showed enhanced visible light photocatalytic activity. The Titanosilicate/ $\text{V}_2\text{O}_5$  inorganic hybrid nanocomposite photocatalysts have been synthesized via a facile ultrasonic dispersion method at room temperature. These results indicate that the improved photocatalytic efficiency is mainly due to high charge separation efficiency and band energy matching and the decreased recombination for Titanosilicate/vanadium pentoxide hetero/nanojunction. More importantly, the as-prepared nanocomposite possesses high reusability. Therefore, these hybrid nanocomposites are promising candidate for degradation of organic pollutants under visible light.

**Chapter 6:** This chapter explores a novel porous titanosilicate/bismuth vandate hybrid nanocomposite system for visible light responsive photocatalysis. The titanosilicate/ $\text{BiVO}_4$  inorganic hybrid nanocomposites photocatalysts have been synthesized by a facile and reproducible *in situ* precipitation method at room temperature. Our results clearly show that the crystal structure and morphology of  $\text{BiVO}_4$  are not changed during the hybridization. Interestingly, the hybrid nanocomposites exhibited significantly enhanced photocatalytic activity for the degradation of RhB under visible light irradiation. The high photocatalytic performance could be attributed to synergistic

effects which promote the migration efficiency of photoinduced electron–hole pairs at the interface of the titanosilicate/BiVO<sub>4</sub>. More importantly, the as-prepared nanocomposite possesses high reusability. Therefore, it can be used as a promising photocatalyst for practical applications in environmental purification and clean hydrogen energy production from water splitting. This chapter was published in *New Journal of Chemistry*, February 2017.

### 7.3 Summary

The obtained results showed that the proficiency of a photodegradation method largely depends on the physicochemical features of the photocatalyst. The Titanosilicate/g-C<sub>3</sub>N<sub>4</sub>, Fe<sub>3</sub>O<sub>4</sub>@Titanosilicate/g-C<sub>3</sub>N<sub>4</sub>, Titanosilicate/vanadium pentoxide, Titanosilicate/BiVO<sub>4</sub> photocatalysts appear to be very promising materials for the photodegradation of various aromatic compounds under visible light and Titanosilicate/Fe<sub>3</sub>O<sub>4</sub> photocatalysts for photocatalytic degradation of MB under UV light. Photocatalytic oxidation processes using porous titanosilicate based catalysts appear to be a very suitable procedure for the detoxification of water containing moderate organic content, leading to the mineralization of the contaminants or to their alteration to more biodegradable materials.

### 7.4 Outlook for future work

- ❖ Visible light driven photocatalytic degradation of organic pollutant, using above porous Titanosilicate-based photocatalysts was described as a possible initiator for future work.
- ❖ The Titanosilicate/g-C<sub>3</sub>N<sub>4</sub>, Fe<sub>3</sub>O<sub>4</sub>@Titanosilicate/g-C<sub>3</sub>N<sub>4</sub>, Titanosilicate/V<sub>2</sub>O<sub>5</sub>, Titanosilicate/BiVO<sub>4</sub> photocatalysts could be used in the photocatalytic degradation of other priority pollutants such as dyes, pesticides and pharmaceuticals as well as clean energy H<sub>2</sub> production from water splitting.
- ❖ Furthermore, it would be interesting to work on the formation of porous Titanosilicate-based photocatalysts with unique nanoarchitecture in order to fulfil the needs of practical application.
- ❖ More importantly, cost-effective magnetic porous Titanosilicate-based photocatalyst facilitates its reutilization and also opens the possibility of working in a continuous regime.

- ❖ Finally, a cost effective synthesis of Titanosilicate/g-C<sub>3</sub>N<sub>4</sub>, Fe<sub>3</sub>O<sub>4</sub>@Titanosilicate/g-C<sub>3</sub>N<sub>4</sub>, Titanosilicate/vanadium pentoxide, Titanosilicate/BiVO<sub>4</sub> photocatalysts showed to be very active in the visible light region, the possibility of using natural solar light as irradiation source can result on both environmental and economical advantages.



## LIST OF PUBLICATIONS, CONFERENCES & BIO-DATA



## 8 LIST OF PUBLICATIONS, CONFERENCES

### Publications in Peer-Reviewed/Refereed International Journals

1. “Photocatalytic degradation of rhodamine B over a novel mesoporous Titanosilicate/g-C<sub>3</sub>N<sub>4</sub> nanocomposite under direct sunlight irradiation”  
**Ajay Kumar Adepu**, Rajini Anumula and Venkatathri Narayanan\*  
**Microporous and Mesoporous Materials**, 247 (2017) 86-94.
2. “Synthesis, characterization, and photocatalytic degradation of Rhodamine B dye under sunlight irradiation of porous titanosilicate (TS)/bismuth vanadate (BiVO<sub>4</sub>) nanocomposite hybrid catalyst”.  
**Ajay Kumar Adepu**, Vamsi Katta and Venkatathri Narayanan\*  
**New Journal of Chemistry**, 41 (2017) 2498-2504.
3. “Synthesis and Characterization of Magnetically Separable Porous Titanium Silicate Nanocomposite Catalyst for Environmental Applications”.  
**Ajay Kumar Adepu** and Venkatathri Narayanan\*  
**Material Today Proceedings**, 4 (2017) 19-24.
4. “Synthesis and characterization of a novel porous titanium silicate/g-C<sub>3</sub>N<sub>4</sub> hybrid nanocomposite catalyst for environmental applications”.  
**Ajay Kumar Adepu** and Venkatathri Narayanan\*  
**AIP Conference Proceedings**, 1724, 020003 (2016).
5. “Titanium aminophosphates as efficient, economical, and recyclable catalysts for the synthesis of xanthenediones.”  
A. Rajini, C. Suman, **A. Ajay Kumar**, S. Suresh, and N. Venkatathri\*.  
**Synthetic Communications**, 46 (2016) 1671–1677.
6. “Titanium aminophosphates: synthesis, characterization and crystal violet dye degradation studies.”  
Rajini Anumula, **Ajay Kumar Adepu**, Suman Chirra, Suresh Siliveri and Venkatathri Narayanan\*  
**RSC Advances**, 6 (2016) 507-514.

7. "Porous palladium aminophosphates: synthesis, characterization, antimicrobial and cytotoxicity Studies." Anumula Rajini, **Ajay Kumar Adepu**, Suman Chirra and Venkatathri Narayanan\*. **RSC Advances**, 5 (2015) 66956–66964.

8. "Titanium aminophosphates: synthesis, characterization, antimicrobial and cytotoxicity Studies." Anumula Rajini, **Ajay Kumar Adepu**, Suman Chirra and Narayanan Venkatathri\*. **RSC Advances**, 5 (2015) 87713–87722.

9. "Titanium aminophosphates: synthesis, characterization and orange G dye degradation Studies." Anumula Rajini, Muralasetti Nookaraju, Suman Chirra, **Ajay Kumar Adepu** and Narayanan Venkatathri\* **RSC Advances**, 5 (2015) 106509–106518.

10. "Porous Palladium Aminophosphates: A Study on Their Synthesis, Characterization and Catalytic Applications." A. Rajini, S. Chirra, **A. Ajay Kumar**, and N. Venkatathri\* **Advance Porous Materials**, 3 (2015) 1–6.

11. "Promoter Induced Rapid Synthesis of Hollow Silica Nano Cuboids from Octadecyltrichloro Silane." N. Venkatathri\*, **A. Ajay Kumar**, M. Nookaraju, A. Rajini, and I. A. K. Reddy **Advance Porous Materials**, 2 (2014) 1–4.

12. "Influence of Organic Amines on Size and Properties of Amorphous Porous Nano Silica" N. Venkatathri\*, M. Nookaraju, A. Rajini, A. Ajay Kumar and I. A. K. Reddy **Advance Porous Materials**, 1 (2013) 224–228.

13. "Magnetically Separable Porous Titanosilicate/Fe<sub>3</sub>O<sub>4</sub> Hybrid Nanocomposites with Enhanced Photocatalytic Performance under UV light Irradiation." **Ajay Kumar Adepu** and Venkatathri Narayanan\*.

**New journal of Chemistry (under Review).**

14. "Development of porous Titanosilicate/Vanadium pentoxide Inorganic Heterostructures: an Efficient Photocatalyst for Methylene Blue dye Degradation under Sun Light Irradiation."

**Ajay kumar Adepu, Vamsi Katta, Venkatathri Narayanan \***

**(Manuscript under preparation).**

15. "Three dimensional heterostructures of  $Fe_3O_4$ @Titanosilicate/g- $C_3N_4$  and its photocatalytic degradation of rhodamine B under Sunlight irradiation."

**Ajay Kumar Adepu, Vamsi Katta, Venkatathri Narayanan\***

**(Manuscript under preparation).**

16. "Novel Porous Titanosilicate/ $Ag_3VO_4$  Composite: Synthesis, Characterization and Visible-light driven Photocatalytic Activity."

**Ajay Kumar Adepu, Vamsi Katta, Venkatathri Narayanan\***

**(Manuscript under preparation).**

17. "Ternary Porous Titanosilicate/ $V_2O_5/ZnO$  nanocomposites: Synthesis and characterization of Photocatalysts for efficiently degradation of dye pollutants under visible-light irradiation."

**Ajay Kumar Adepu, Vamsi Katta, Venkatathri Narayanan\***

**(Manuscript under preparation).**

**Oral and Poster presentations in National/International Conferences**

1. Delivered the Oral Presentation in the 7<sup>th</sup> Asia Pacific Congress on Catalysis (**APCAT-7**) entitled "A novel Mesoporous Titanosilicate/ $V_2O_5$  nanocomposite Synthesis, characterization and Methylene blue photocatalytic degradation studies" during January 17-21<sup>st</sup>, 2017, organized by ICT Mumbai at Mumbai, Maharashtra, India.
2. Delivered the Oral Presentation in the 2nd International Conference on Emerging Technologies: Micro to Nano 2015 (**ETMN-2015**) entitled "Synthesis and characterization of a novel porous titanium silicate/g- $C_3N_4$  hybrid nanocomposite

catalyst for environmental applications" during 24–25<sup>th</sup> October 2015, organized by Manipal University Jaipur, CEERI Pilani, and BITS Pilani.

3. Delivered the Oral Presentation in the 22<sup>nd</sup> National Symposium on Catalysis (**CATSYMP 22**) entitled "Titanium dodecylamino phosphate: A novel efficient catalyst for tetrahydrobenzo[a]xanthen-11-ones synthesis" during January 7-9<sup>th</sup>, 2015 at organized by CSIR-Central Salt and Marine Chemicals Research Institute, Bhavnagar, Gujarat, India.
4. Delivered the Oral Presentation in the Research Conclave 2017 entitled "Synthesis, characterization, and photocatalytic degradation of Rhodamine B dye under sunlight irradiation of porous titanosilicate (TS)/bismuth vanadate (BiVO<sub>4</sub>) nanocomposite hybrid catalyst" during 18-19<sup>th</sup> March 2017, organised by National Institute of Technology Warangal, Warangal, India.
5. Delivered Poster Presentation in the Fourth International Conference on Advanced Oxidation Processes (**AOP-2016**) entitled "Magnetically Separable Porous Titanium Silicate Hybrid Nanocomposites with Enhanced Photocatalytic Performance" during 17-20<sup>th</sup> December 2016, organized by BITS Pilani K K Birla Goa Campus, Goa, India.
6. Delivered Poster Presentation in International Conference on Nano Science and Technology (**ICONSAT-2014**) entitled "Synthesis, Characterization of Nano Titanium Silicates and its Catalytic Applications" during 3-5<sup>th</sup> March 2014, organized by Institute of Nano science and Technology, Mohali, Punjab, India.
7. Delivered Poster Presentation in the National Conference on "Recent Advances in Surface Science" (**RASS – 2013**) entitled "Synthesis and Characterization of Hallow Silica Nano Cuboids from Octadecyl trichloro silane" during 14–15<sup>th</sup> February 2013, organised by Gandhigram rural institute (GRI), Dindigul, Tamilnadu, India.

## 9 BIO-DATA

### A. AJAY KUMAR

### Contact Address

S/O. A. Sudhakar  
H. No. 5-4-47  
Bhudhawarpet, Nirmal  
Nirmal (District) – 504106  
Telangana, India.  
E-mail: [ajay.kumar553@gmail.com](mailto:ajay.kumar553@gmail.com)  
Mobile: +91-9493260602

---

---

**Objective:** To be professionally associated with an organization, where I can utilize my Doctoral Research experience in solving the practical challenges and achieve the goals of the organization.

### Academic Qualifications:

#### EDUCATION AND TRAINING

##### July 2012 – July 2017

##### Doctoral Research Scholar (PhD)

National Institute of Technology Warangal, India  
(<http://www.nitw.ac.in/nitw/>)

##### Current Position:

Full-time Doctoral Research Scholar (PhD) in the **Department of Chemistry** under the supervision of **Dr N. Venkatathri**, Assistant Professor  
(<http://www.nitw.ac.in/nitw/div/view.php?facultyid=16383>)  
(<https://scholar.google.co.in/citations?user=uTzzht8AAAAJ&hl=en>)

**THESIS TITLE:** "*Development of porous Titanosilicate-based hybrid nanocomposites for photocatalytic applications under uv and solar light irradiation*"

##### July 2009 – June 2011

##### Master of Science in Chemistry

National Institute of Technology Warangal, Telangana, India  
(<http://www.nitw.ac.in/nitw/index.php/departments/department-of-chemistry>)

Cumulative Grade Point Average (CGPA): **6.85** (First Division)

**June 2005 – April 2008**

**Bachelor of Science (Biotechnology, Botany and Chemistry)**

Osmania University, Hyderabad, Telangana, India

(<http://www.osmania.ac.in/>)

Percentage of Marks: **63.3** (First Division)

**June 2003 – March 2005**

**Intermediate (Botany, Zoology, Physics and Chemistry)**

Board of Intermediate Education, Andhra Pradesh, India

(<http://bieap.gov.in/>)

Percentage of Marks: **88.6** (First Division)

**June 2002 – March 2003**

**Secondary School Certificate (High School)**

Board of Secondary Education, Andhra Pradesh, India

(<http://bsetelangana.org>)

Percentage of Marks: **83.3** (First Division)

### Professional Summary:

- **Junior Research Fellow** at National Institute of Technology, Warangal, Telangana, India, from July 2012 to July 2014
- **Senior Research Fellow** at National Institute of Technology, Warangal, Telangana, India, from July 2014 to July 2017

### Personal Details:

- Name : A. Ajay Kumar
- Father's Name : A. Sudhakar
- Date of Birth : 5<sup>th</sup> January 1988
- Gender : Male
- Marital Status : Married
- Nationality : Indian
- Languages Known : Telugu, English and Hindi

### Achievements:

- Best Oral presentation award in the “Research Conclave-2017” organized by NIT Warangal.
- Qualified in All India level CSIR-UGC National Eligibility Test December 2011(**Rank-26**).



- Selected Summer Research Fellowship Programme sponsored by Indian Academy of Science (Bangalore), Indian National Science Academy (New Delhi), The National Academy of Science (Allahabad) in the year of 2010.
- Secured 44<sup>th</sup> rank in National level exam “National Institute of Technology Warangal Entrance Test” (NITWET) 2009 for M.Sc. Admissions.

### **Technical Skills:**

- Expertise in utilizing the software - Microsoft Office, Origin etc., Molecular Modeling Systems - ChemDraw Ultra 12.0, HyperChem Release - 8.0.9
- Expertise in MENDELEY Reference Manager

### **Expertise in Instrumental Techniques:**

- UV-Visible dispersive reflectance Spectrophotometers Analytik Jena Specord 205
- Fluorimetry - Fluoroskan Ascent FL 2.6 Thermo Life Sciences
- FTIR Spectrophotometer, PerkinElmer
- Raman spectrometer, HR800 LabRAM confocal
- Gas chromatography, YL 6500, South Korea
- Differential Scanning Calorimeter, Q10 TA instruments, USA
- Surface area and Porosity analyzer, NOVAe 1200 Quantachrome, USA
- Scanning Electron Microscope, VEGA3, Tescon, USA
- Other small instruments relevant for materials characterization and analysis.

### **Research Interests:**

- Design and development of Nanostructured Materials.
- Applications of Photocatalysis.
- Synthesis of microporous and mesoporous materials.

### **Other Capabilities:**

- Capable of carrying out both collaborative and independent research
- Motivated strong ethics and providing efficient service
- Very good interpersonal and communication skills along with management skills
- Good experience in writing technical papers, presentations and reports

- Guided many post-graduate students for their projects

### **Some important workshops and training schools attended**

- Participated in 7<sup>th</sup> IEEE International Conference on "**Technology for Education (T4E-2015)**" organized by NIT Warangal, India during 10-12<sup>th</sup> December 2015.
- Participated in "**Advanced Materials Characterisation Techniques**" organized by Department of Materials Science and Metallurgical Engineering, Indian Institute of Technology Hyderabad (IITH), Telangana, India, during 1-2<sup>nd</sup> November 2014.
- Participated in National Workshop on "**Innovations in Electrochemical Science and Technology (IEST-2013)**" Department of Chemistry, NIT Warangal during 10-14<sup>th</sup> December 2013, Telangana, India
- Participated in the Workshop on "**Innovations in Materials and Processes and Transfer of Technology to Industries**" during 17-19<sup>th</sup> October, 2013 at National Institute of Technology Warangal, Telangana, India.

### **DECLARATION**

I hereby declare that all the information furnished above is true and correct to the best of my knowledge and belief.

Place: Warangal

Date:

**(Mr. A. AJAY KUMAR)**